

---

**FRICITION AND WEAR BEHAVIOUR OF SELF  
LUBRICATING BEARING LINERS**

**Russell Gay**

**Thesis submitted in candidature**

**for the degree of Doctor of Philosophy**

**at Cardiff University**

**Tribology Group**

**Institute of Theoretical, Applied and Computational Mechanics**

**Cardiff School of Engineering**

**Cardiff University**

**March 2013**

---

## Declaration

This work has not previously been accepted in substance for any degree and is not being concurrently submitted in candidature for any degree.

Signed \_\_\_\_\_ (candidate)

Dated \_\_\_\_\_

### Statement 1

This thesis is being submitted in partial fulfilment of the requirements for the degree of PhD.

Signed \_\_\_\_\_ (candidate)

Dated \_\_\_\_\_

### Statement 2

This thesis is the result of my own independent work / investigation, except where otherwise stated. Other sources are acknowledged by explicit references.

Signed \_\_\_\_\_ (candidate)

Dated \_\_\_\_\_

### Statement 3

I hereby give consent for my thesis, if accepted, to be available for photocopying and for inter-library loan, and for the title and summary to be made available to outside organisations.

Signed \_\_\_\_\_ (candidate)

Dated \_\_\_\_\_

---

## Summary

The thesis describes a numerical model for evaluating the variation of friction and wear of a self lubricating bearing liner over its useful wear life. Self-lubricating bearings have been in widespread use since the mid-1950s, particularly in the aerospace industry where they have the advantage of being low maintenance components. They are commonly used in relatively low speed, reciprocating applications such as control surface actuators, and usually consist of a spherical bearing with the inner and outer elements separated by a composite textile resin-bonded liner.

A finite element model has been developed to predict the local stiffness of a particular liner at different states of wear. Results obtained using the model were used to predict the overall friction coefficient as it evolves due to wear, which is a novel approach. Experimental testing was performed on a bespoke flat-on-flat wear test rig with a reciprocating motion to validate the results of the friction model. These tests were carried out on a commercially-available bearing liner, predominantly at a high contact pressure and an average sliding speed of 0.2 ms<sup>-1</sup>. Good agreement between predicted and experimentally measured wear was obtained when appropriate coefficients of friction were used in the friction model, and when the reciprocating sliding distance was above a critical value.

A numerical wear model was also developed to predict the trend of backlash development in real bearing geometries using a novel approach. Results from the wear model were validated against full-scale bearing tests carried out elsewhere by the sponsoring company. Good agreement was obtained between the model predictions and the experimental results for the first 80% of the bearing wear life, and explanations for the discrepancy during the last 20% of the wear life have been proposed.

---

## Acknowledgments

A large amount of the credit for this thesis is due to my two excellent supervisors, Professor Pwt Evans and Professor Ray Snidle of Cardiff University, both of which have been brilliant to work with over the last four years. They have helped me develop my skills as a researcher, an engineer, and as a project supervisor, invaluable experience I will always be able to call upon.

My thanks are due to the EPSRC who funded this project through a joint CASE award with SKF, who also funded my travel to SKF research centres throughout Europe. I would like to thank Andy Bell, Paul Hancock and Michael Colton from SKF Aerospace with whom it has been a pleasure to work. I would also like to thank members of the SKF MFSC Workgroup who have been both friendly and very helpful over the duration of this project.

I must thank my friends Michael Bryant and Grant Dennis for keeping me sane for the last few years, and thanks also to my colleagues Amjad Al-Hamood, Anton Manoylov, Ingram Weeks, Dr. Ben Wright, Matteo Carli, Dr Kayri Sharif and Dr. Alastair Clarke, of the Tribology Group. In addition, thank you to the Cardiff Racing Formula Student team, who have on many occasions given me a welcome distraction from my work, and the entire UCAS team, who have provided both fun and frustration in equal measure.

A special thank you to my parents for their support throughout all my studies, and to my family for their encouragement. Finally I wish to thank my friends - Marc, Charlie, Andy, Josh, James, Robin, Mike, Hesky, and my girlfriend, Lucy, for not only looking after me over the last four years, but also making my time in Cardiff so memorable.

---

# Contents

<b>Declaration</b>	ii
<b>Summary</b>	iii
<b>Acknowledgments</b>	iv

## **Chapter 1: Introduction and Review of Relevant Work**

1.1	Overview	1
1.2	Tribology and Self-Lubricating Bearings	1
1.3	History of Textile Liners	9
1.4	Woven Fabric Bearing Liners	12
1.4.1	Performance of Polymer Self-Lubricating Bearings	13
1.4.2	Counterface	18
1.4.3	Bearing Geometry	19
1.4.4	Environmental Conditions	21
1.5	Tribology of Dry Sliding	25
1.6	Computer Modelling of Self-Lubricating Bearings	30
1.7	Future Development of Bearing Liners	34
1.8	Aims & Objectives	35

## **Chapter 2: Modelling the Weave**

2.1	Objectives	37
2.2	Weave Visualisation	39
2.3	Finite Element Model	40
2.3.1	Unit Cell Geometry	40

---

2.3.2	Contact Settings and Element Selection	49
2.3.3	Harmonic Boundary Conditions	58
2.4	Assumptions and Limitations	65
2.4.1	Thread Cross-Sections	65
2.4.2	Variation in Thread Thickness	67
2.4.3	Weave Pattern in Warp vs. Weft Direction	67

### **Chapter 3: Building the Weave Model**

3.1	Overview	69
3.2	Python Script Structure	71
3.2.1	User Variables	71
3.2.2	Abaqus General Commands	72
3.2.3	Create Design Area	73
3.2.4	Model Assembly	78
3.3	Post-Python Tasks	80
3.4	Results	82
3.5	Technicalities of Python Script	84
3.5.1	Selecting Points	84
3.5.2	Mesh Resolution	85
3.5.3	Omission of Prepreg Layer	88

### **Chapter 4: Friction Model**

4.1	Concept Overview	93
4.2	Tribology Assumptions	94
4.3	Principles	96
4.4	Abaqus Output Files	98

---

4.5	Wear Steps	102
4.6	Model Structure	104
4.6.1	Model Setup	105
4.6.2	Load External Inputs	106
4.6.3	Format Data	107
4.6.4	Define Materials	108
4.6.5	Calculate Friction Coefficients	108
4.7	Results	110
4.8	Limitations	114

## **Chapter 5: Experimental Work & Comparison to Friction Model Results**

5.1	Overview	117
5.1.1	Capabilities	118
5.1.2	Key Features	119
5.1.3	Data Output	125
5.1.4	Early Test Rig Problems	126
5.2	Test Results	128
5.2.1	Example of Test Results	128
5.2.2	Variation in Reciprocating Sliding Distance	136
5.2.3	Variation of Mean Contact Pressures	144
5.2.4	Counterface Roughness	147
5.3	Comparison with Friction Model Results	148
5.3.1	Experimental Results	148
5.3.2	Literature Model	150
5.3.3	Test Bench Model	152
5.3.4	Modified Resin Model	154

---

5.4 Discussion	156
----------------	-----

## **Chapter 6: Wear Model**

6.1 Theory	159
6.2 Spherical Plain Bearing Liner Contact Model	165
6.2.1 Relationship between Contact Load and Eccentricity	165
6.2.2 Liner Contact Model Discretisation and Solution Method	167
6.2.3 Comparison of Liner Contact Model and equivalent Finite Element Model	175
6.3 Adding Wear to the Liner Contact Model	178
6.3.1 Overview	178
6.3.2 Sliding Distance	180
6.3.3 Wear Model Operation	182
6.4 Results and Comparison with Test Data	183

## **Chapter 7: Conclusions and Future Work**

7.1 Overview	189
7.2 Aims and Objectives Met and Contributions	190
7.3 Future Work – Friction Model	191
7.4 Future Work – Experimental Data	193
7.5 Future Work – Wear Model	196
7.6 Summary of Conclusions	198

<b>References</b>	199
-------------------	-----



# **1. Introduction and Review of Relevant Work**

## **1.1 Introduction**

This thesis investigates a computational approach to predicting friction and wear in self-lubricating composite bearings, and compares the results of the approach taken with experimental measurements. This chapter introduces the field of tribology and the principal applications of self-lubricating composite bearings. Relevant literature related to both composite bearing tribology and computational modelling of dry-sliding and self-lubricating bearings is also discussed in detail.

## **1.2 Tribology and Self-Lubricating Bearings**

Tribology is defined as “the science and technology of interacting surfaces in relative motion” (Department of Education and Science, 1966), though it can be more simply described as the combined effect of friction, lubrication and wear. It is interesting that it is only (relatively) recently that a term was created to refer to a science that has existed for millennia. Dowson (1979) discusses stone carvings found in Ancient Egypt, circa 2400 B.C., showing the use of lubricants on sledge tracks, and metal rims on wheels to reduce wear are evidenced as early as 2750 B.C. The most prominent and truly ancient example of tribology in history however is in the creation of fire. By patiently rubbing wood together, there is evidence of man creating fire in a controlled fashion dating back to 100,000 B.C. (Bowman et al., 2009). In Greek mythology, fire was a concept stolen from the gods by the Titan

Prometheus, so it is fitting that the etymology of the word tribology derives from Ancient Greek, *tribos*-, “to rub”, and *-logy*, “knowledge of”. Prometheus was renowned for his intelligence, and is the first of many names similarly famous for their genius who have developed understanding of tribology. Leonardo Da Vinci’s notebooks for example, dating back to c1500, show that he understood that friction was independent of contact area, and describes basic tests which are now used educationally at a high-school level (Carnes, 2005).

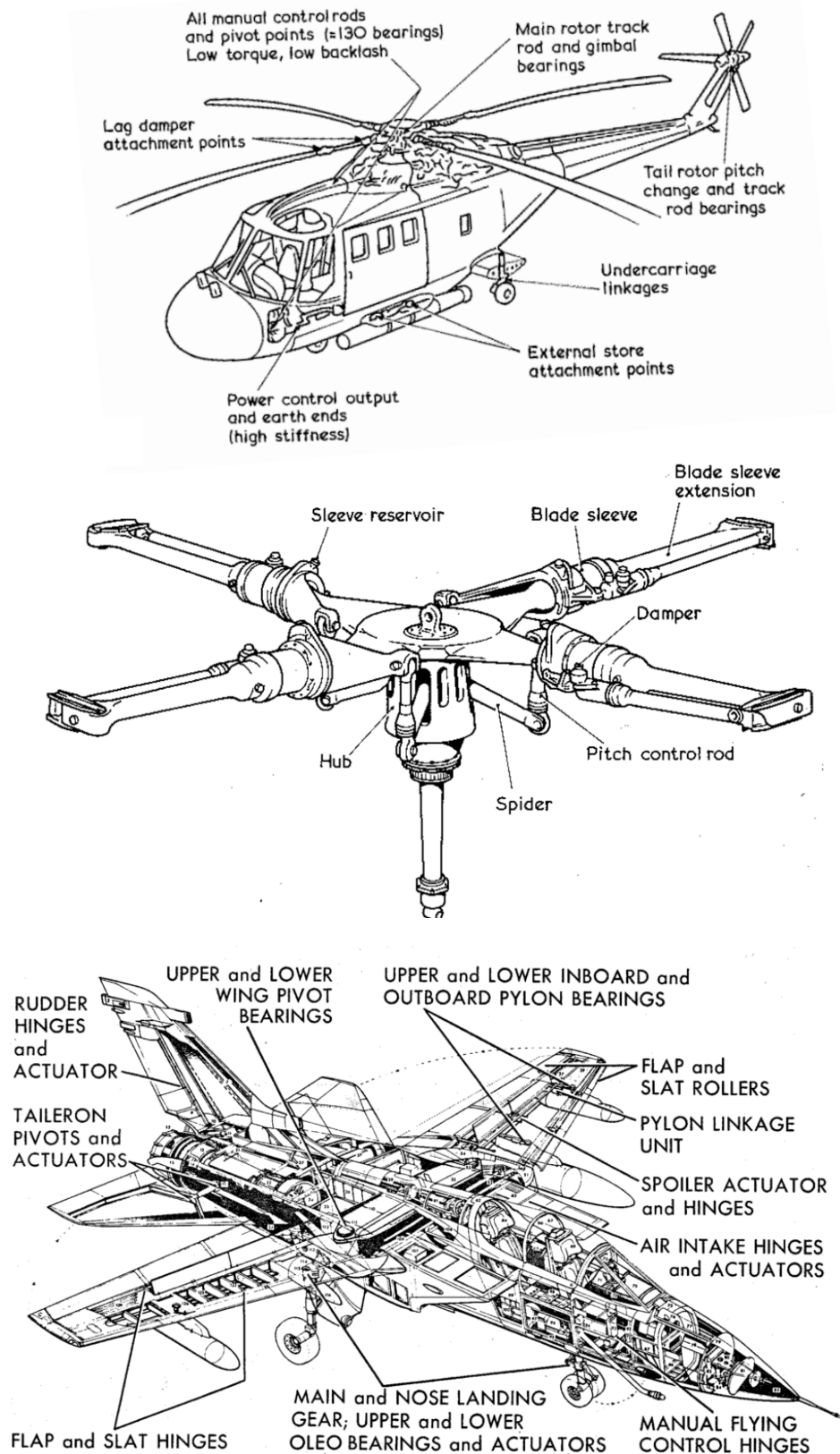
Bearings have a similarly long history, with one of the earliest examples of a recognisable bearing design being the axles used in early wheels. The Ancient Greeks used bearings lubricated with animal fats in their ships, though in this case their under-development in the field of tribology was to be to their detriment, as the animal fats would catch fire due to the heat generated by the bearings, destroying entire ships. The invention of the roller bearing is often attributed to Da Vinci, though this is incorrect as the earliest example was found on the Nemi ships of the 1<sup>st</sup> century A.D. (Rossi et al., 2009). Da Vinci is however credited with the first use of bearings in an aerospace design (U.S.C.P.B., 2012).

Leonardo used rolling-element bearings in his designs, and while the aerospace industry did not “take off” until the late 19<sup>th</sup> century, the use of rolling-element bearings in aeroplanes and helicopters remained common until the 1930s. It was at this time that the use of self-lubricating journal bearings was proposed, in the form of oil-filled sintered bronze bearings. While the overall life-span of these bearings was less than that of their rolling-element counterparts, they required no maintenance over their life, as opposed to rolling-element

bearings which require re-greasing at regular intervals. In addition, rolling-element bearings require a sufficient amount of rotation to distribute the lubricant, and in applications with a limited degree of oscillation, rolling-element bearings can quickly become dry in the contact area, and suffer damage in a limited section of the bearing track (Bell, 2013). The oil in sintered bronze bearings was saturated into the pores of the bronze, and required high speed rotation to “draw out” the oil, making them unsuitable for the many low-duty, low-speed reciprocating motions found in aircraft. Polymer journal bearings were a more useful form of self-lubricating bearing for the aerospace industry. Polymer journal bearings similarly did not have the same operating life-span as rolling-element bearings, but offered two key advantages over their bronze counterparts. Firstly they were lightweight, a very serious consideration in the aerospace industry where weight can affect top speed, fuel efficiency, manoeuvrability, and in some cases whether or not the aeroplane can actually take off (Allen & Bell, 2013). Secondly, they significantly increased the aircraft maintenance interval, i.e. the number of hours an aircraft can be flown before it needs “servicing”, as the bearings only require attention when they are replaced at the end of their life. With the cost of grounding a helicopter and servicing the bearings estimated at €35,000 (Bell, 2012a), and other estimates putting the cost of maintaining an aircraft as a third of its overall lifetime operating costs (Lancaster, 1982), increasing the maintenance interval of aircraft represents a very significant cost saving.

A problem with early polymer bearings was their strength, or lack thereof. The use of materials such as Nylon and PTFE provided low friction, but they could not support heavy loads. This meant their use was limited to low-load applications within aircraft. The use of

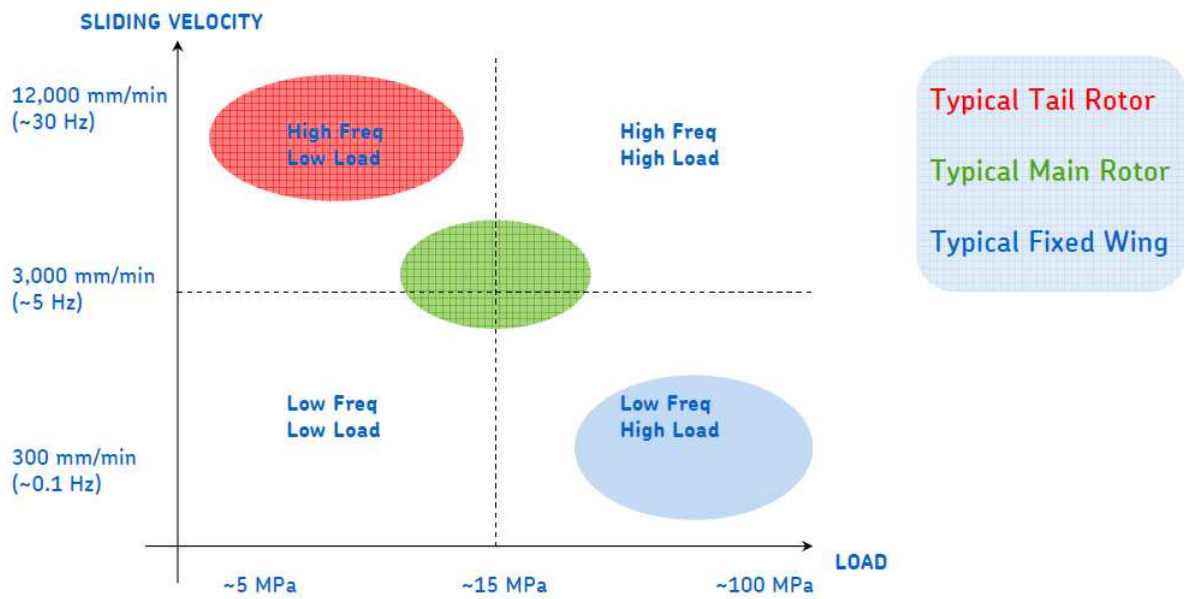
composite materials in the 1950s created bearings which had the low-friction characteristics of the pure polymers, but with much higher load-bearing ability. Their areas of application in aircraft quickly increased, and they are now found in many areas where there is a high degree of reciprocation, or infrequent usage. Figure 1.1 shows applications of self-lubricating bearings identified by Lancaster (1982) in both fixed wing (aeroplanes) and helicopter applications, including a magnified schematic of the applications in a helicopter main rotor.



**Figure 1.1** Examples of applications of self-lubricating bearings in helicopters (top) – specifically in the main rotor (middle) – and a Tornado fighter jet (bottom) (Lancaster, 1982)

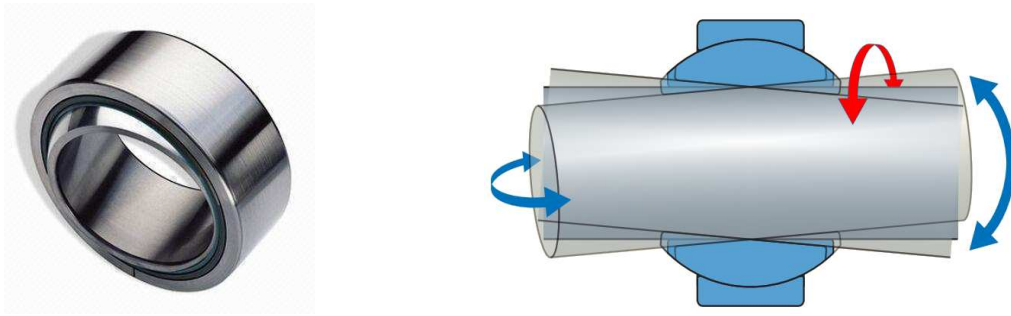
The use of self-lubricating bearings in fixed wing and helicopter applications generally falls into two categories. Firstly, parts such as landing gear and load bay doors are subject to high-load and very low frequency use, and therefore are unsuitable for lubricated bearings, which require regular movement to maintain full-film lubrication. Secondly, components such as control flaps and rudder actuators are subject to higher frequency movement, but over a very limited travel and often in a reciprocating motion. Indeed, as aircraft become more complex and increasingly manoeuvrable, the frequencies at which these control flaps have to move increases. While the speed and frequency of control flaps adjustments is increasing, the majority of fixed wing applications are considered to be at the high-load, low-frequency end of the spectrum of self-lubricating bearing applications

In helicopter applications, there are again two general categories into which the use of self-lubricating bearings fall. Firstly, in main rotor applications, the bearings controlling the attack angle of the rotor blades are subject to medium loads at a medium frequency range (relative to the spectrum of aerospace applications). Tail rotors, from which helicopters derive their stability, are subject to low loads, but at very high frequencies, as adjustments are constantly made to the angle of attack of the blades on the rotor, and the rotor spins at a much higher speed. A summary of the applications and their operational parameters is presented in Figure 1.2. This summary is not all-encompassing, as there are some areas in both fixed wing and helicopter applications which fall outside of the denoted region, but it serves as a general overview of the area.



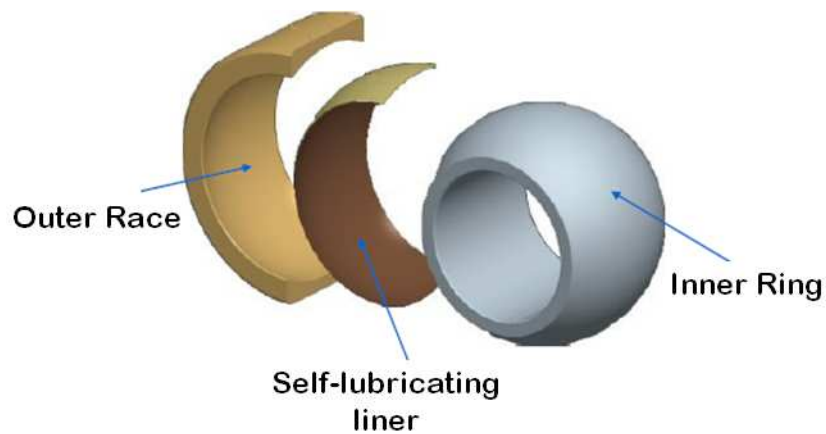
**Figure 1.2** Summary of applications of self-lubricating liners and their operating parameters (Bell, 2009)

“Spherical plain bearings” are particularly useful compared to journal bearings as they can tolerate misalignment between the axis of rotation and the axis of the housing. These misalignments can be a result of design, assembly, or deflection under load. A spherical plain bearing is shown in Figure 1.3, along with a schematic showing misalignment direction with blue arrows, and rotation with a red arrow.



**Figure 1.3** Spherical Plain Bearing showing oscillation of shaft fixed to inner ball in rotation (red) and misalignment (blue) (Made in China, 2012) (SKF Group, 2010)

Self-lubricating spherical plain bearings generally incorporate three components – a metal inner ring and outer race, and a self-lubricating “liner” between them, illustrated in Figure 1.4. The liner is bonded to the outer race so that the sliding interface is between the liner and the inner ring.



**Figure 1.4** Components of a self-lubricating spherical plain bearing (Bernard, 2011)



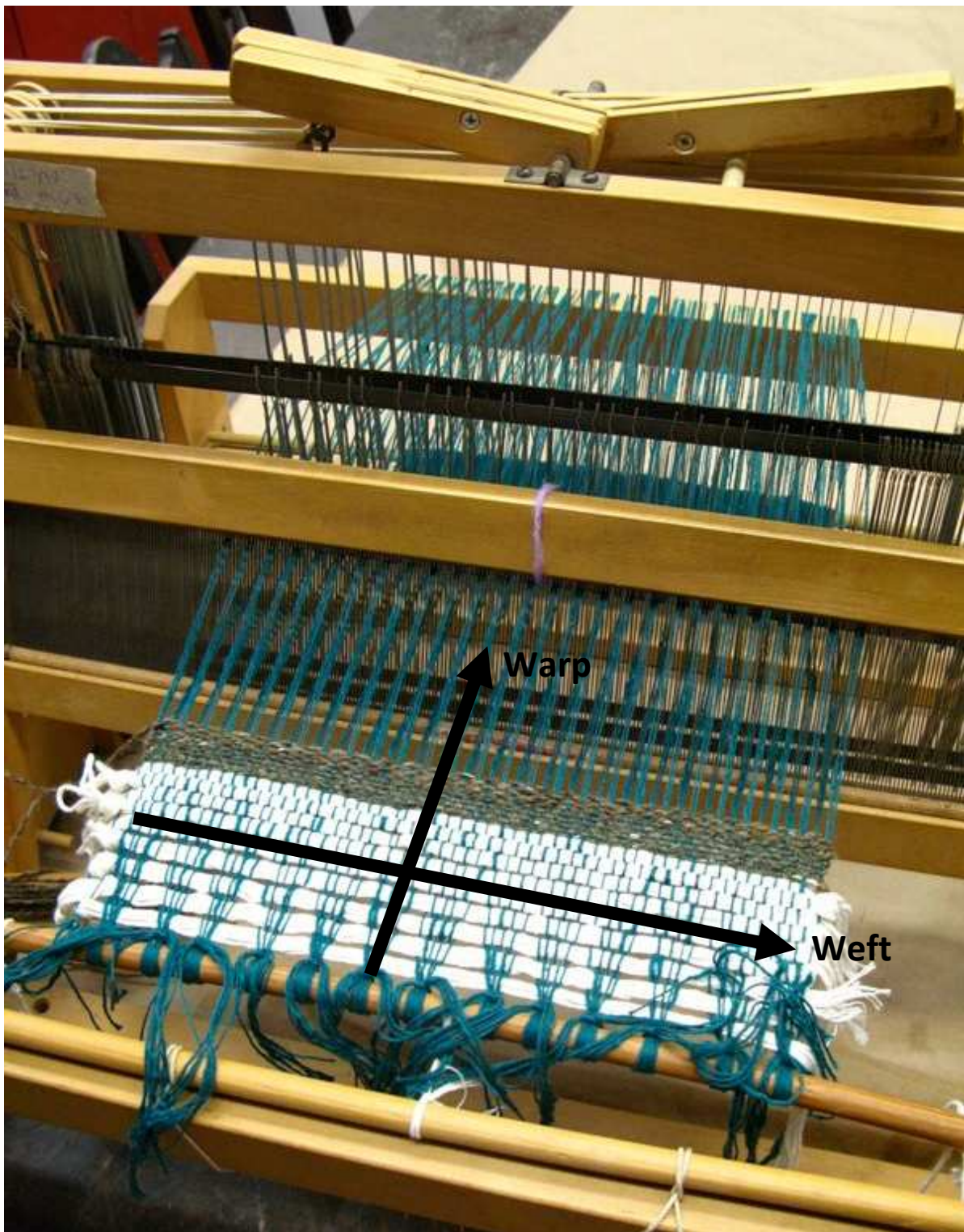
The applications of self-lubricating bearings are not limited to aerospace. Most forms of transport, including automobiles and trains, incorporate some self-lubricating bearings, as do marine applications and power generation. Increasingly, manufacturing and processing industries benefit from the cost-savings that can be realised by reducing maintenance intervals through use of self-lubricating bearings.

### **1.3 History of Textile liners**

With a variety of industries using self-lubricating bearings, and a wide range of application conditions within each industry, a “one-size-fits-all” self-lubricating bearing material has not proved to be feasible. PTFE was often used in self-lubricating bearings due to its very low coefficient of friction, though this is only true at low sliding speeds or high loads (Santner & Czichos, 1989). At low loads or high sliding speeds a coefficient of friction as high as 0.3 may occur, which does not distinguish it from many other polymers. PTFE alone however is unable to support higher loads (Lancaster, 1982), necessitating the introduction of some form of reinforcement.

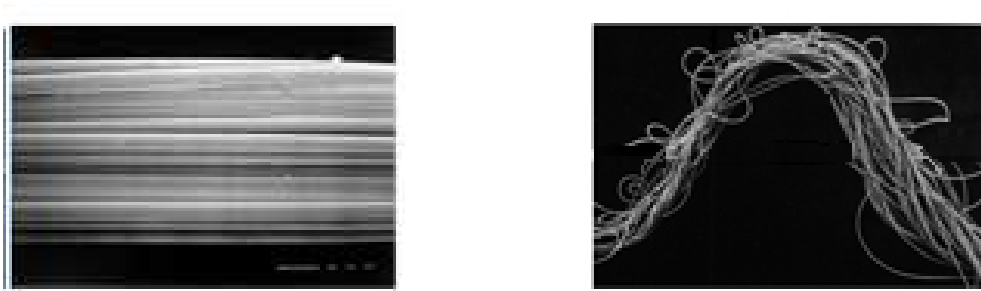
Ampep Ltd. was founded in 1963, and supplied self-lubricating bearings predominantly to the aerospace industry. In the mid 1960s one of their new product lines incorporated a self-lubricating liner called “Fiberslip”, produced by a weaving process. Two yarn types were included in a two-layer warp providing lubrication and reinforcement properties. The “warp” of a fabric consists of the yarns which are held tight in the loom, while the “weft” threads are passed over and under them. Figure 1.5 shows an example of a woven material on a loom,

with the warp and weft yarns highlighted. Note that this is not a bearing material, and that the image is chosen for illustration purposes only.



**Figure 1.5** Woven material on a loom with warp and weft yarns highlighted (Eto, 2008)

A yarn can be either mono-filament or multi-filament. A mono-filament yarn is a thread made up of a single strand of a fabric type, for example a fishing line. A multi-filament yarn is made up of many strands of the same or different fabric types, usually twisted together, as shown in Figure 1.6. A prime example of a multi-filament yarn is a rope.



**Figure 1.6** Multiple filaments (left) twisted to form multi-filament yarn (right) (Siede, 2012)

## 1.4 Woven Fabric Bearing Liners

Ampep carried out an investigation into improving the performance of “Fiberslip” by varying the proportion and location of the lubricant and reinforcement yarns in a woven fabric. One of these variations is the basis of this investigation, and will be referred to as the test fabric.

The stiffness of the test liner was tested by Harrison (1978) using disc shaped samples of 25.4 mm diameter which were tested up to a load of 400 kN, or a pressure of 197 MPa. The results presented in the report however show only the trend lines of the stress-strain variation for the materials tested, not the individual data points. Bennett (2008) conducted a similar test, with

samples of area  $628 \text{ mm}^2$  and a pressure of up to 400 MPa. In this test, the individual data points for stress versus strain were given. Two clear stiffness phases were apparent, with the liner elastic modulus increasing by a factor of four at high loads. Neither of these values agree with the earlier work of Harrison (1978). However, as the raw data for this test is available, and the tests were carried out on much larger samples (therefore minimising the effects of any exceptional features), these results are viewed as more reliable.

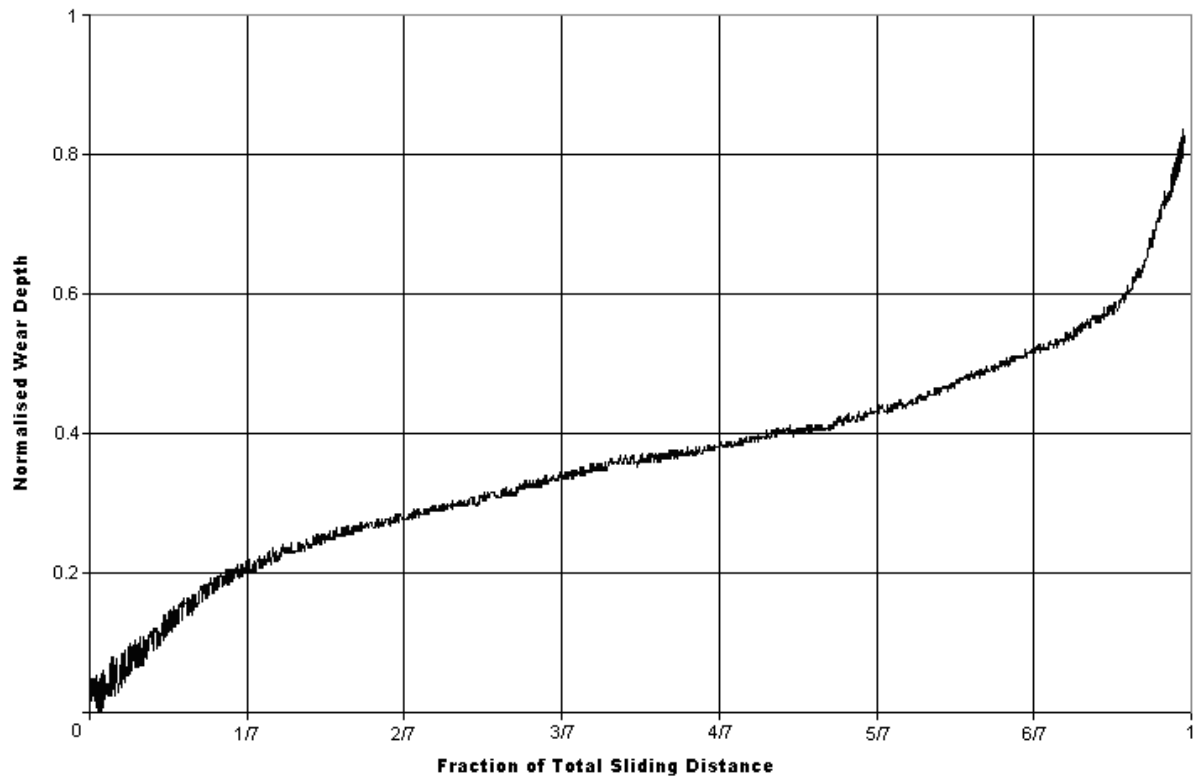
#### **1.4.1 Performance of Polymer Self-lubricating Bearings**

The majority of the tribological investigations into the performance of self-lubricating liners was carried out in the late 1970s and early 1980s by Lancaster and Play. Play was a French tribologist at the Institut National des Sciences Appliquées de Lyon, and Lancaster worked for the Royal Aircraft Establishment (RAE). In addition to the papers published by the two, Lancaster produced a series of technical reports for the RAE on the subject. While these technical reports are not peer-reviewed, much of the information presented in the journal articles stems from them, with any information of commercial sensitivity removed, and are therefore referred to in this review. This important body of work still contains the majority of available knowledge on the subject of self-lubricating liners to date.

Lancaster, in his role as an aerospace engineer, was predominantly concerned with comparative testing of self-lubricating bearing liners available in the later 70s, to determine their suitability for applications in military aeroplanes and helicopters. Lancaster (1982) identified that full-scale bearing tests under a given set of operation conditions (known as

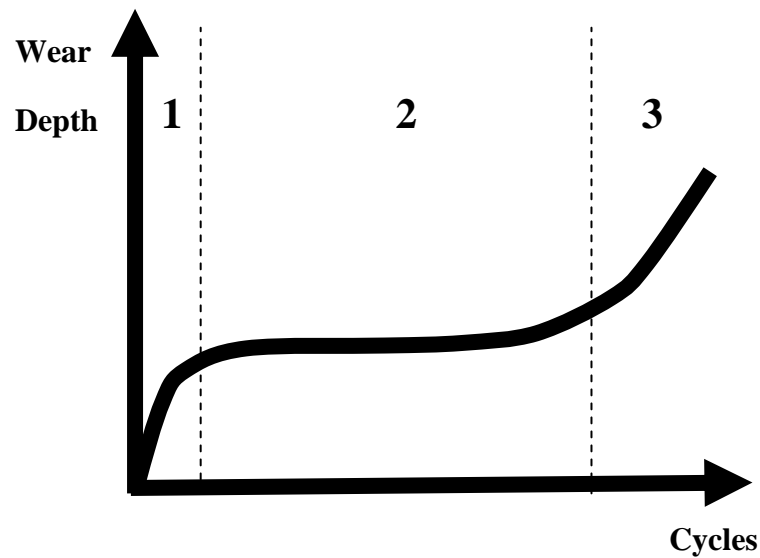
demonstrator tests) would only show the performance of a self-lubricating or “dry” bearing under those exact conditions, and were unsuitable to develop an understanding of why certain materials performed better than others. In addition to the range of operating conditions possible in aircraft, there was also a range of possible surface finishes and coatings applied to inner rings. Beyond these application parameters, the influence of environmental conditions such as temperature (King, 1979) and humidity (Morgan & Plumbridge, 1987) have been shown to have a significant effect on the performance of self-lubricating bearings. The effect of some of these factors is discussed in this chapter.

For aerospace hardware, SAE International publishes specifications to prove the suitability of a bearing for a particular application. Specifications AS81819 and AS81820 define the test conditions and minimum performance requirements required for bearings to be used in high-speed and low-speed applications, respectively. To comply with these standards, often a number of bearings must be tested under a given set of conditions to simulate certain operating conditions, requiring bespoke test benches and often a testing period of many months. Suitability is usually indicated by a maximum wear depth allowed after a given number of cycles. Tests were carried out with online wear measurement to sense the wear depth over the life of the bearing. These results do not account for the deflection of the liner under load, but they show a general pattern of wear behaviour over the life of a bearing. Figure 1.7 shows an example of these results.



**Figure 1.7** Example of wear progression of a self-lubricating spherical plain bearing

King (1979) tested a range of self-lubricating materials and noted a similar pattern of high initial wear rate transitioning to a “steady-state” wear rate which was considerably lower. He described this transition point as a “knee”, and while the pattern was similar between materials, he noted a wide range of “knee” depths and steady-state wear rates between the materials he tested. Figure 1.8 shows the commonly accepted progression of wear depth in a self-lubricating spherical plain bearing, with three zones shown (Dayot, 2011). Zone 1 is the wear-in of the bearing, zone 2 is the steady-state wear of the bearing, and zone 3 is the wear-out. The “knee” described by King occurs at the transition between zones 1 and 2.



**Figure 1.8** Typical wear depth progression over life of a self-lubricating spherical plain bearing (Dayot, 2011)

It is hypothesised that the transition in wear rate between zones 1 and 2 is due to the development of a PTFE “transfer layer” (Yang et al., 2009), discussed later, leading to a significant reduction in wear and friction. The transition between zones 2 and 3 is similarly hypothesised to be due to the breakdown of this transfer layer due to cyclic stress and plastic deformation (Yang et al., 2009). This transfer layer is essentially the inclusion of PTFE wear debris between the surface asperities on the metal counterface, reducing the effective roughness of the counterface (Briscoe et al., 1988). Briscoe et al. (1988) tested pure PTFE pins sliding on metal counterfaces, and observed that development of this transfer layer starts very early in the wear life, in fact from the first cycle i.e. the first generation of PTFE debris.

Lancaster concluded that a means of screening potential self-lubricating materials quickly



was necessary, as full-scale bearing tests were too time-consuming to be useful to aid technology development (Lancaster, 1982). Lancaster devised an apparatus which would create Hertzian line contact stresses between a rotating metal cylinder and a reciprocating flat strip of bearing material (Lancaster, 1979), and demonstrated results across a range of materials which exhibited a similar form to Figure 1.8. He noted considerable differences between the performance of different materials. However, he was unable to extrapolate these results to full-scale bearing tests as insufficient data were available to him on the range of materials tested. Lancaster identified a range of situations which can lead to over- or under-estimation of wear performance. For particularly rough surfaces, he stated that sample tests underestimate the initial running-in period, an effect which increases with load. He also stated that, for composite materials, the sample size should be big enough to contain a representative proportion of all materials in the composite. The operating conditions to which the bearings are subjected have a significant influence on performance. Higher loads can lead to increased wear rates, as can increased sliding speeds, though Pihtile & Tosun (2002) point to load as the more influential parameter.

### 1.4.2 Counterface

Lancaster (1982) noted significant increases in lifespan of bearing liners when counterface roughness was reduced. He found lifespan increased when roughness was reduced from 0.65  $\mu\text{m}$  to 0.20  $\mu\text{m}$  roughness average (Ra), and again when reduced to 0.05  $\mu\text{m}$  Ra. He found that the effect of reducing the roughness even further to 0.015  $\mu\text{m}$  Ra was however negligible, a result which corroborated information from industry at the time.

Kennedy et al. (1975) investigated the factors affecting the wear of polyethylene against a steel counterface. They found that wear rate decreases when moving from a very rough surface to a smoother surface, but found a point at which increasing the smoothness of the surface further actually increased the wear rate. In the case of polyethylene on steel, they found this roughness to be 0.1  $\mu\text{m}$  Ra. Surprisingly, they also found the coefficient of friction decreased with increasingly rough surfaces.

Lancaster (1981) discussed the effect of counterface hardness on the wear of the counterface. In the case of hard counterfaces, there is little to no surface modification of the counterface over the wear life of the bearing liner, and therefore initial and steady state wear rates are affected by the magnitude of the initial roughness. In the case of softer counterfaces, there is extreme abrasion of the surface, and therefore surface roughness can increase over the wear life of the bearing liner, thereby increasing the wear rate. When a medium is interposed between these however, such as the Cu-10% Al alloy, there is the possibility of the surface roughness decreasing over the lifespan of the bearing liner, leading to lower wear rates. All

these effects however are severely dampened by the presence of a “transfer film” of third body particles, which reduces the effect of surface roughness on wear rate.

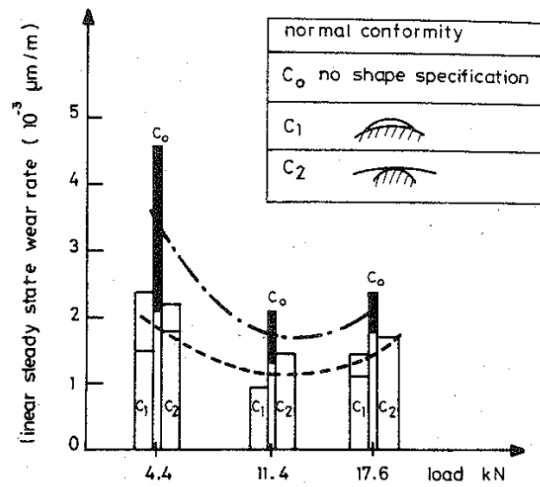
Lancaster (1982) discussed the wide range of surface coatings used by industry for the inner ring component in self-lubricating bearings, and postulates that different coatings could cause different tribological mechanisms to take precedence, which could also be affected by operating conditions. Holmberg et al. (1997) broke down these dry sliding tribological mechanisms into four types – macromechanical, micromechanical, chemical and material transfer. Dependent on load, sliding speed, temperature and environment, the main tribological mechanism can change with the same sample/counterface pair, thus changing the performance of the counterface under different operating conditions.

### **1.4.3 Bearing Geometry**

Play and Pruvost (1983) looked at the relationship between cylindrical bearing (journal bearing) tests of a self-lubricating composite and spherical bearing geometry. They used a PTFE- and Nomex-fibre woven composite with a phenolic resin. They noted that both cylindrical and spherical geometries exhibited decreased coefficients of friction with increased load. They noted that if the average contact pressure in spherical bearings is adjusted for the real contact area as opposed to the apparent contact area (which they propose is  $1.5\times$  larger than the real contact area), the relationship between contact pressure and friction coefficient is the same for both spherical and cylindrical geometry. This they believe explains the small coefficients of friction exhibited in spherical bearings compared to

material tests. They also propose that the lower wear rates found in spherical bearings compared to cylindrical bearings are due to the movement of the wear debris generated. In both cases, the debris moves from the heavily loaded zone to the unloaded zone. In the case of a cylindrical bearing with a line contact, this migration often takes place axially, and the debris is ejected out of the sides of the bearing. In the case of a point contact in a spherical bearing, the debris has to move through an unloaded region of the spherical bearing before it reaches the edge, at which point there is little imperative for it to move further and so it stays in the bearing. This hypothesis is supported by the observation that spherical bearings show very little change in overall weight after testing compared to their cylindrical bearing counterparts.

Play & Pruvost (1983) also investigated the effect of conformity on bearing wear rate. They tested three bearings – one with normal close-tolerance conformity ( $C_0$ ), one with an increased closed shape ( $C_1$ ) and one with an increased open shape ( $C_2$ ), as shown in Figure 1.9, with the results displayed as bars, with the spread of results shown as blocks at the top of the bars. Figure 1.9 shows that when the conformity was reduced in either a closed or open shape, the wear rate was decreased considerably. Play & Pruvost do not offer any explanation for this feature, other than as an indicator that small changes in bearing geometry can have a considerable influence on the lifespan of the bearing. They also noted that reduced-conformity bearings exhibited a significantly increased no-load torque, but they did not attempt to correlate the two findings.



**Figure 1.9** Effect of normal conformity and load on linear steady state wear rate in spherical geometry (Play & Pruvost, 1983)

#### 1.4.4 Environmental Conditions

King (1979) investigated the behaviour of several commercially-available self-lubricating bearing liners at ambient and elevated temperatures, in order to develop an understanding of how these conditions can affect performance. Aircraft components in extreme environments can be exposed to temperatures in excess of  $100^{\circ}\text{C}$ , and temperatures in this range can significantly impact the tribological and structural performance of polymers (both thermosetting and thermoplastic) used in self-lubricating bearings (Yang et al., 2009). Yang et al. (2009) investigated the effect of a critical temperature on woven liners, but in this case discussed the effect of surpassing the reinforcement transition temperature of PTFE in a PTFE/Kevlar/Cotton liner reinforced with phenolic resin. They noted deterioration in the wear resistance of the liner once this temperature had been exceeded, but failed to quantify

the extent of the reduction in wear performance.

King (1979) adopted an early version of the testing apparatus used by Lancaster (1979) to generate a reciprocating line contact. He showed that an increase in temperature to 100°C above ambient could increase the wear rate of some materials, particularly those incorporating reinforcement and other inorganic materials in the weave pattern, by a factor of 10. Evans (1978) noted a similar pattern when testing PTFE composites, and attributed this effect to the increased temperature hindering the creation of a PTFE transfer layer. Lancaster (1981) also attributes the temperature-dependent effects to the formation of a transfer layer being inhibited, and postulates it may be due to the reduction in either cohesive or adhesive forces at the third-body/wear debris interface at elevated temperatures.

While some materials do show temperature-sensitivity in their steady-state wear rates, King (1979) found that the “knee” depth of some materials was not dependent on ambient temperature. King was also not able to extrapolate these results to a prediction of bearing performance, as he noted that some materials which performed well in his testing conditions did not perform as well in full-scale bearing tests, and vice-versa. In addition, he noted that little data were available on full-scale bearing tests, as these are for the most part often carried out by bearing manufacturers for developed materials and not for experimental materials which are still in development.

Floquet et al. (1977) identified contact interface temperature as one of the key factors

affecting bearing performance, and created a numerical model to understand the influence of certain bearing design decisions. They found that the interface temperatures were highest when the bearing was subjected to a reciprocating motion compared to a uni-directional rotating motion, and when the bearing liner was attached to the rotating shaft instead of the static housing (Floquet & Play, 1981).

Humidity is another factor in bearing performance, particularly seen in “bearing torque”, which is the torque of a bearing under no load. This has been noted to vary for the same bearing day-to-day at very similar ambient temperatures, and this is often attributed to variations in humidity (Bell, 2012b). Morgan and Plumbridge (1987) investigated the effect of humidity on the ultimate tensile strength, indentation recovery and bearing torque of a woven composite. They used an apparatus housed in sealed humidity cabinets to undertake tests, so they could vary the humidity of the environment. They noted that the ultimate tensile strength was reduced by approximately 25% when humidity was increased from 20% to 80%, and that specimens under lower humidity conditions exhibited more deformation under load than in higher humidity conditions. This would indicate that the strength of the material is reduced under high humidity conditions, while its stiffness increases. They rationalised this discrepancy in that the reinforcement components, which are the greatest factor in the strength of the material, become weaker when exposed to moisture, whereas the swelling of the PTFE component under higher humidity leads to a more tightly packed structure, which increases the overall stiffness. In addition, they noted that bearing torque was approximately 30% higher in bearings at a humidity of 80% than at 20%. Importantly, they noted that the material took around 20 hours to respond to a change in humidity, meaning it is not affected

by short-term changes in humidity. They discuss the relationship between bearing torque and humidity proposed by Kuhn, but show that this relationship gives an estimate of bearing torque that is an order of magnitude too large, and conclude that there are not enough available data to propose their own relationship. They also conclude that the effect of temperature variation on bearing torque could be attributed to the associated variation in humidity due to temperature change.

The effect of humidity on wear rate was investigated by Moreton (1983). In sample tests, he noted no influence on the wear rates of materials with humidity in the range of 0.1% to 90% when the tests were loaded under a line contact conditions, however, he noted increases in wear rate up to 2.5× with some of the same materials in a point contact, while others maintained their insensitivity. In contrast to Morgan and Plumbridge (1987), he observed no effect on friction coefficient due to humidity level. He found the materials most affected by humidity were polyamide, graphite and Aramid. Graphite was particularly susceptible to increased wear when near 100% humidity occurred and condensation began, leading to an increase in wear rate of 15×.

Much work has also been undertaken on the effect of contamination of bearings by fluids, as this is often an unavoidable operating condition (Lancaster, 1982). Bramham et al. (1980) identified a range of fluids which were detrimental to bearing life, but found no trend for predicting the effect of an untested fluid based on a known property, such as viscosity. They also found that some mineral oils gave improved performance. All tests were undertaken



however at one sliding speed and load, therefore the influence of different fluids could very easily have varied under different operating conditions.

## **1.5 Tribology of Dry Sliding**

The Laboratoire de Méchanique des Contacts (Laboratory of Contact Mechanics) at INSA, Lyon, carried out a large amount of work on friction and particularly wear of dry sliding materials. In their paper of 1980, Godet et al. attempt to apply some principles of lubricated tribology theory to dry sliding, particularly with regard to the formation and transport of third body debris. In particular they highlight the enormity of the effect that third body debris can have on the wear rate of a dry sliding system, dependent on whether it is entrained within or ejected from the contact area.

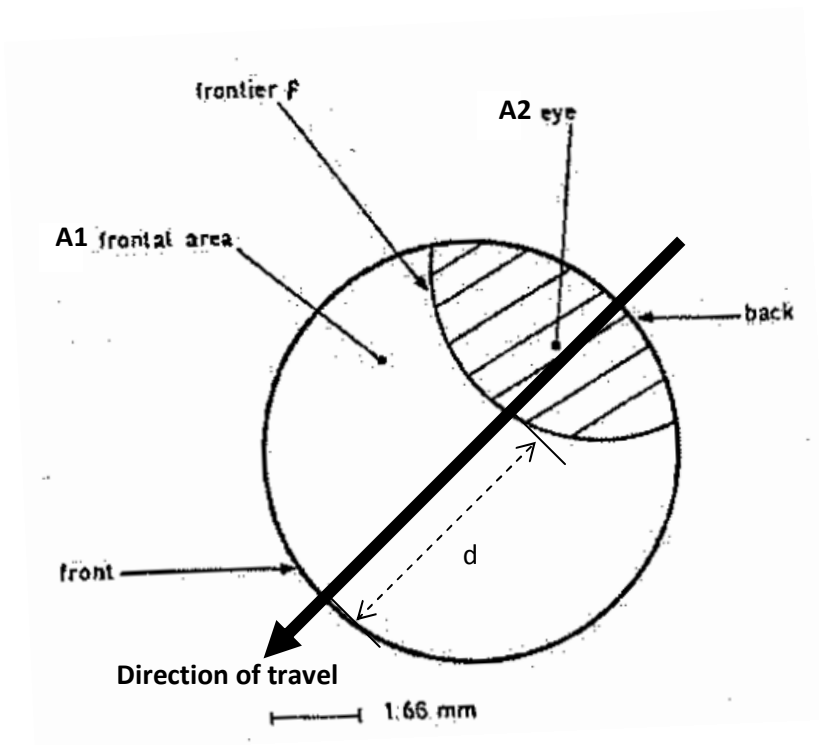
The principle of wear proposed is that a third body is formed from wear debris within the contact through some wear mechanism, i.e. adhesion or abrasion, which is then progressively removed from the contact area (Play, 1985). The volume of wear is therefore the volume of debris lying outside the contact area. Depending on the material, the debris can also form a “third-body film” or transfer layer. The thickness of this transfer layer depends on the amount of wear debris generated and the ratio of the contact area between a sample and the counterface and the length of the counterface. This seems fairly obvious, as if it is assumed all wear debris becomes a transfer layer of uniform thickness, the thickness of the layer will be:

wear volume (m<sup>3</sup>) / total contact area over a cycle (m<sup>2</sup>) = thickness of transfer layer (m)

Play (1985) noted that the transfer layer is not uniform, and tends to be thicker towards the centre of the contact. This is explained by Godet et al. (1980), who discussed how wear debris can only be ejected from the edges of a contact, therefore debris entrained in the centre of the contact cannot easily be removed, as in “wet” lubrication theory of un-sealed journal bearings. Play (1985) also noted that the coefficient of friction and wear rate is considerably lower in oscillating motion than in uni-directional sliding, a finding supported by Lancaster et al. (1982). Play (1985) described contacts in terms of a Mutual Overlap Coefficient (MOC), defined as the ratio of the contact area of the sample to the total contact area of the counterface traversed by the sample. Play tested the effect of MOC using chalk pins on a glass counterface. When the vertical displacement of a pin is compared with time, a curve very similar to that observed by King (1979) is seen, with three distinct phases. The running in period is, however, much shorter as a proportion of overall test duration. They noted that wear rate is reduced when this MOC ratio is high (a short stroke length) but the friction coefficient is increased. However, it is important to note that both these values are taken from the final “running out” part of the wear curve, and not from the steady-state period. These effects cannot therefore be directly compared with the literature on bearing liners, where wear rate and friction coefficient are typically taken during the “steady-state” phase of their wear curve.

The development of a third body transfer layer is attributed to lower wear rates, and this is described as a “self-protective” feature of dry sliding materials (Play & Godet, 1977). Play

and Godet (1977) described this self-protective feature as dependent on the length of the contact normal to the sliding direction, and independent of the width. They proposed a model with two contact zones, as seen in Figure 1.10 taken from the paper. In the “frontal area” (denoted A1 on Figure 1.10), wear debris is formed by interaction with asperities of the counterface, and the debris fills the gaps between the asperities. Excess debris then forms a third body film on top of the counterface, and the friction and wear of the “eye” (denoted A2 on Figure 1.10) is governed by the interaction between the sliding material and the third body layer, the wear of which can be described as a “polishing” effect and significantly lower than that encountered by the first zone. The third body film in the second zone will “lift” the front zone away from the contact slightly, reducing the load carried by this high wear region, and therefore the overall wear rate of the contact.


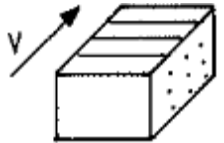
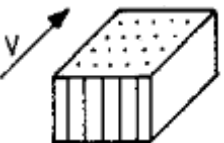
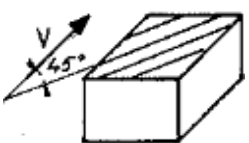


**Figure 1.10** Two-zone contact (Play & Godet, 1977)

In reciprocating motion, if the length of the specimen is greater than  $2 \times d$  from Figure 1.10, the centre of the specimen will only ever interact with a transfer layer, which explains the observation of Play (1985) that transfer films on both the specimen and the counterface are significantly thicker at the centre of the contact area.

Godet & Play investigated the effect of fibre alignment with respect to sliding direction in an epoxy-filled carbon fibre composite. They noted that if the fibres were aligned normal to the sliding direction, the coefficient of friction was reduced by 25% compared to the case in which fibres were aligned parallel to the sliding direction, as shown in Table 1.1. If the fibres are oriented at 45 degrees to the sliding direction however, the coefficient of friction is only increased by 4% compared to the case in which the fibres are parallel to the sliding direction.

**Table 1.1** Coefficient of friction dependent on fibre orientation (Godet & Play, 1975)

Fibre Alignment	Coefficient of friction
	0.16
	0.12
	0.19
	0.125

Kennedy et al. (1975) investigated the factors affecting the wear of polyethylene against a steel counterface. They found that wear rate decreases when moving from a very rough surface to a smoother surface, but found a point at which increasing the smoothness of the surface further increases the wear rate. In the case of polyethylene on steel, they found this roughness to be  $0.1 \mu\text{m Ra}$ . They also found that the coefficient of friction is decreased with rougher surfaces. They rationalised this as due to the combined effect of adhesion and third body thickness. They stated that the main frictional mechanism between polyethylene and steel is adhesion, which is significantly reduced by the formation of a third body film. As a rougher surface allows the third body film to be generated and held between the asperities, this reduces the effect of adhesion and therefore the coefficient of friction. They did not

however extend this hypothesis to explain the increase in wear rate against very smooth surfaces, though as the trends are the same when surface roughness is compared to both coefficient of friction and wear rate, such an extension would seem logical.

The work of Bramham et al. (1980) identified a range of fluids which were detrimental to overall bearing life, and showed that their effect was increased when a constant supply of the fluid was introduced. They presented one possible explanation for this as the fluid inhibiting the creation of a transfer layer, or continuously removing the one already formed (Lancaster, 1972). This suggestion is supported by micrography of the surfaces compared to the same materials examined in dry conditions (Evans, 1978). This further underlines the importance of the creation and maintenance of a transfer layer in the performance of self-lubricating materials. Moreton (1983) uses the effects of fluids inhibiting the creation of transfer layers to explain the huge detriment to performance experienced with some materials when operating in near 100% humidity, where water condensation at or near the contact zone is possible.

## **1.6 Computer Modelling of Self-Lubricating Bearings**

Computerised modelling is a relatively new technology in the field of self-lubricating bearings, and has only recently started to be applied. Metal-on-metal journal bearings are relatively simple, and can often be modelled using conventional continuum mechanics principles. The introduction of a composite self-lubricating liner, with non-homogenous material properties, increases the complexity of the modelling problem significantly.

Fortunately, Finite Element Modelling (FEM) is an accessible method of computationally modelling structures, with many commercial software packages available to carry out simulations. Modelling is possible on the scale of the fabric itself using finite element techniques (Parsons et al., 2010), but it is currently considered unrealistic to model the bearing liner on the scale of the bearing with the necessary degree of detail.

Cao et al. (2010) investigate the effect of including heat generated due to friction on the contact stresses in a spherical self-lubricating bearing, with a PTFE-based composite fabric liner. They compared the results of theoretical temperature analysis and FEM temperature analysis, and found good agreement between both techniques and experimental data. They found that the peak contact stress in the bearing was increased by approximately 30% due to the inclusion of the effect of expansion due to frictional heating.

Liu and Shen (2010) propose a mathematical method of combining the elastic properties of yarns in a composite fabric containing PTFE and C-50 carbon. They obtained very good agreement between the elastic modulus of the fabric found by computational and experimental methods (0.63% difference) and good agreement for the Poisson's ratio (12.74% difference).

Some studies have considered the liner as a bulk material, with elastic (Li et al., 2008) or hyperelastic (Yang et al., 2010) properties. These properties are usually selected after matching to the experimentally derived stress-strain curve. Li et al. (2008) modelled a self-

lubricating spherical plain bearing with a fabric bearing liner containing Aramid and PTFE with a synthetic resin. This liner was considered as a laminate, which contains the correct proportions of the materials but neglects the weaving pattern. The bearing was modelled as three parts – the inner ring, the bearing liner and the outer ring. The stiffness and Poisson's ratio of the liner was calculated by combining the stiffness and Poisson's ratio of the Aramid and resin, as the PTFE was ignored due to its low volume fraction. These properties were then applied to a bulk material representing the liner. This method produced good agreement between experimental and FEM results (<10% variation) for the displacement of an inner ring into the liner material under load.

Yang et al. (2010) used indenter tests to determine the stress-strain relationship for a Kevlar- and PTFE-fibre woven composite with synthetic resin, and chose a mathematical definition that was close to the stress-strain relationship. A spherical plain bearing was modelled, with and without the bearing liner included in the model, and for the case where it was included, the mathematical stress-strain relationship was applied to the material. They found that there was a considerable increase in the contact area when the liner was included, and therefore a significant reduction in the peak contact pressures for the model with the liner at a given load. They proposed that the stiffness of the liner can contribute to increased performance of the bearing (load capacity, service life), and that there is an optimum stiffness. Unfortunately there is no further discussion of how this could be identified, nor are any data comparing liner stiffness to bearing service life detailed.

Potentially, these models can provide information on how modification of the properties of



the fibres and resin affect the stiffness of the liner, but they cannot give any indication of the effect on friction and wear of the liner. Other modelling methods have approached the problem of predicting friction and wear. Bortoletto et al. (2012) use a custom script in a commercially available finite element software to describe the removal of material due to wear in a dry sliding pin-on-disc test incorporating an Archard wear law formulation. They calculate friction in the model by calculating the tangential force needed to move the pin and dividing it by the normal load. However, it is not entirely clear what governs the force needed to move the pin, as they do not specify a coefficient of friction between the pin and the disk. In any case their results using this method lead to predicted coefficients of friction between 40% and 70% lower than those observed in experiments. Their results for wear show a similar magnitude of error, but consistently over-estimate the wear depth.

The discrete element modelling approach has an advantage over finite element modelling in that wear is very easy to simulate (Richard et al., 2007). In the discrete element method, a material volume is represented by a cluster of spheres, for which interactions are specified. The method models not only wear, but allows the movement of third bodies to be tracked (Fillet et al., 2005). The method also enables thermal effects to be studied in a similar manner to the finite element method (Richard et al., 2008). These theoretical methods do not appear to have been verified experimentally, however, and there are concerns regarding the assumptions made on the size and distribution of wear particles, which are partly governed by user inputs, which can have a major effect on the predictions of the model (Fillet et al., 2005).

## 1.7 Future Development of Bearing Liners

As self-lubricated bearing tribology has progressed, attempts have been made at improving the performance of bearing liners by using new materials. Li & Ran (2010) found carbon-fibre reinforcement to give improved wear performance over other reinforcement materials in non-woven composites. Considerable work has also been undertaken in evaluating the performance of different resins in woven materials. Verma et al. (1996), for example, found improved performance of a phenolic resin in a woven composite when the resin was chemically modified with Poly Vinyl Butryal (PVB). The specific wear rate ( $\text{mm}^3\text{N}^{-1}\text{m}^{-1}$ ) was reduced by between 20% and 80% in comparisons with non-modified phenolic resin, with a corresponding reduction in coefficient of friction of between 10% and 50%, dependent on sliding velocity. The modified resin possesses around 5% higher tensile strength and flexural modulus, with 7% reduced flexural strength. Importantly, the modified resin has an 80% higher tensile modulus, and 75% higher Charpy impact energy ( $\text{kJ m}^{-2}$ ). The authors concluded that the reduction in wear rate was due to the increased ductility of the resin. There was also a reduction in bulk surface temperature rise of between 20% and 50% observed through use of the modified phenolic resin, which is a considerable factor in the context of friction and wear of thermosetting materials (Yang et al., 2009). The effect of temperature on the pattern of friction and wear observed is discussed. In particular the authors identify a critical temperature above which “charring” of the resin is observed, the effect of which is to significantly increase the friction coefficient and wear rate. The theoretically ideal temperature is one which is high enough to reduce the friction coefficient and wear rate by increasing the ductility of the resin, but not so high as to cause “charring” and bring about a reduction in the material properties of the resin.

Investigations into the performance of alternative resin materials are of particular commercial importance at the present time, as the many phenolic resin systems utilise formaldehyde, the use of which is coming under increasingly strict regulations (Wagner, 2010). It is therefore timely to develop new methods of tribologically simulating self-lubricated bearings which can be used as screening tools for the rapid evaluation of candidate material combinations.

## **1.8 Aims & Objectives**

The project aims to fulfil the following objectives:

- To produce a finite element model of a composite dry bearing liner, providing a representation of all constituent materials.
- To use this finite element model to inform a model of the variation in friction coefficient over the wear life of the bearing liner, which will take into account the changing proportion of the constituent materials in contact with the counterface.
- To verify this friction model against experimental data obtained from a bespoke flat-on-flat sample wear test bench.
- To model the useful wear life of a complete “dry” spherical plain bearing containing the bearing liner, and verify predicted wear against results from full-scale bearing tests undertaken outside of the project. The approach will apply lubricated journal bearing theory to a “dry” spherical plain bearing.

There are two aspects to the project which are novel – firstly, the modelling of the friction

coefficient of a multi-material tribological contact and its variation throughout the wear life of a composite material. Secondly, the modelling of the wear life of a complete “dry” spherical plain bearing using lubricated journal bearing theory.

## **2. Modelling the Weave**

### **2.1 Objectives**

Composite bearing liners have been available since the late 1960s (Lancaster, 1982). Physical testing of new bearing liners is both costly and time-intensive, therefore methods of screening potential new composites are urgently sought.

There are three key performance characteristics of bearings:

- Load-bearing capacity – dependent on the stiffness and ultimate tensile strength of the component materials.
- Efficiency – dependent on the overall friction coefficient of the bearing.
- Lifespan – dependent on the wear rate and any failure modes.

There are additional characteristics of bearings required for certain applications, such as resistance to corrosion and contaminants, and the ability to operate at extreme temperatures.

An improved bearing liner would show improvements in one or more of the key performance characteristics. In order to model any of these parameters for a new fabric before the prototyping phase, some method of simulating the fabric's response under realistic conditions is required.

It was decided that a finite element analysis (FEA) model should be developed to simulate a composite bearing liner, using the commercial finite element software DSS Abaqus. This would allow estimation of the three key bearing characteristics in the following way:

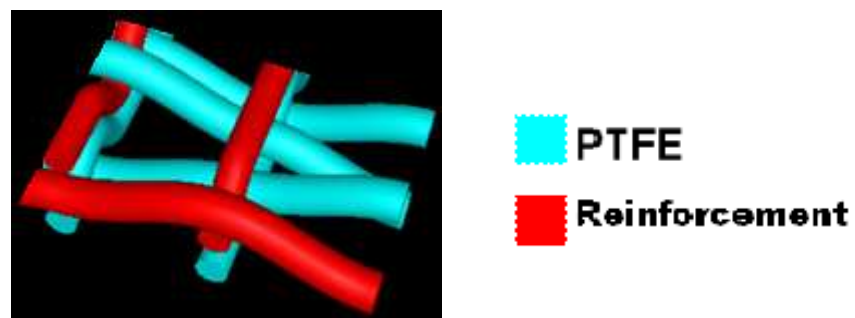
- Load-bearing capacity – a finite element model of the constituent materials of a bearing liner would allow an overall stiffness to be calculated.
- Efficiency – a friction model would use the variation in contact pressure and the proportion of materials in contact over the wear-life of the liner to estimate the friction coefficient corresponding to different amounts of wear.
- Lifespan – the wear rate of a composite material is affected by the variation in stiffness at different amounts of wear.

To evaluate the effectiveness of models of this sort, it would be necessary to test them in terms of a pre-existing material, so that information on the three key performance characteristics of the bearing liner could be obtained. The end goal of these models (beyond the scope of the project) is to develop a method of screening potentially new composite fabrics.

## 2.2 Weave Visualisation

It was anticipated that the simplest finite element model of the test bearing liner is that of a “unit cell” – the smallest repeating geometry – subject to boundary conditions to make it behave as part of a much larger sheet of the material. In order to preserve commercial confidentiality and intellectual property, only a portion of the unit cell is illustrated in this version of the thesis.

While the specification of the fabric was obtained from manufacturing specifications, the fabric was still difficult to visualise due to its complex structure. Texgen is software developed by the University of Nottingham to “model the geometry of textile structures” (Texgen, 2013). This software was used to develop a visualisation of the test fabric in 3D, shown in Figure 2.1.



**Figure 2.1** Visualisation of part of the test fabric weave, using Texgen

## 2.3 Finite Element Model

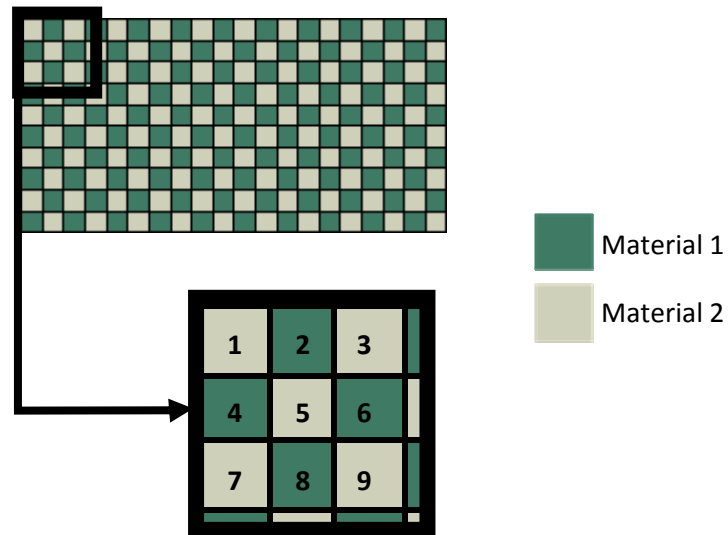
### 2.3.1 Unit Cell Geometry

Finite element models were first developed in two dimensions, to evaluate methods for specifying a composite material structure. DSS Abaqus finite element models contain “parts” – individual components which are either free to act independently or are constrained in some way to simulate part of a larger assembly. Parts generally have a single material property for the whole part even if the part is made of a composite material, in which case non-homogenous material properties can be specified. In order to model the test composite unit cell as one part on the micro scale, different material properties had to be specified for different sections of the part. It would have been possible to create the “unit cell” from multiple parts representing the yarns and the resin and specifying their interactions, but it was anticipated that this would create a complex, inflexible model. A method was necessary to specify the composite material structure using only one part, but containing multiple material assignments.

An initial attempt to create multiple material definitions was performed element-by-element. Due to the regular numbering structure for elements in regular meshes in DSS Abaqus, elements could have material properties specified by creating sets of element numbers, identifiable from their predictable pattern. Figure 2.6 shows a single “part” made up of two alternating material definitions, specified by element number. Figure 2.2 also shows an illustration of how the predictable pattern of element numbering allows sets of element numbers to be built to create such a “part”. A weave-like structure created using this method

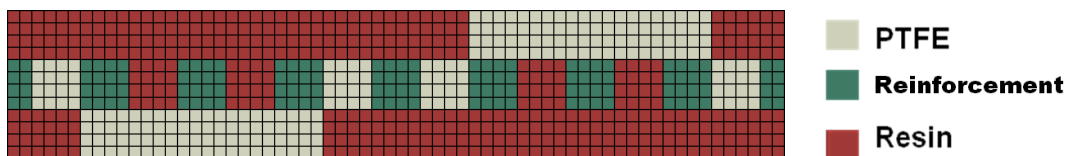


is illustrated in section Figure 2.3.



**Figure 2.2** A single “part” made up of two materials, with an area magnified showing an example of the element numbering system

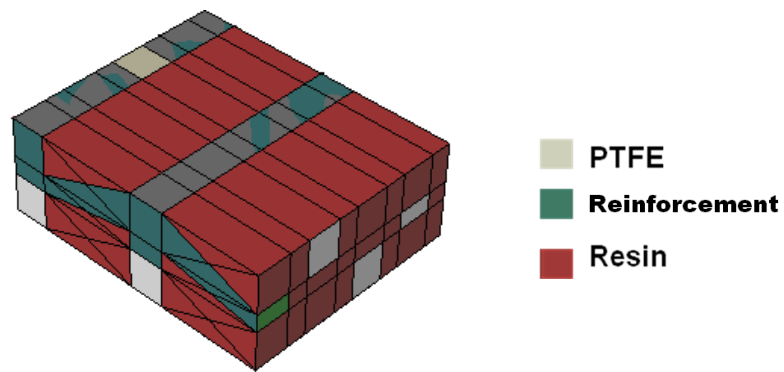
*In this example, 2 sets of element numbers would be created – 1,3,5,7,9 for Material 2 and 2,4,6,8 for Material 1.*



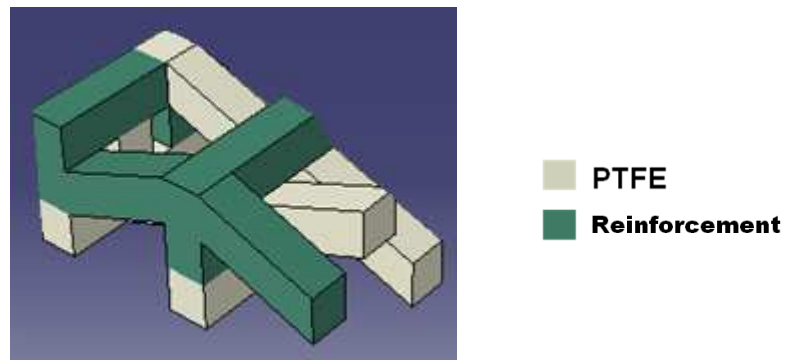
**Figure 2.3** A weave-like pattern specified by element number

This method was found to have two limitations which prevented it from being extended to 3D models. Firstly, element numbering is mesh-dependent. Changing the mesh density changes the size of elements, therefore a given area would have different numbers of elements. Using this method new sets of element numbers had to be created every time a different mesh was specified. Secondly, when less regular meshes were used, as required when a mixture of element types were used, the mesh numbering pattern became less predictable and it was very difficult to build the necessary element number sets.

A more flexible method of specifying sections and materials was developed which used a bespoke script with a series of commands, written in the Python programming language. The make-up of the script is described in detail in Chapter 3. This script creates a 3D Finite Element model of the weave with a structure representative of the test composite fabric. Figure 2.4 shows the “unit cell”, made up of PTFE yarns and reinforcement yarns in a resin matrix. Figure 2.5 is the same “unit cell” but with the resin hidden, to show the weave structure, which is compared with the weave structure visualised using Texgen (Figure 2.1).

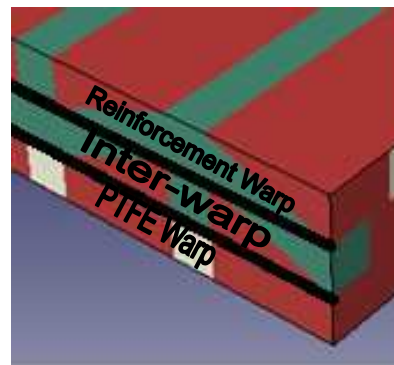


**Figure 2.4** Part of a “unit cell” of test composite fabric, made up of PTFE and reinforcement yarns in a resin matrix



**Figure 2.5** Part of a “unit cell” of test composite fabric, as Figure 2.4 but with resin hidden to show the weave structure

The geometry of the unit cell is designed around the concept of dividing the test composite into three “layers” – a reinforcement warp layer; a layer of resin to allow the weft to pass between the warp yarns; and a PTFE warp layer. In application, the PTFE warp layer would be the layer initially in contact with the moving part. Figure 2.6 shows this division into layers on the “unit cell”, and Figure 2.7 shows a cross-section through the weft of the test fabric, alongside the same diagram but with only 1 warp thread shown.

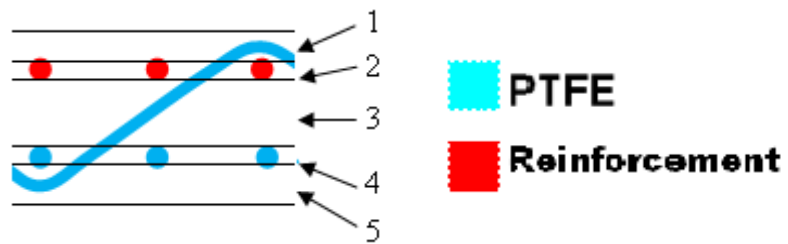


**Figure 2.6** Part of unit cell showing three “Layers” of Finite Element Model



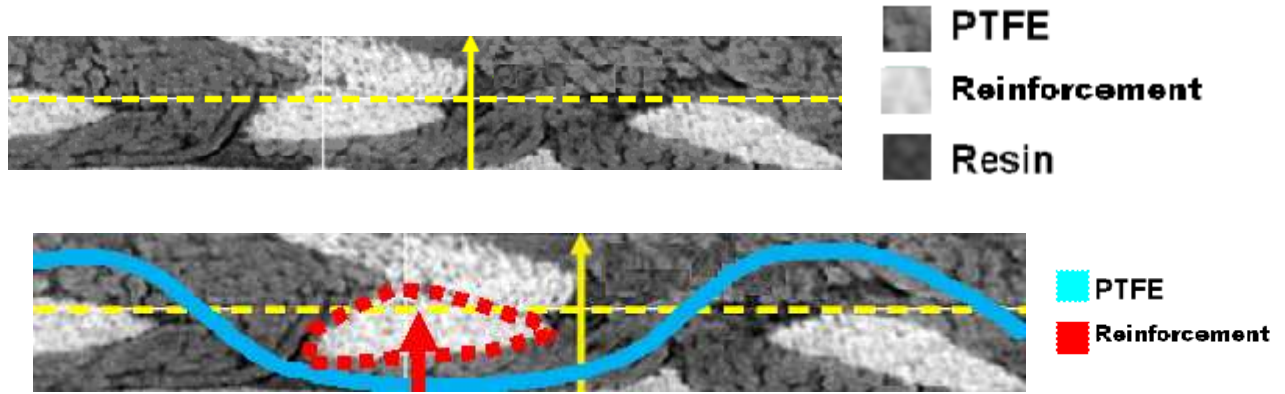
**Figure 2.7** Part of a cross-section in the warp direction showing only one weft thread

The cross-sectional diagram in Figure 2.7 implies the need for five “layers” as shown in Figure 2.8 – a layer for weft threads passing over the reinforcement warp (1); a layer for the reinforcement warp (2); a layer between the reinforcement warp and PTFE warp (3); a layer for the PTFE warp (4); and a layer for weft threads passing underneath the PTFE warp (5).



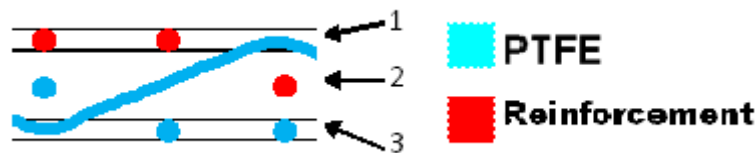
**Figure 2.8** Part of a cross-section through the warp, showing five layers - a layer for weft threads passing over the reinforcement warp (1); a layer for the reinforcement warp (2); a layer between the reinforcement warp and PTFE warp (3); a layer for the PTFE warp (4); and a layer for weft threads passing underneath the PTFE warp (5).

It was seen from tomography of the test composite fabric that where a weft thread passes over a warp thread, it displaces the warp thread into the inter-warp layer, hence there is no need for layers 1 and 5. This is highlighted in Figure 2.9, featuring a magnified view of a weft thread being pulled into the inter-weft layer.



**Figure 2.9** Tomography showing cross-section through the weft (top), with warp thread highlighted in blue, along with reinforcement weft thread which has been displaced into the inter-weft layer in red

Figure 2.10 shows the three-layer approach based on Figure 2.9, showing the reinforcement warp layer (1); the inter-warp layer (2); and PTFE warp layer (3). Figure 2.11 shows this same structure in the finite element “unit cell”.

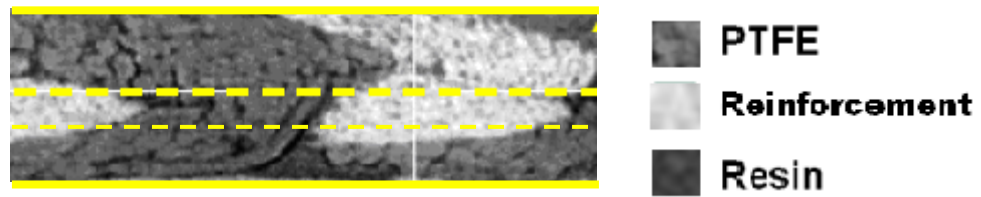


**Figure 2.10** Part of a cross-section through the warp, showing 3 layers - the reinforcement warp layer (1); the inter-warp layer (2); and PTFE warp layer (3).

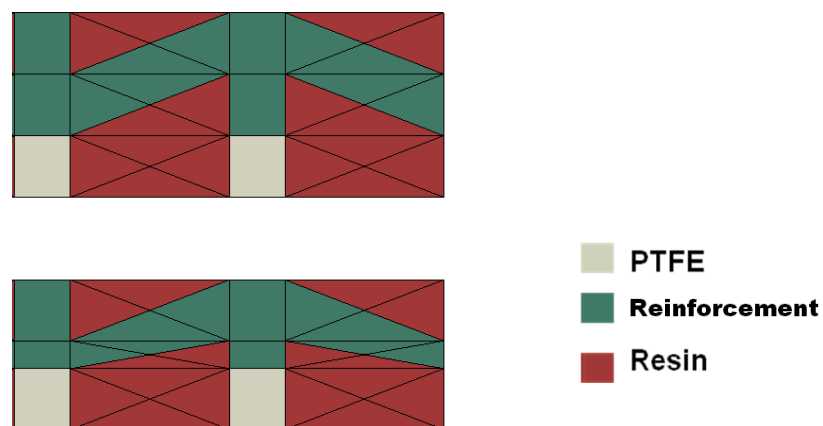


**Figure 2.11** Part of a cross-section through the warp of the finite element “unit cell” showing only one weft thread, with displaced warp threads and layer divisions highlighted

From examination of the tomography of the test composite fabric, it was also found that the inter-warp layer was much thinner than the two warp layers. Figure 2.11, for example, shows the dimensions of these layers superimposed on the test tomography, with the yellow measurement lines in the figure taken as average heights; for example the top line represents the average height of the top surface across a sample. The figure shows the reinforcement warp and PTFE warp layers are thicker than the inter-warp layer. Figure 2.12 shows the FEA model with three equal layers and in the modified form with a reduced inter-warp layer thickness.

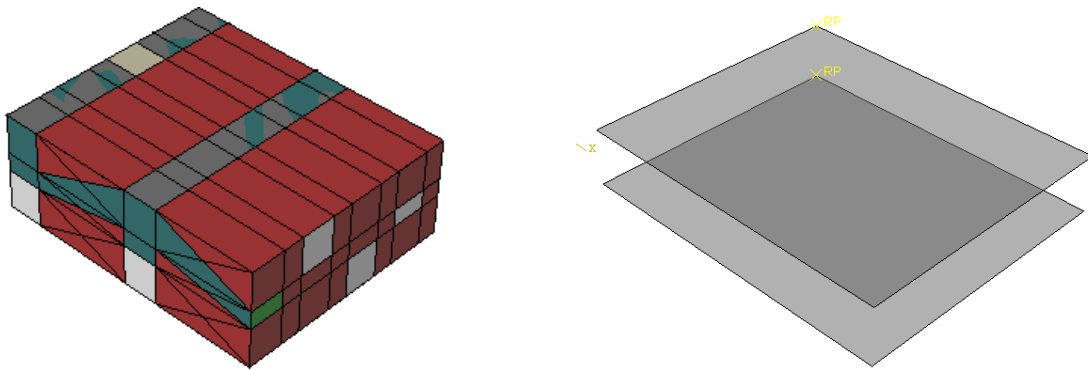


**Figure 2.11** Tomography showing cross-section through the weft of the test composite fabric



**Figure 2.12** Part of a cross-section through the weft of test composite “unit cell”, with three equal layers (top) and reduced inter-weft layer thickness (bottom)

The full unit cell was then assembled between two rigid planes on the top and bottom. The top plane has a uniform pressure over its top surface of  $1 \text{ N/mm}^2$  and is only allowed to displace in the  $y$ -direction (perpendicular to the plane). The bottom plane is constrained in all directions to prevent any movement. This set of constraints and loading represents compression of the composite fabric between two flat platens, shown in Figure 2.13. Contact was therefore simulated between the two rigid planes and the unit cell. The simulation gives a contact pressure distribution on the bottom (contact face) surface of the unit cell, which will vary based on the stiffness of the materials in contact and the materials directly above them. The results of these simulations are discussed in Chapter 5.



**Figure 2.13** Part of “Unit cell” assembled between two rigid planes (left) with “unit cell” hidden (right) to show only rigid planes



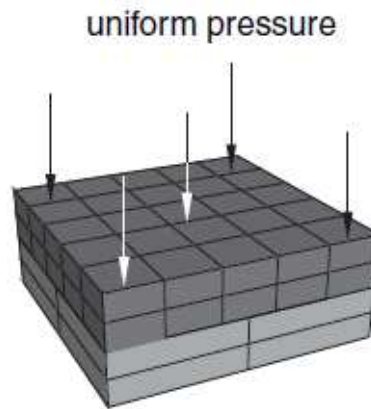
### 2.3.2 Contact Settings and Element Selection

DSS Abaqus offers a wide range of options for specifying contact in a model, together with a range of element types. Not all possible options for contact and element selection are discussed in this section, as full information can be found in the DSS Abaqus User Manuals. The contact conditions for the finite element model are relatively simple compared to some more complex models DSS Abaqus is capable of simulating, therefore the settings used are close to the recommended default settings. This section discusses only the contact controls which were changed from the default settings, or where there is no default setting. The selection of elements is also discussed, as certain element types are unsuitable for contact modelling.

Contact between two bodies in DSS Abaqus is defined by a master and slave surface, with the condition that slave nodes cannot penetrate a master surface, but master nodes can penetrate a slave surface. It is recommended that the master surface is defined as the more coarsely meshed surface. In this model, the two rigid planes were selected as master surfaces, and the unit cell faces were defined as the slave surfaces.

DSS Abaqus offers two options for contact discretization – node-to-surface and surface-to-surface, and two options for contact formulation – small-sliding and finite sliding. Except in borderline cases where convergence is difficult, DSS Abaqus recommends the use of surface-to-surface contact discretization for maximum accuracy. Figure 2.14 shows an excerpt from the DSS Abaqus manual, comparing the two contact discretization methods and showing the

surface-to-surface method to be at least an order of magnitude more accurate.



**Figure 34.1.1-4** Test model for comparison of different master and slave surface designations.

The bottom block is fixed to the ground, and a uniform pressure of 100 Pa is applied to the top face of the top block. Analytically, the top block should exert a uniform pressure of 100 Pa on the bottom block across the entire contact interface. Table 34.1.1-1 compares the Abaqus analysis results for different contact discretizations and slave surface designations.

**Table 34.1.1-1** Error (from analytical results) for various discretization/slave surface combinations.

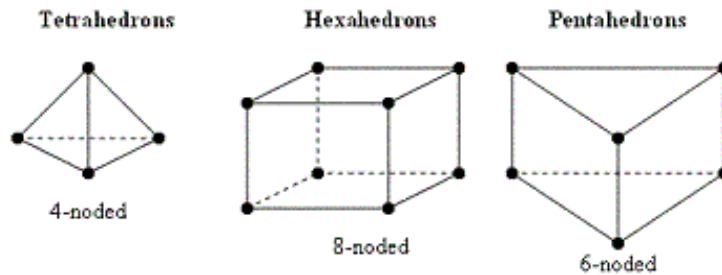
Contact discretization	Slave Surface	Maximum error in CPRESS
Node-to-surface	Top block	13%
	Bottom block	31%
Surface-to-surface	Top block	~1%
	Bottom block	~1%

**Figure 2.14** Contact discretization methods and their accuracy (DSS Abaqus, 2012)

There are two options available for contact formulation – small-sliding and finite-sliding. Small sliding is a contact approximation method designed to reduce the solution computing time, but it can produce results which are not physically meaningful if some sliding is occurring at the interface. The finite sliding method is, by comparison, more robust, and

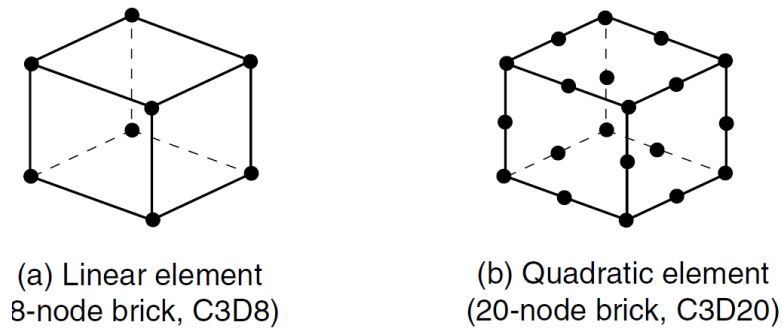
highly recommended for all contact problems (DSS Abaqus, 2012). In this model, the finite sliding formulation is used in both contact interfaces between the “unit cell” and the rigid planes.

DSS Abaqus offers three possible 3D element shapes – tetrahedral (“tet”), hexahedrons (“brick”) and pentahedral (“wedge”), shown in Figure 2.15.



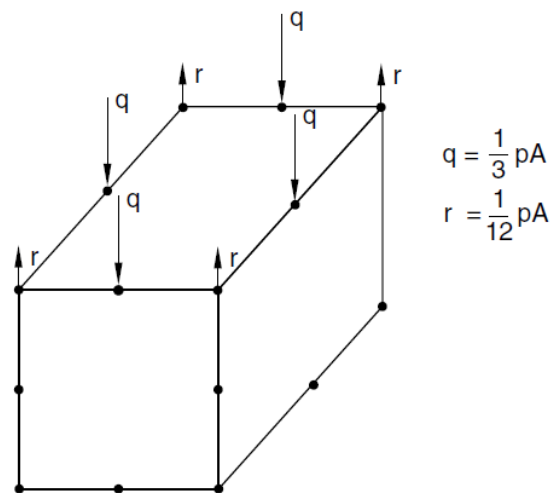
**Figure 2.15** 3D Element types (left to right) – tet, brick and wedge (Moreno, 2012)

Each element type has two main derivatives – first-order and second-order. First order elements have a node at each vertex of the element; therefore in the case of a six-sided brick element there are eight nodes. Second-order elements also include a node at the midpoint of each side, so in the case of a six-sided brick element there are twenty nodes, as illustrated in Figure 2.16.



**Figure 2.16** First-order and Second-order brick elements showing the number and position of nodes

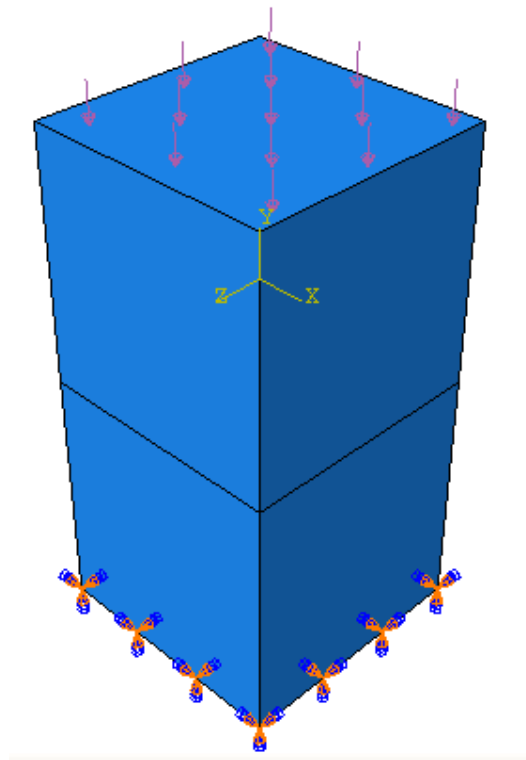
Second order elements are generally more accurate for modelling stresses, but their use incurs a computational cost penalty. For the application of a contact pressure to a brick element, in the case of the first-order element, the pressure is equally divided amongst the 4 nodes in contact. In the case of the second-order element however, the pressure is not equally distributed amongst the eight nodes in contact, as shown in Figure 2.17.



**Figure 2.17** Equivalent nodal loads produced by a constant pressure on the second-order element face in a contact simulation

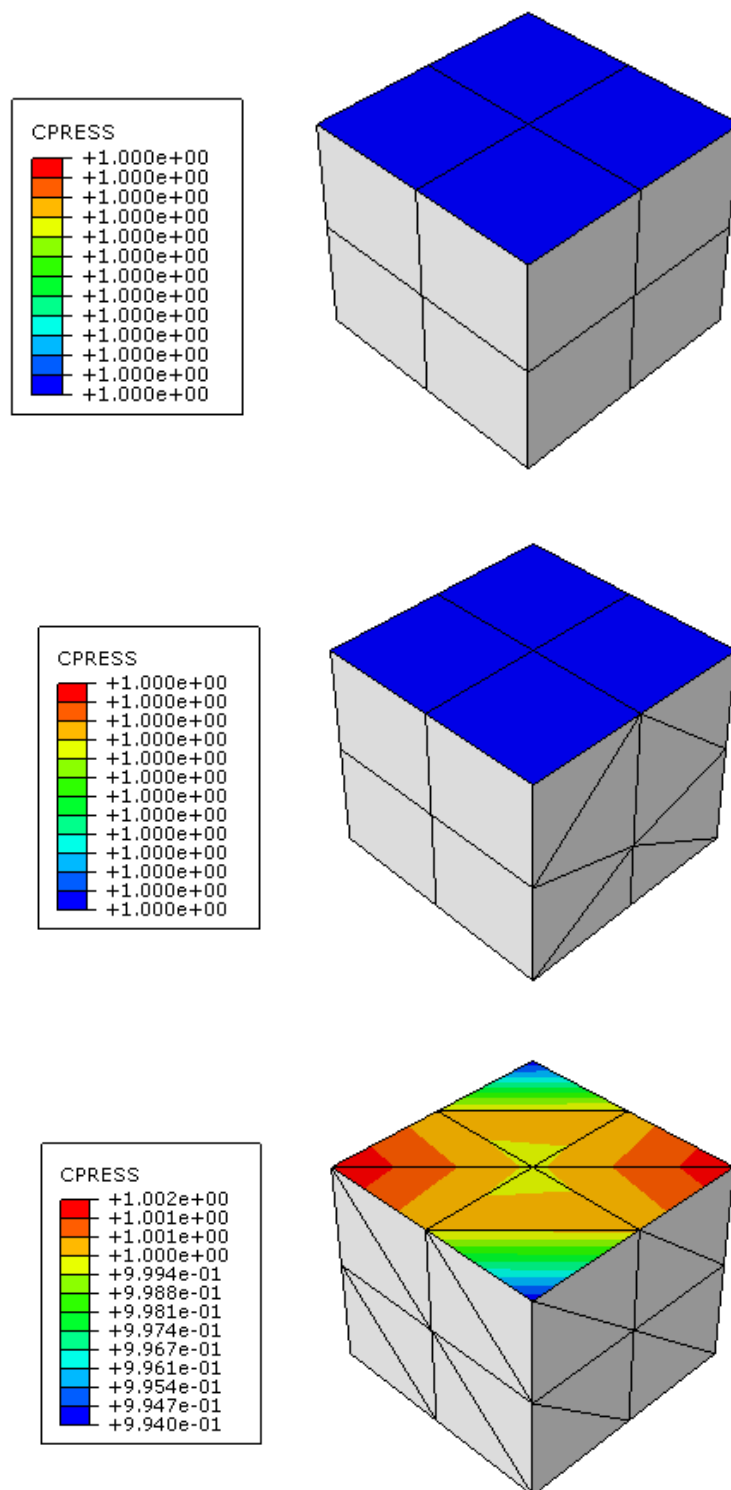
As the output of this finite element model would need to be processed and understood outside of the DSS Abaqus Visualisation program, first-order elements were chosen so that pressures values output by node would be more representative of the contact stresses.

A simple model of two equal sized blocks was created with a pressure of 1Pa on the top face of the top block, with the bottom block constrained in all directions on the bottom face, shown in Figure 2.18. This was coarsely meshed using tet, brick and wedge elements to evaluate their performance in contact modelling.



**Figure 2.18** Finite element model used to test element types for contact, showing two cubes with contact along their interface, a pressure applied on the top face of the top block and encastre boundary constraints on the bottom face of the bottom block

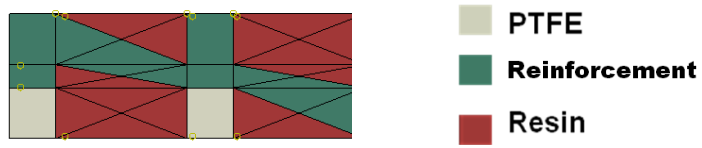
The results of the analysis are shown in Figure 2.19. Both brick and wedge elements produced a uniform pressure distribution as expected, whereas the tet elements produced a non-uniform pressure distribution, with variations of up to 0.6% from the mean pressure value. This small deviation in contact pressure, along with possible problems with shear locking in non-linear analyses such as contact (Puso, 2006), led to tet elements being disregarded as suitable elements to mesh the unit cell.



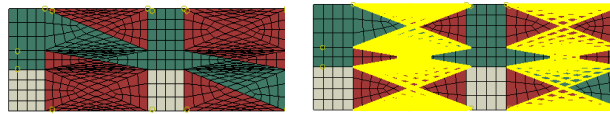
**Figure 2.19** Pressure distributions for brick and wedge elements (top and middle) and tet elements (bottom) for the same finite element model

First-order elements were used throughout the unit cell. Quadratic elements could not be used in areas away from the contact without significantly increasing the complexity of the model due to the need for complex tie interfaces between first- and second-order elements. Wedge elements were used in the weaving sections of the model, as these are accurate in contact calculations, and are also able to fit into the triangular sections of the model without extreme element distortion. Brick elements were used to represent the weft thread areas. Figure 2.20 shows a cross-section through the weft of the finite element model, with a reinforcement warp yarn shown, and no mesh. Figure 2.21 shows the same model meshed only using brick elements, alongside the same mesh with elements highlighted in yellow where there is enough distortion to potentially effect the accuracy of the results. Figure 2.22 shows the mesh that was used in the unit cell, which consists of brick elements for the weft thread areas (highlighted in orange) and wedge elements used for all other areas (highlighted in blue). Wedge elements were used in the areas with triangular sections as their native shape lends itself to use in triangular sections.

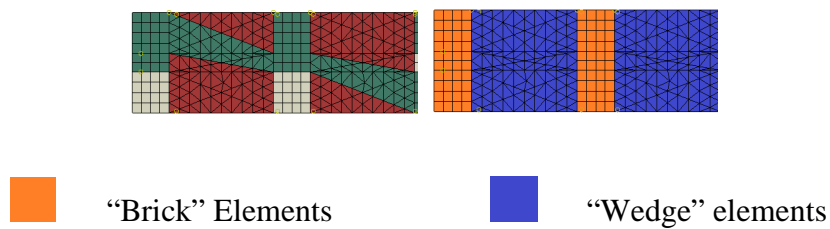




**Figure 2.20** Part of a cross-section through the warp showing reinforcement weft thread without mesh



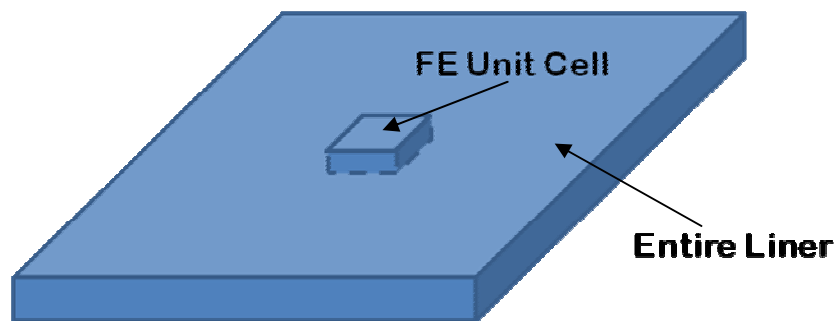
**Figure 2.21** Part of a cross-section through the warp showing reinforcement weft thread meshed using brick elements (left) alongside the same mesh with excessively distorted elements highlighted in yellow (right)



**Figure 2.22** Part of a cross-section through the warp showing reinforcement weft thread meshed using wedge and brick elements (left), with brick elements highlighted in orange and wedge elements highlighted in blue (right)

### 2.3.3 Harmonic Boundary Conditions

Once a representative unit cell of the test composite fabric had been created, boundary conditions had to be specified which would make the unit cell behave as if part of a much larger overall liner, as illustrated in Figure 2.23.

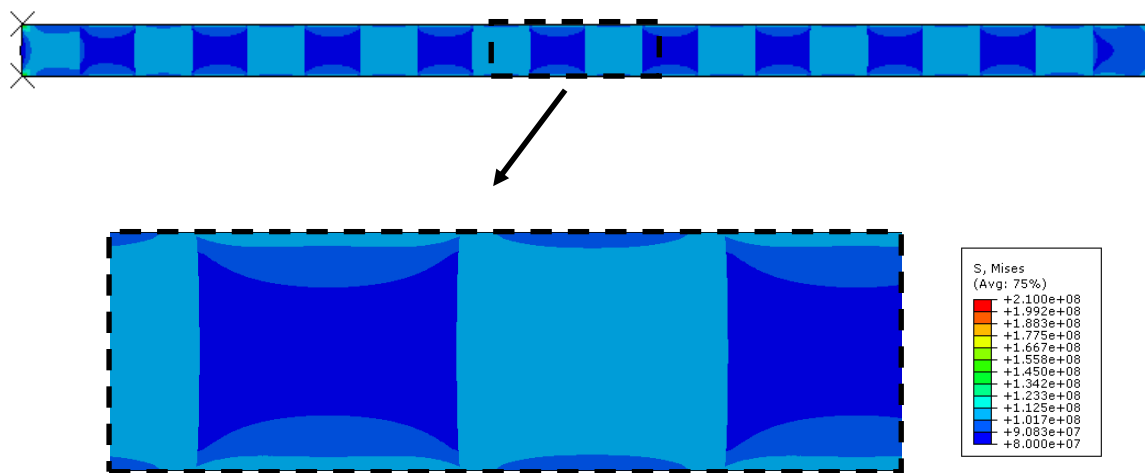


**Figure 2.23** “Unit cell” displayed as part of a larger liner

Figure 2.24 shows a finite element model of a block with a repeating pattern of material assignment compressed between two platens. The bottom platen is fixed, and the top platen is constrained to move only in the y-direction. The top platen is displaced to give a compressive strain of 0.9. The block has a height of 1, and a length of 20, with each section possessing the dimensions of  $1 \times 1$ , each with 10,000 elements. The block has a repeating pattern of material assignment, with both materials having the same stiffness but with Material 1 having a Poisson's ratio of 0.3 and Material 2 having a Poisson's ratio of 0. This means that sections with the properties of Material 1 will have edge effects, and those with Material 2 will not. Figure 2.25 shows the stress contours produced by this simulation, with a close-up of a repeating unit cell at the centre of the part, away from any edge effects.

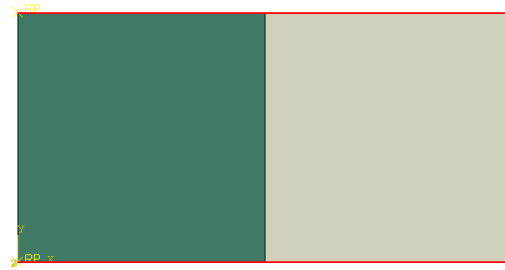


**Figure 2.24** Model of block with repeating pattern of material assignment, Material 1 in green and Material 2 in cream, compressed between two platens in red

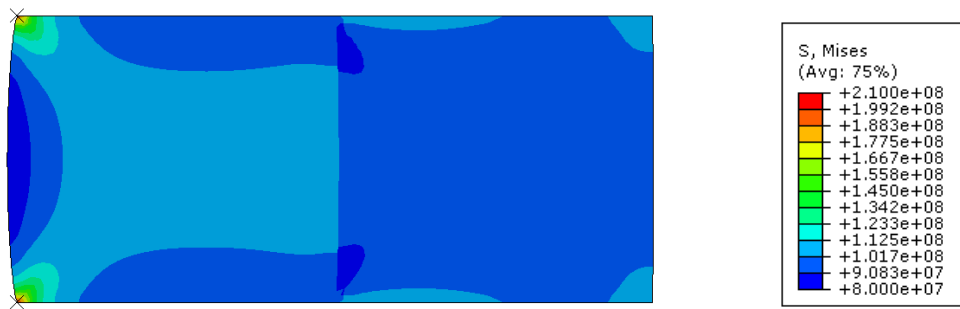


**Figure 2.25** Results of analysis of model in Figure 2.29 (top) with a close-up of central repeating block (bottom)

Figure 2.26 shows a model of a block with only two sections, which is the repeating unit cell of the previous model. This model is given the same compressive strain as the previous model but no additional constraints, and the results are shown in Figure 2.27, which are significantly different to those seen in Figure 2.25. This means that without additional constraints this model is not representative of the behaviour of a unit cell at the centre of the model.

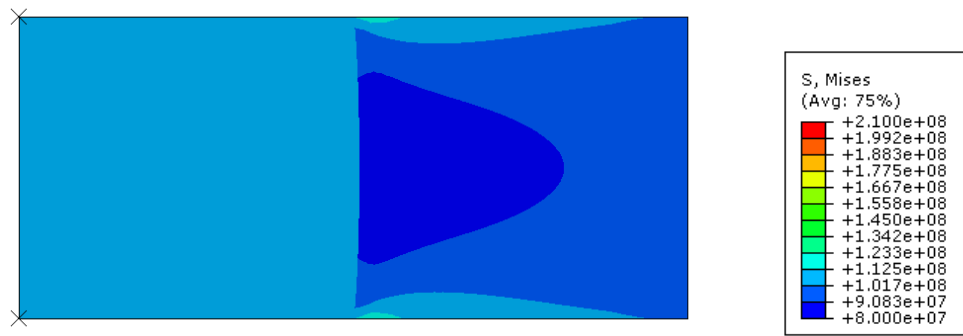


**Figure 2.26** Unit cell with two materials compressed between two platens in red



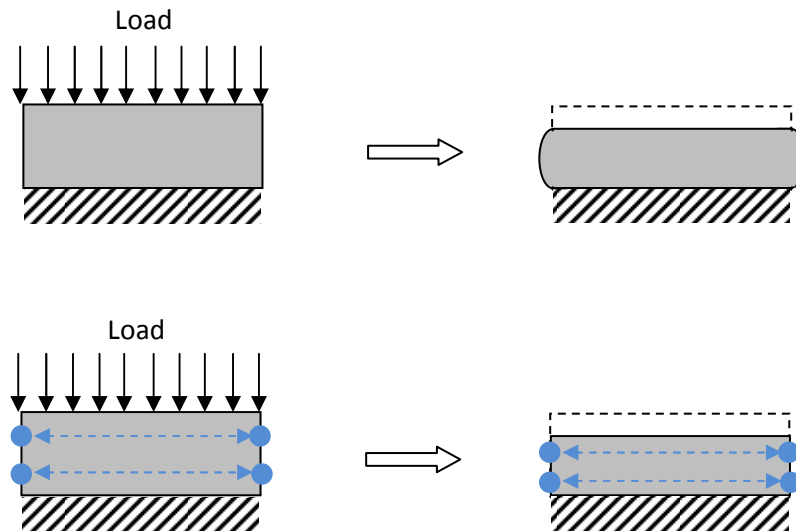
**Figure 2.27** Results of analysis of model in Figure 2.31

Figure 2.28 shows the results obtained using the same model, but with boundary conditions imposed on the far left and right hand edges of the unit cell to stop their displacement in the x-direction. This is again different to the results seen in Figure 2.25, and therefore not representative.

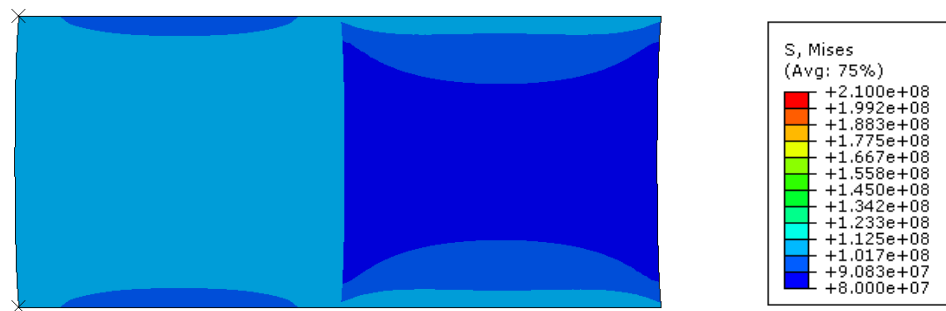


**Figure 2.28** Results of analysis of model in Figure 2.26 but with  $x$ -direction constraint boundary conditions applied to left and right hand side of the block

The model was analysed again, however this time the constraints on the left and right hand sides were changed to harmonic boundary conditions. Harmonic boundary conditions constrain opposite sides of the unit cell to have equal displacement. This was achieved by using DSS Abaqus's "tie" function to keep corresponding points on opposite sides of the block at a constant separation, and remove "edge effects". This works by (in this case) keeping points with the same height but on opposite sides of the block at the same separation in the  $x$ -direction or  $z$ -direction. Figure 2.29 shows a schematic representation of this type of constraint.

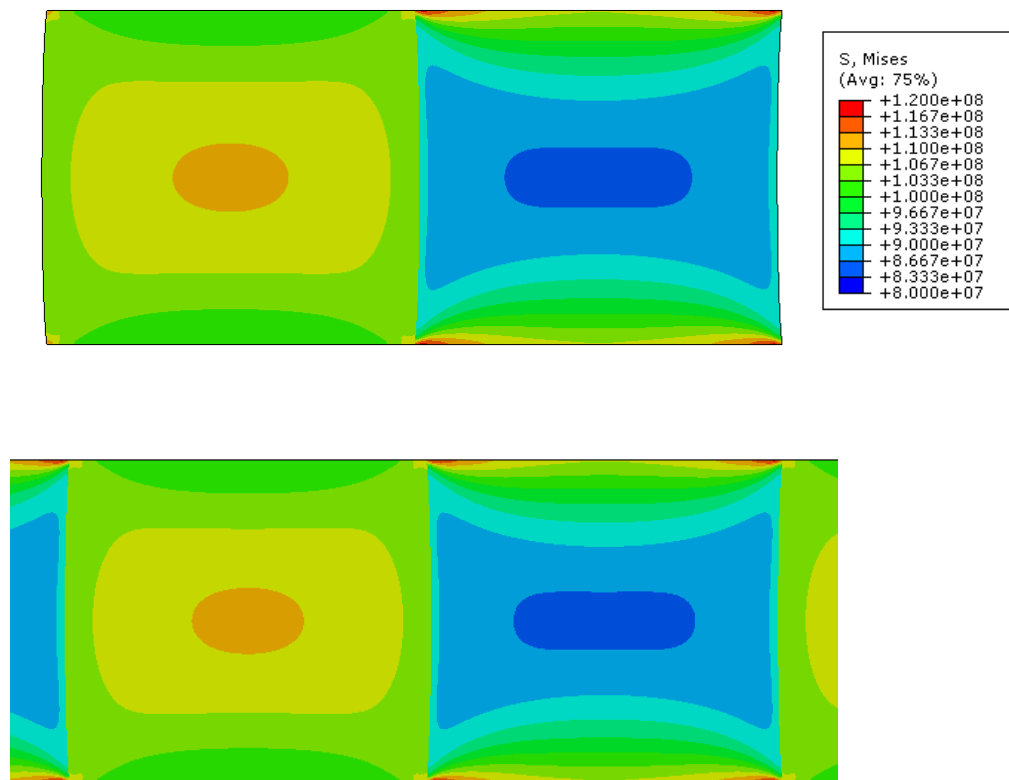


**Figure 2.29** Loading of a block without harmonic boundary constraints, showing Poisson “edge effects” (top) and the same model with harmonic boundary constraints, which removes Poisson “edge effects” (bottom)



**Figure 2.30** Results of analysis of model in Figure 2.26 but with harmonic boundary conditions applied to left and right hand side of the block

Figure 2.30 shows the results of this simulation, which are now very similar to those seen in the larger model in Figure 2.25. Figure 2.31 shows the results of the two simulations with the scale adjusted to increase the detail in the stress contours in the section. The results are very similar. However, there are slight differences in the contours, for example at the top left hand and bottom left hand corners of the unit cell model. The unit cell block however reduced the number of elements in the model by a factor of ten. While it may be possible for the first, larger model to be reduced in size while still isolating the repeating cell at the centre from edge effects, the necessity to have multiple unit cells would mean that a model with harmonic boundary conditions reduced the number of elements by at least a factor of three. Such a reduction represents enormous savings in analysis time, as the relationship between the number of elements and the time taken to perform an analysis is not necessarily linear.



**Figure 2.31** Results of analysis of model as Figure 2.35 (top) and Figure 2.30 (bottom) with scale adjusted to increase detail of contours



## 2.4 Assumptions and Limitations

The following assumptions and limitations apply to the unit cell model, each of which are discussed in this section:

- All threads in the warp direction and all threads in the weft direction have the same cross-section, though there can be a difference between warp and weft threads, and the cross-section of all warp and weft threads is rectangular.
- The weft threads are not of constant thickness when passing through the inter-warp layer.
- There is a smooth, connected weave pattern in the cross-section through the warp, but not in the weft cross-section.

### 2.4.1 Thread Cross-Sections

In the finite element model all threads have a rectangular cross-section. This allows much simpler meshes to be used than if the threads were of circular or elliptical cross-section. The threads in the finite element model represent bundles of hundreds of individual fibres, a level of detail which would have been unrealistic to model on the scale of the unit cell. To account for the fact that the PTFE and reinforcement threads are not of the same dimensions, the actual total cross-sectional area of all the fibres in the threads was calculated from manufacturing specifications of the yarns, allowing for the proportion of resin and reinforcement/PTFE in the unit cell cross-sectional area and the equivalent stiffness for the unit cell thread. The weight of threads are measured in “denier”, a unit of measurement of the linear mass density of yarns, defined as the mass in grams of 9,000 m of the thread. The

origin of this traditional unit of measurement is from weaving, where one strand of silk has a mass of approximately 1 gram per 9,000 metres (Brossard, 1997). From the linear mass density of the fibres, and the density of the material, the total cross-sectional area of all filaments in a yarn may be calculated.

The yarns are made up of many filaments, which will have small gaps between them. Denier is a more useful way of calculating the total cross-section of all the filaments making up the yarn than physically measuring it, as it is not affected by how tightly the fibres are wound and how much space is left between fibres in a single yarn. The total cross-section of all fibres in a yarn is calculated by dividing the linear mass density of the yarns (denier) by 9000, to give the mass in grams per metre of thread, then dividing by the density of the material, to give the total cross-sectional area of all threads.

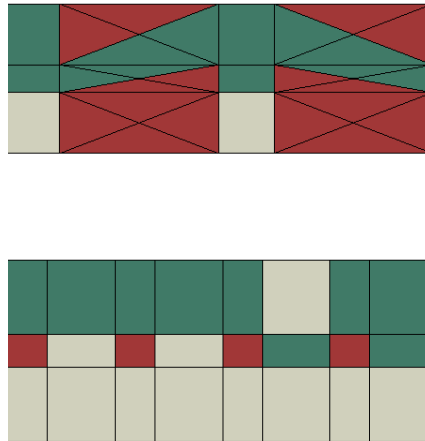
By dividing the total cross-sectional area of the yarns of each material by the cross-sectional area of the threads in the unit cell, the percentage of the area of the thread made up by the yarn material can be calculated. The remaining portion of the “unit cell” thread is assumed to be made up of resin, the simplification being made that there are no air gaps in the test composite fabric. The stiffnesses of the two materials are combined in these proportions to give the representative stiffnesses of the reinforcement and PTFE threads which are found to be in the ratio of 70:1.

### **2.4.2 Variation in Thread Thickness**

The model was originally designed with all three layers having the same thickness, which allowed the cross section of weft threads to remain constant as they passed through the inter-warp layer. Upon examination of X-ray tomography images it was seen that this inter-weft layer was in fact much smaller than expected, and the inter-warp layer was therefore reduced in the finite element model. This was not viewed as having a detrimental effect on predicted response, as the inter-warp layer is predominantly resin, therefore reducing its size brings the proportional amount of resin in the model closer to that seen in the finished liner.

### **2.4.3 Weave Pattern in Warp vs. Weft Direction**

Creating a 2D weave pattern was a relatively simple task compared to being able to create a 3D weave pattern which also allowed for a regular mesh throughout. The method by which the material was divided into sections is described in chapter 3. A limitation of this method is that it could be achieved in the warp cross-section, but not in the weft cross-section simultaneously while using wedge elements. Figure 2.32 shows the thread weaving pattern in the weft and warp cross-section, and the differences in resolution in the two directions.



**Figure 2.32** Part of a cross-section through the warp (top) and weft (bottom) showing the difference in resolution of weave structure

The only way to model a smooth weave pattern in the warp and weft direction was to use tet elements, which are not currently appropriate for modelling contact (see Section 2.3.2). However, developments in the DSS Abaqus software since the commencement of the project mean that tet elements are now regarded as accurate for modelling contact. It should therefore be possible in future to improve this aspect of the modelling.

## **3. Building the Weave Model**

### **3.1 Overview**

The model described in the previous chapter was difficult to create using only the DSS Abaqus graphical user interface (GUI), as points had to be selected which were internal, and many tasks were repetitive. In addition, it was anticipated that the geometry of the model might be changed for future research into other liner materials. A solution was developed which built the FE model of the test liner, while allowing some geometrical parameters of the model to be easily changed.

Python is a freely-available high-level object-oriented programming language, which places particular emphasis on the ease of comprehension of the code (Python, 2013). DSS Abaqus includes a scripting interface, allowing commands to be controlled by scripts written in Python. All actions which can be completed in the Abaqus GUI have an associated Python command. These commands can be applied to a range of entity types including the entire model space, a part, a section of a part, or a point in space.

A useful feature of DSS Abaqus is that the related Python commands for all actions undertaken in the GUI are automatically recorded in a text file. By copying the Python command associated with an action and applying it again, the same action can be repeated.

These commands can be applied individually, or as a longer series of commands.

Python commands can refer to many aspects of a model, including a part, section or point in space. By altering the aspect that a Python command refers to, for example choosing a different part, an action can be repeated and applied to different parts. Additionally, these commands can be used with a specified value, or refer to a variable which can be changed. Through careful modification of a series of Python commands an FE model can be built in Abaqus which will vary based on a user-defined set of input parameters.

Developing a model in this manner has the following advantages:

- The script can be split into user-defined variables and actual commands, which means that the output can be modified without understanding of the underlying commands.
- User-defined variables can be altered to change some parameters of the model such as geometry and materials.
- The model does not have to be stored as the finished product, which can be costly in terms of storage capacity for very large models. By storing the model as a series of commands, the model can be stored much more efficiently, although with the penalty of the time taken to build the model from the script.

In the case of the model of the test composite liner, the first two points are particularly advantageous, allowing the model to be adjusted without knowledge of the commands in the script. The third point is not of particular concern, as the model is very small relative to the

spectrum of finite element models; however it is worth noting for models with an extremely high degree of geometric complexity.

## 3.2 Python Script Structure

### 3.2.1 User Variables

The Python script builds a DSS Abaqus finite element model of the test composite liner unit cell based on a series of parameters controlling some aspects of its geometry. The overall height of the unit cell can be changed, along with the height of the three “layers” of the model. The pitch (distance between yarns) in both the warp and weft direction can be changed, as can the cross-section of the yarns which, as discussed in the previous chapter, is the same for all yarns in both the warp and weft direction. The properties of the materials in the composite can also be changed. The weave structure of the fabric however cannot be changed simply by varying the user-defined variables, as this would require considerable modification of the overall script.

These parameters are stored as the following variables. All dimensions are in mm, and all Young’s moduli are in Pa:

- Height – the overall height of the unit cell
- Threaddia – the diameter of the yarns
- Weftpitch/warppitch – the distance between each yarn in the warp/weft direction
- Heightlub – the height of the “layer” including the lubricant yarns

- Heightreinf – the height of the “layer” including the reinforcement yarns
- ReinfYoungs, reinfpoisson – Young’s modulus and Poisson’s ratio of the reinforcement yarns
- LubYoungs, lubpoisson – Young’s modulus and Poisson’s ratio of the lubricant yarns
- ResinYoungs, resinpoisson – Young’s modulus and Poisson’s ratio of the resin

No further user input is required within the script. The finite element model does however require further manipulation within the GUI to produce the output necessary for the friction model, described later in this chapter.

### 3.2.2 Abaqus General Commands

This section begins with a series of generic commands to load all Abaqus user interface sub-modules. This happens automatically when using the GUI, but has to be directly specified when using the scripting interface.

The script then creates an empty model space to work in. If the script is run repeatedly without creating a new file, for example while investigating the effect of varying different parameters, the previous model has to be deleted so that the new model can be built. This allows for the script to work whether the file space is empty or has previously been used.

The next section informs Abaqus that commands will refer to points in the “compressindex”



format. The default is to refer to commands using the “coordinate” format, which refers to a series of points using numbers, but does not allow points to be referred to as variables. The “compressindex” format allows the use of both numbers and variables to define points.

### 3.2.3 Create Design Area

Abaqus applies material specifications in a multi-material part using “sections” – these sections allow for a Young’s modulus and Poisson’s ratio to be specified, along with the possibility of using more complex properties, such as non-homogenous materials, though these are not used in the current model. The “Materials/Sections” part of the script creates the three materials used in the model.

The script then creates a single static analysis “step”. For a static model, such as the one considered, a step is a specified amount of time in which loads can be applied to a model, and the model allowed to stabilise. Multiple loads can be applied in a step, but these will all be applied simultaneously. To apply multiple loads successively, multiple steps are necessary. The current model is however a simple deformation/contact model with only one load, and therefore does not require multiple steps.

In the unit cell there are four threads in the warp direction and eight in the weft direction, with the spaces between them filled by resin. To create the FE model, a series of parts are made, each representing either one weft thread weaved between the two warp layers, or a

resin "spacer" which contains only the warp layers. By dividing the unit cell up into threads and resin spacing, these parts can be created separately then combined together into the overall unit cell at a later time, which simplifies the creation of the model.

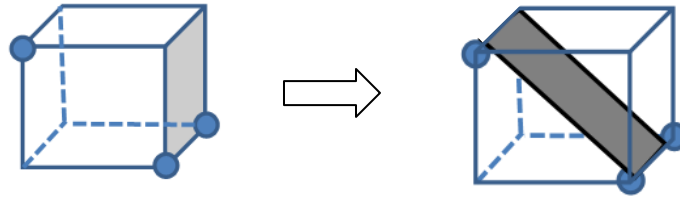
Each of the weft threads has the same undulating shape and the same length as it passes through the warp, however the start and end points are all slightly offset. Figure 3.1 (Figure 1.9) shows a cross-section through the warp of the fabric, with all threads shown on top, with only one thread shown on the bottom to highlight the weaving pattern. The pattern is that a weft thread passes over a reinforcement warp thread, between a reinforcement and PTFE warp thread, under a PTFE warp thread, then between a reinforcement and PTFE warp thread.



**Figure 3.1** Part of a cross-section through the warp showing only 1 weft thread

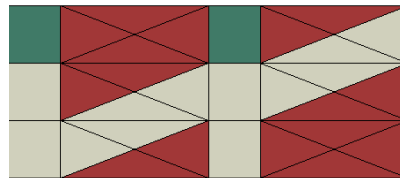
All threads have the same geometry, so instead of creating a new part for each weft thread, a single weft thread is created with the correct geometry, split into sections, and then re-assembled to create other weft threads which have offset geometries. A weft thread is created, which is then cut into two parts – one being the first quarter of the geometry, and the other being the following three quarters of the geometry. The first quarter is moved to the end of thread and then re-combined, to give the same thread pattern (offset) but with a new geometry.

To model the first thread, the script creates a series of points to define a block which has the height of the unit cell, with the length of one weft thread, and the width of the cross-section of the thread. This block is then divided into a series of sections, which will later receive material property definitions to create the complete thread pattern. The method of dividing a block in 3D is illustrated in Figure 3.2, which consists of cutting planes defined by three points. The coordinates of these points for a given division are calculated based on the user-defined geometry of the unit cell.



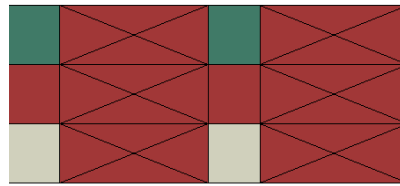
**Figure 3.2** Division of a 3D block (left) by three points, with the cutting plane shown (right)

Once the block has been split up into sections, these sections are each given an appropriate material assignment to create the weave structure. For larger areas of the same material, this is performed part-way through the process, so that should an area have the same material properties but need to be sub-divided further, there are fewer commands necessary. An example of a PTFE weft thread is shown in Figure 3.3.



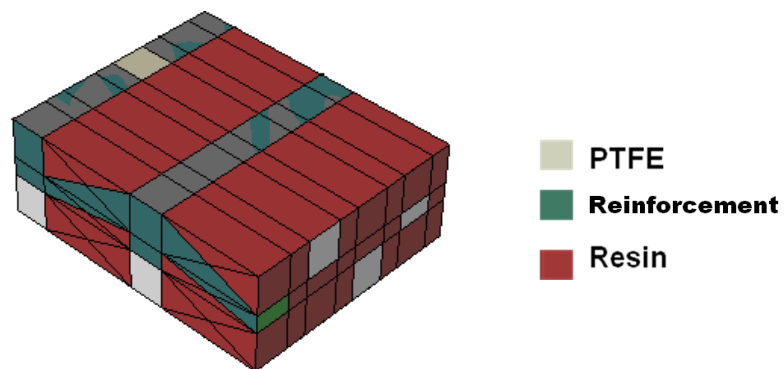
**Figure 3.3** A PTFE weft thread

In addition to the weft thread sections, a resin spacing section is also created. This has the height of the unit cell, the length of a weft thread and the thickness defined as the pitch minus the thread diameter from the user inputted variables. It contains areas which specify the warp threads, but the majority of the block is resin, as seen in Figure 3.4.

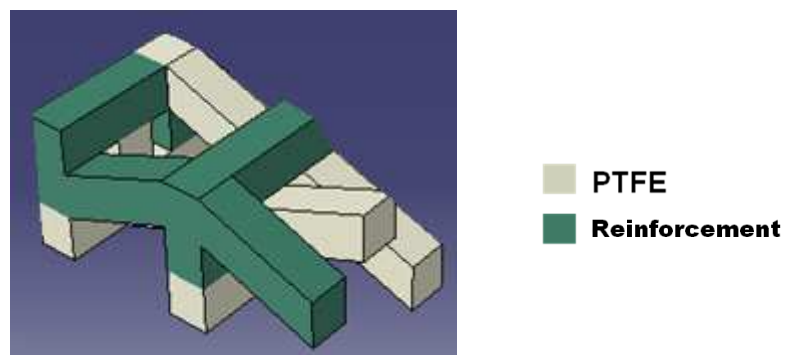


**Figure 3.4** Resin spacing section

Once all eight weft threads and the eight resin spacings have been created, they are placed into an assembly and then merged to create the unit block, shown in Figures 3.5 and 3.6. With the resin hidden in Figure 3.6, the pattern of the weft threads can be seen more clearly.



**Figure 3.5** Part of a “unit cell” of test composite fabric, made up of PTFE and reinforcement yarns in a resin matrix



**Figure 3.6** Part of a “unit cell” of test composite fabric, as Figure 3.5 but with resin hidden to show the weave structure

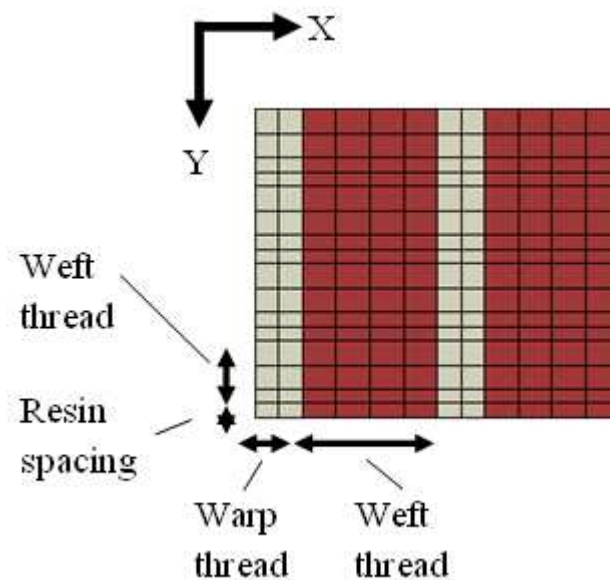
### 3.2.4 Model Assembly

DSS Abaqus allows surfaces to be referred to as “sets”, which are a collection of either element faces or nodes, but are specified based on geometry and are therefore mesh independent. Once a set has been created, any command that refers to that set will apply to all element faces or nodes contained within that geometry, though once a set has been created it can only refer to either element faces (referred to as “surfaces” in Abaqus) or nodes, as these specifications are not interchangeable. It is therefore recommended that for every geometry to be referenced, a set name is created for both element faces and nodes, as some commands refer only to element faces and some only to nodes.

In the Python script, sets are created for each side of the block (except for the top and bottom) in both element face and nodal form. These sets are used to set up the displacement and rotation constraints for the model, along with the harmonic boundary conditions. A set is not created for the bottom of the unit block, because this will change as material is removed from the bottom of the block to simulate wear, and therefore has to be manually created each time a specified amount of material is removed.

Two planar parts are created with the same dimensions as the top and bottom surfaces of the unit block. These are rigid parts, and are used to simulate compression of the model between two platens. These planes are given the boundary conditions discussed in the previous chapter. The sides of the unit block are given harmonic boundary constraints as discussed in the previous chapter.

Contact regions and the mesh must now be defined. Contact is not defined using the script as this has to be redefined every time material is removed from the unit block to simulate wear, and Abaqus CAE includes very simple commands for finding contact pairs based on geometry which are sufficient for this model. The model also has to be re-meshed for different levels of wear, and this is left for the user to perform. The mesh pattern at the bottom contact surface must have a regular structure for use in the friction model, discussed in the next chapter. This structure is shown in Figure 3.7. Each thread section is split in two in the  $y$ -direction, as is every resin spacing section. Each warp thread is split in two in the  $x$ -direction, and each weft thread section split into four in the  $y$ -direction.

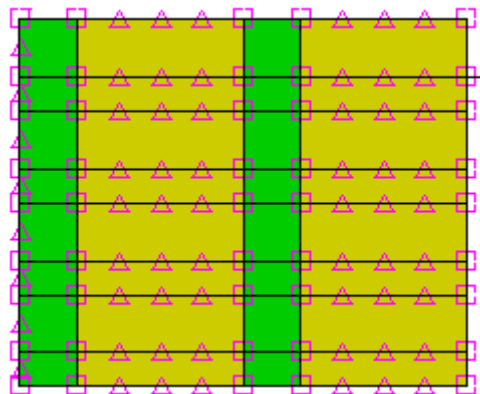


**Figure 3.7** Bottom side of unit cell with mesh pattern shown

### 3.3 Post-Python Tasks

As mentioned earlier, some tasks need to be performed manually after the Python script has been used to prepare the model for analysis. Firstly, material must be removed from the bottom of the unit cell if an amount of wear is to be simulated. This is done by creating a block with the same dimensions as the bottom surface of the unit cell, and with a height equal to the wear depth simulated. By placing this across the bottom of the unit cell, as shown in Figure 3.8, and subtracting its geometry from the overall geometry, the size of the unit cell is reduced. The bottom platen must then be relocated to the new position of the bottom surface, and the set for the bottom of the unit cell must be manually re-defined.

The mesh pattern must also be manually specified. This is done by placing nodes on the border of the unit cell, and allowing DSS Abaqus to build the mesh. Figure 3.9 shows the placement of nodes to create the mesh shown in Figure 3.7.



**Figure 3.8** Node placement on bottom surface of unit cell to specify mesh layout, node locations in pink

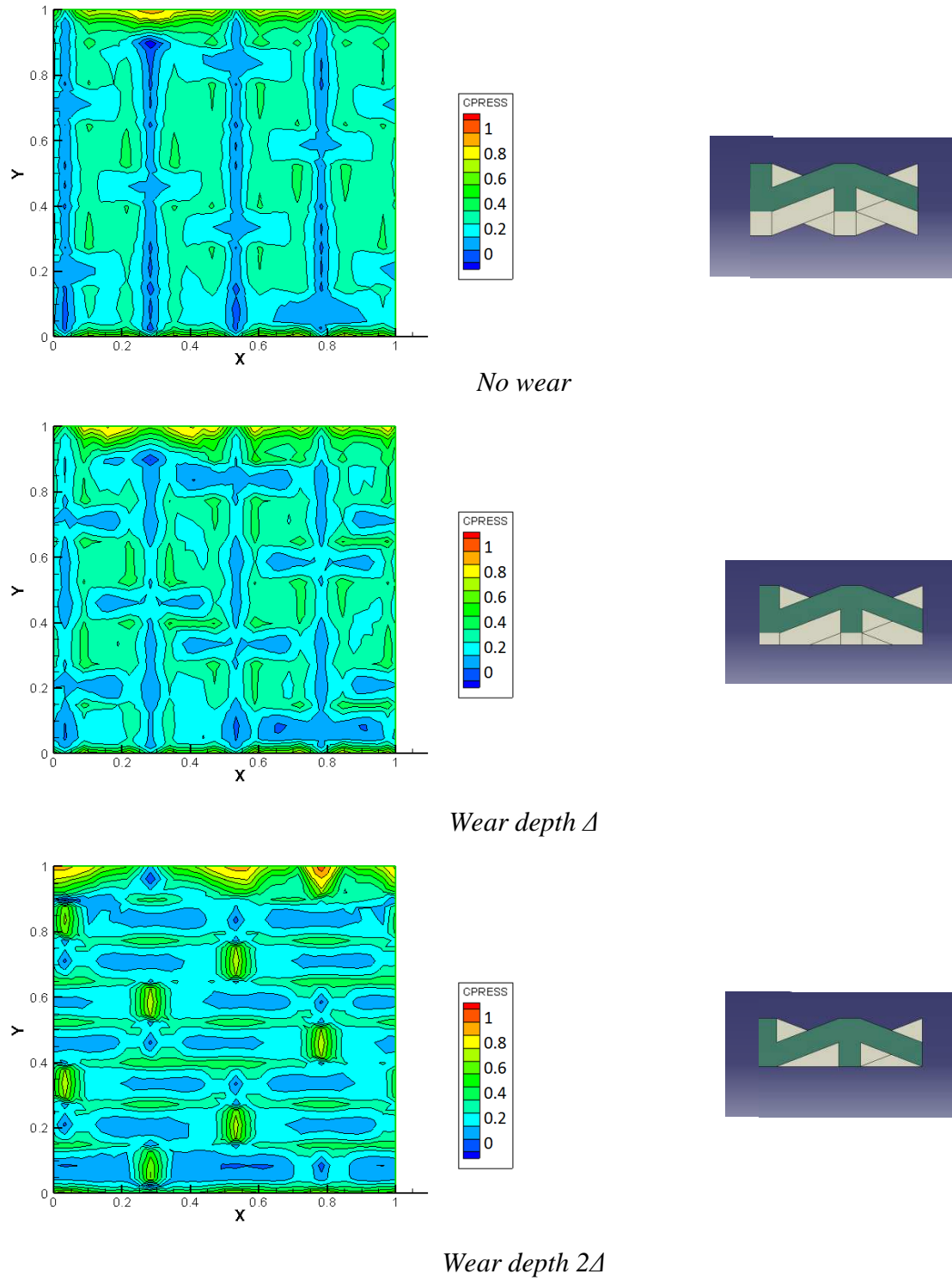


Finally, the analysis input file must be generated, then modified. DSS Abaqus allows most output types to be selected from the GUI, however the friction model requires the  $x$ -axis and  $z$ -axis coordinates of all nodes on the contact surface, along with the contact pressures at these points to be available as output information. The following lines must therefore be manually inserted at the end of the Abaqus analysis input text file, so that this information is outputted as part of the analysis.

```
*CONTACT PRINT, NSET=Bottom-side, FREQ=1
CPRESS
*NODE PRINT, NSET=Bottom-side, FREQ=1
COOR1, COOR3,
```

### 3.4 Results

When a constant pressure is applied across the top rigid plane in the model, contact pressures are generated on the bottom surface of the model. The pressure at any point is dependent on both the stiffness of the material in contact, and the material directly above the material in contact. Figure 3.9 shows the contact pressure contour at three different levels of wear, alongside a side view of the unit cell with the resin hidden showing the material removed from the bottom. The contact pressures are normalised with respect to the maximum contact pressure and are therefore independent of the force applied. High pressure regions are encountered where there is a high proportion of stiff reinforcement either in the contact or just away from the area in contact, with low pressure areas where there is a high proportion of soft PTFE either in or just away from the contact. Areas with a high proportion of resin in the contact tend to a normalised pressure of approximately 0.3. The long areas of low pressure in the  $y$ -direction seen when there is no wear correspond to the soft PTFE warp threads, however once a wear depth of  $2\Delta$  is achieved these strands have all been worn away and the surface threads are now predominantly oriented in the  $x$ -direction.

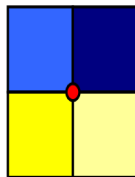


**Figure 3.9** Normalised contact pressure profiles shown for different amounts of wear, alongside side-view of unit cell with resin hidden

## 3.5 Technicalities of Python Script

### 3.5.1 Selecting Points

Selecting a section by coordinates is not an immediately obvious challenge. The most reliable way of doing so involves calculating the coordinates of the centre of the section and using this in a command to be applied to that section. Finding these coordinates however requires additional calculation, and therefore increases the complexity of the script. An alternative means of selecting a section is, if the coordinates of a point at the intersection between two sections are known, to use the coordinates of the point at the intersection plus a small increment to choose one of the sections. Figure 3.10 shows a datum point in red surrounded by four surfaces. If the coordinates of the point in red are  $(0, 0)$ , to select the top right section (dark blue) would require reference to a point  $(0 + s, 0 + s)$ , and to select the bottom right section (light yellow) the coordinates would be  $(0 + s, 0 - s)$ , where  $s$  is much smaller than the dimensions of any section.



**Figure 3.10** Datum point (red) surrounded by 4 surfaces (dark blue, light blue, yellow, light yellow)

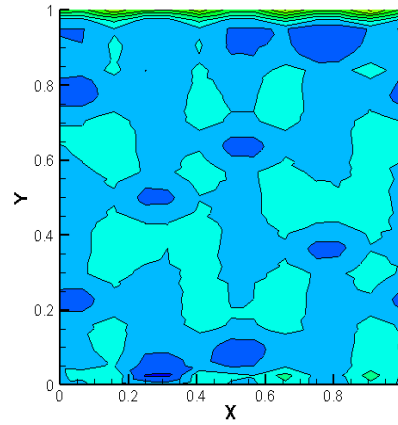
### 3.5.2 Mesh resolution

The time necessary to perform a finite element analysis of a model is dependent on the number of elements in the model, which for a given geometry depend upon the fineness of the mesh. In this model, a compromise had to be found between a mesh which was sufficiently fine as to produce a useful contact pressure contour, but with a realistic computation time.

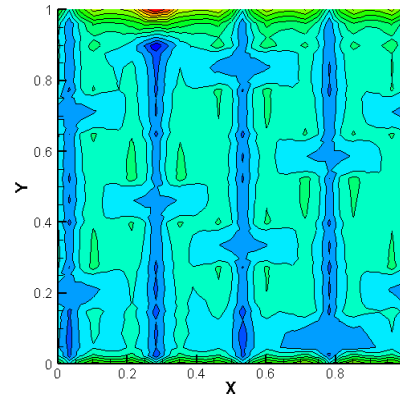
For a single variable, such as maximum displacement, a graph can be made of displacement versus mesh resolution, and therefore a mesh which is sufficiently fine that the results are independent of the mesh resolution can be found, and a finer mesh will not lead to a more accurate result. In the case of a contour however, increasing the resolution of the mesh will always increase the resolution of the contour on some scale, and as such the concept of a mesh-independent result is less applicable to contours.

Figure 3.11 shows the contact pressure contour on the bottom surface of the unit block without any material removed at three different mesh densities denoted as low, medium and high density. By moving from a low-density to medium-density mesh it can be seen that more detailed information is gained on the location of contact pressure peaks and valleys. In the case of the high-density mesh information is not gained on the location of these peaks and valleys, it is the definition of the boundaries between these areas that is increased. The low mesh density allows the model to be analysed in less than ten minutes on the computer used for these simulations, and the medium mesh density allows the model to be analysed in one

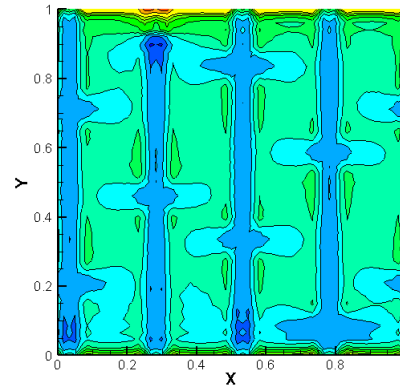
hour. The high mesh density model can take over four hours to analyse, and the trade-off between increased resolution and increased processing time was not seen to be favourable. The medium-density mesh was therefore adopted for generation of contact pressure contours used in the friction model. Computation times are obviously dependent on hardware specifications and additionally, since the development of this model, there have been considerable improvements in the analysis speed of DSS Abaqus. As such, there is the potential for future models to be meshed at much finer resolutions without necessarily increasing the analysis time unduly.



*Low mesh density (8000 Elements for unit cell model)*



*Medium mesh density (19000 Elements for unit cell model)*

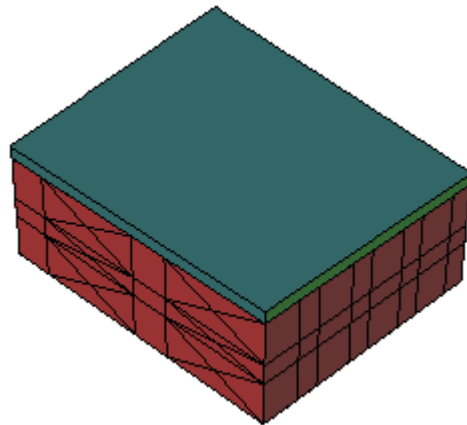


*High mesh density (50000 Elements for unit cell model)*

**Figure 3.11** Normalised contact pressure contour of bottom surface of unit cell meshed at different mesh resolutions (left) and contact surface mesh (right)

### 3.5.3 Omission of Reinforcement Layer

The test liner also has a further reinforcement backing layer. This has not been considered in the analysis presented. In order to show that omission of the reinforcement layer in the finite element model did not have any significant impact on results, a model was created which included this layer, with all the same boundary conditions as the previously described model of the test fabric alone. The thickness of this layer in the finished liner was obtained from tomography. Figure 3.12 shows the finite element model assembly, with the test fabric in red and the reinforcement layer in green.



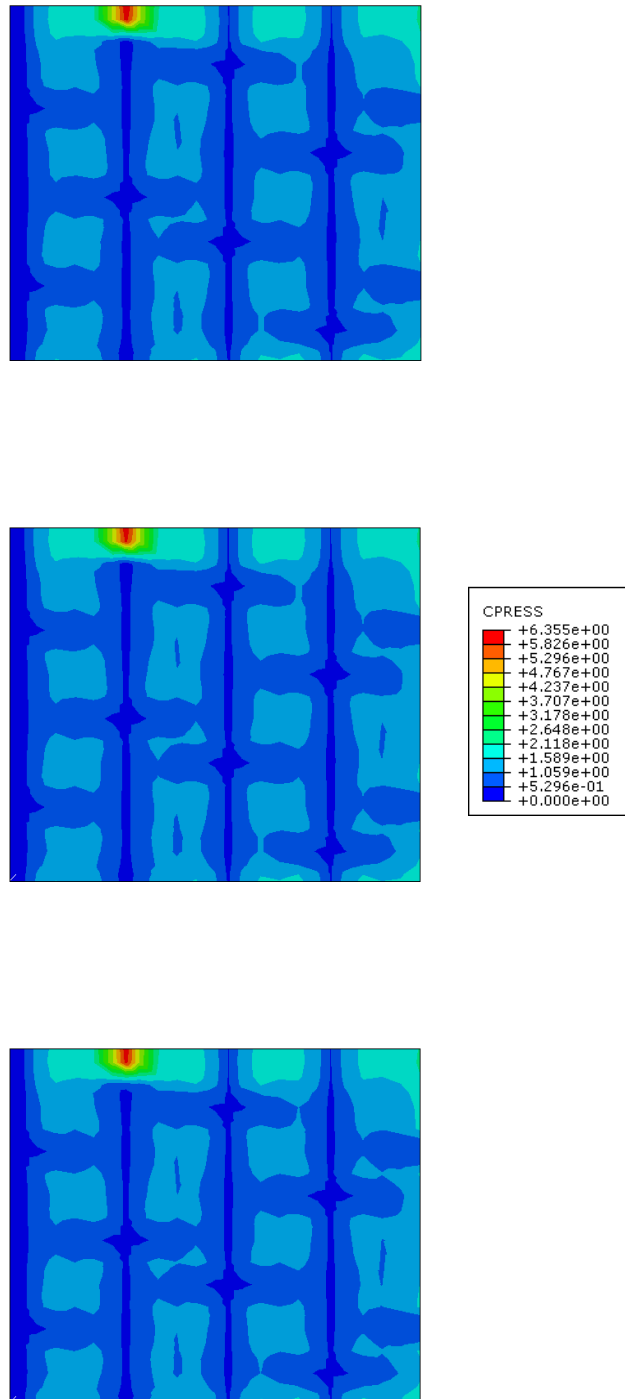
**Figure 3.12** Finite element model of test fabric and reinforcement layer, with the test fabric in red and the reinforcement layer in green

The reinforcement liner stiffness was given two values representing the lowest and highest possible values. Three cases were compared; the test liner alone (case 0), the test liner with a low stiffness reinforcement layer (case 1), and the test liner with a high stiffness reinforcement layer (case 2)

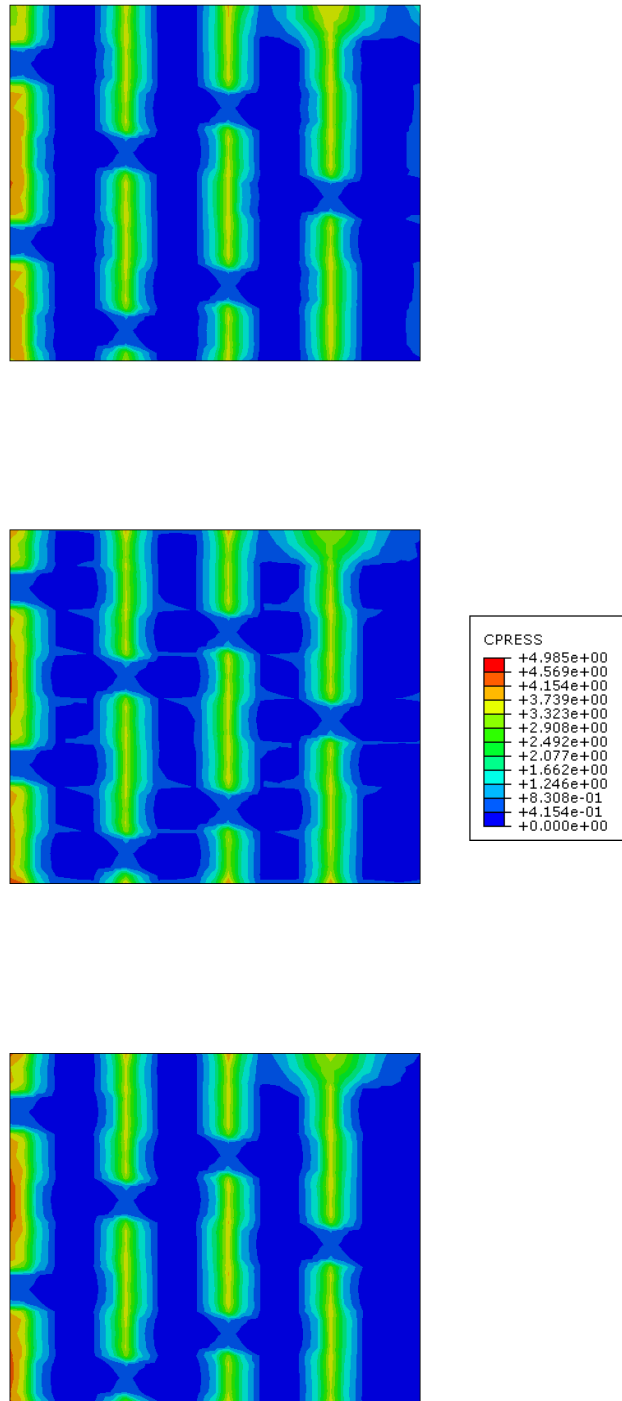


To assess the effect of the inclusion of the reinforcement layer, the contact pressure contours for the three cases were compared. Figures 3.13 and 3.14 show the results of these simulations. In the case of these figures the differences in the results are extremely minor, and can only be revealed either by very close inspection of the contact pressure contours or examination of the raw data. For the higher wear depth presented in Figure 3.14, the differences are more apparent, but in all cases there is less than a 10% variation in the contact pressure values.

The inclusion of the reinforcement layer in the model increases the processing time of one analysis by between 4× and 10×, as the interface between the reinforcement layer and the test fabric considerably increases the complexity of the calculation. When the Case 1 and 2 contact pressure contours were used in the friction model, the difference in the overall coefficient of friction obtained was less than 5%, meaning that omission of the reinforcement layer was a reasonable assumption, given the consequent improvement in processing speed.



**Figure 3.13** Comparison of contact pressure contours at zero wear for Case 0 (top), Case 1 (middle) and Case 2 (bottom)



**Figure 3.14** Comparison of contact pressure contours at a high wear depth for Case 0 (top), Case 1 (middle) and Case 2 (bottom)



## **4. Friction Model**

### **4.1 Concept Overview**

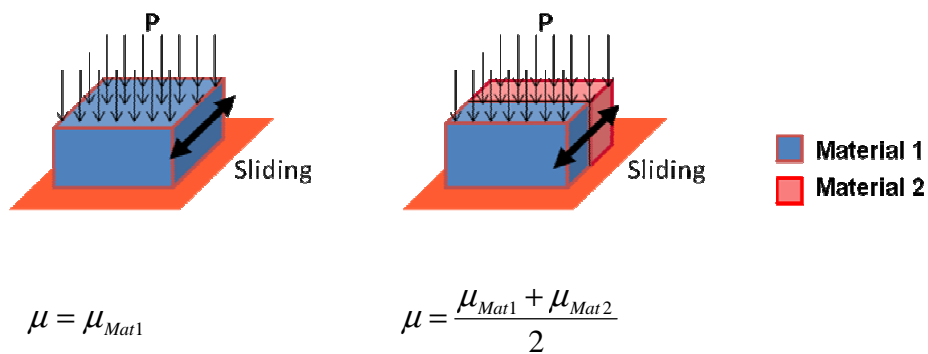
The central concept investigated using the friction model is that the overall coefficient of friction of the composite liner is dependent upon the coefficients of friction of the different materials in contact. It is further hypothesised that this overall coefficient of friction is dependent upon the proportions of each material at the contact interface, and also upon the way in which the contact pressure is distributed.

The model uses the previously discussed Finite Element (FE) analysis to obtain stiffness information at varying wear states, which is then used to predict an overall friction coefficient at defined states of wear.

The research is concerned with the test bearing liner, but the wear simulation model is designed so that its application to liners with different combinations of materials is straightforward. This will enable it to be used as a tool in material development – to minimise both the time and resources necessary to develop future alternative bearing liner materials.

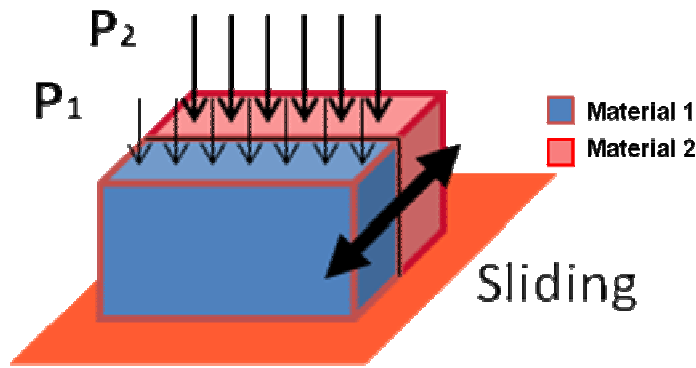
## 4.2 Tribology Assumptions

In the case of a single material in sliding contact with a counterface as shown in Figure 4.1(left), the coefficient of friction will be that of the material/counterface pair. We may then consider a simple case of a block consisting of two different materials of the same size but having unequal friction coefficients as shown in Figure 4.1(right). If it is assumed that the interface contact pressure acting over the surfaces of the two blocks is uniform then the overall coefficient of friction will simply be the mean of the two values for the two separate materials, as shown. If the blocks are unequal in size (the contact pressure remaining uniform) then the net friction coefficient will be weighted in proportion to the two areas in contact. However, when the two materials are of significantly different elastic properties (as is the case in a composite bearing liner) the assumption of a uniform contact pressure at the interface does not hold (even if the pressure applied at the top of the composite block is uniform) because of the different stiffness behaviour of the two materials.



**Figure 4.1** Coefficient of friction for single- and multi-material interfaces (left) single block; (right) two blocks of equal size.

Assuming that in the simple case of the 50/50 area split, one half is subjected to a very high contact pressure, and the other half is subjected to little or no contact pressure, then the overall coefficient of friction will tend towards that of the material with the highest contact pressure. Figure 4.2, for example, shows a two-material block in sliding, with different pressures applied to each section. Assuming that these pressures are transmitted directly to the contact, and they are not re-distributed at the interface between the two materials, then the net coefficient of friction will be given by Equation 4.1



**Figure 4.2** A two-material block with different contact pressures on the two materials.

$$\tilde{\mu} = \frac{F_{friction}}{W} = \frac{\mu_1 A_1 p_1 + \mu_2 A_2 p_2}{A_1 p_1 + A_2 p_2} \quad (4.1)$$

In the case of an n-material contact (such as the composite liner which consists of three distinct materials) we make the fundamental assumption that the overall friction coefficient is based on the area in contact of each material, and the contact pressures of those areas as

follows:

$$\tilde{\mu} = \frac{\mu_1 A_1 p_1 + \mu_2 A_2 p_2 \dots + \mu_n A_n p_n}{A_1 p_1 + A_2 p_2 \dots + A_n p_n} \quad (4.2)$$

Finally, we must take account of the fact that in the composite liner considered the contact pressure between each individual constituent material and the counterface will, in general, vary from point to point (as revealed by the FE model) according to the geometry of the textile weave and the proportions of different materials in the composite.

### 4.3 Principles

The simulation of friction and wear at the liner/counterface is based on the FE model. Values are assumed for the elastic properties of the constituent materials together with their friction coefficients when in contact with the steel interface. An overall coefficient of friction is calculated for the liner/counterface pair at a range of wear depths, weighted according to the proportions of each material in contact and contact pressures of the regions in contact as outlined above.

The contact force at each node of the friction model is calculated by multiplying the contact pressure at the node by its associated area. The frictional force at each node is then given by the product of the force at that node and its associated coefficient of friction. The sum of these frictional forces, divided by the area in contact, gives the effective coefficient of friction for the contact interface,  $\tilde{\mu}$ , shown in Equation 4.3

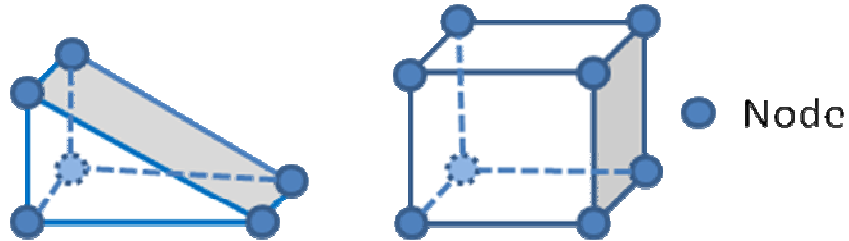


$$F_{contact,node} = p_{node} \times area_{node}$$

$$F_{node} = F_{contact,node} \times \mu_{node}$$

$$\tilde{\mu} = \frac{\sum F_{node}}{\sum area_{node}} \quad (4.3)$$

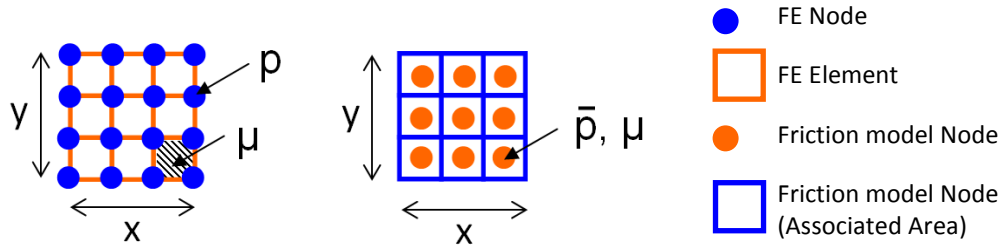
It is important at this point to distinguish between two concepts – FE nodes and friction model nodes. FE analysis makes use of elements, which in the case of the model developed are either six-node or eight-node wedge and brick elements, respectively, with faces made up of three or four nodes, as illustrated in Figure 4.3.



**Figure 4.3** Node distribution on Wedge (left) and Brick (right) elements

Friction model nodes represent an area, specifically a rectangular contact face comprising of a single material. Friction model nodes exist at the centre of the contact face of each FE element, and have both an associated area and a contact pressure, as illustrated in Figure 4.4. In an FE model, pressures ( $p$ ) are applied at nodes, and friction coefficients ( $\mu$ ) are associated with element faces. In the friction model, friction coefficients are applied over an area, and

have an associated average pressure across the element area,  $\bar{p}$ .



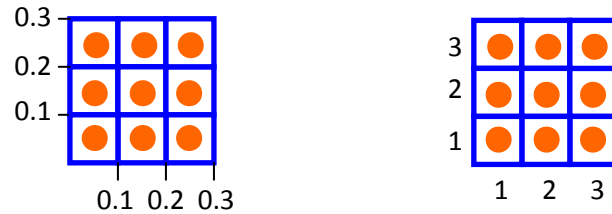
**Figure 4.4** FE (left) and friction model (right) meshes of a given area

## 4.4 Abaqus Output Files

DSS Abaqus by default delivers results in a database file (.odb) which can be used to visualise results through the Abaqus results visualisation module. Data can also be requested for certain results in a tabular format, and this is done by adding this request to the Abaqus processor input file. To request the data for a specific area, in this case the contact area, the area of interest is manually selected in the user interface and given a name, so that it can then be called in the input file.

The data required in this case are the coordinates of each FE node in contact, and the contact pressure associated with each node. Forces are calculated in the FE model at nodes, irrespective of whether a node-based or element-based contact formulation is used, and contact pressures are obtained by dividing the force at the node by its associated area to determine the nodal pressure. These data are then manually manipulated into a structure

ready for use in the friction model, stored as a .csv file. Data are referred to by point number. The point number is a method of referring to nodes without including the coordinates of the point. Figure 4.5 shows an example of this numbering scheme. In this example the bottom right node would have the coordinates (0.25, 0.05) and the point number (3,1).



**Figure 4.5** Friction model mesh with dimensions (left) and node numbering scheme (right)

These files all have the same structure – the first three lines define the wear depth step and the number of points in the  $x$  and  $y$  directions. The “wear step” is the notation used to define an amount of wear, and is described in the next section. Each subsequent row is then made up of five data items – the point number in  $x$  and then  $y$ , the  $x$  then  $y$  coordinate, and finally the contact pressure at that node (in pascals). The final line is always five 0’s, to inform the friction model code that it is the end of the file. Table 4.1 shows an illustration of this format, along with an actual example in Table 4.2.

**Table 4.1** Layout of .csv file containing contact pressure data

Layer no.				
No. Points (x)				
No. Points (y)				
Point no. (x)	Point no. (y)	X coordinate	Y coordinate	Contact Pressure
Point no. (x)	Point no. (y)	X coordinate	Y coordinate	Contact Pressure
Point no. (x)	Point no. (y)	X coordinate	Y coordinate	Contact Pressure
Point no. (x)	Point no. (y)	X coordinate	Y coordinate	Contact Pressure
...	...	...	...	...
...	...	...	...	...
0	0	0	0	0

**Table 4.2** Example of .csv file containing contact pressure data

2				
25				
33				
1	33	0.3846	-1.17	0.2612
2	33	0.4346	-1.17	0.4569
3	33	0.4846	-1.17	1.48
4	33	0.5558	-1.17	1.732
...	...	...	...	...
...	...	...	...	...
0	0	0	0	0

The layer number in Table 4.1 is not read by the friction model code, and is there to allow the user to see which wear depth a .csv file corresponds to without knowing its file name. The number of points in the  $x$  and  $y$  dimensions are used to specify the size of the array that the contact pressures will be read into. Currently the arrays are the same size for each wear step, however this feature gives the potential for different mesh sizes to be used at different wear steps.

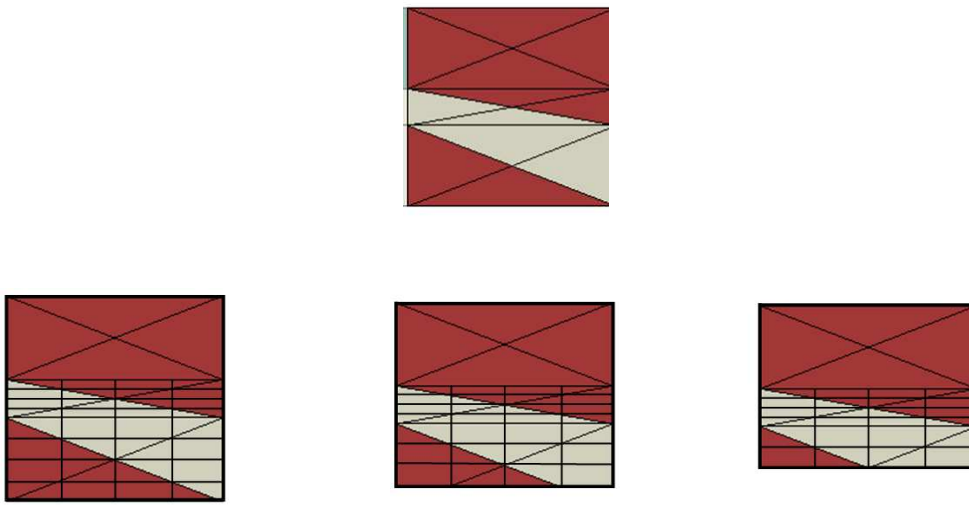
As seen above, the first three lines of each file contain data both for the user's information and to define the size of the arrays needed. These data are only read into the friction model for the first wear step (all wear steps have identical meshes in the contact region); for all other input files this code indicates to the friction model where to begin loading contact pressure values into the .csv file.

## 4.5 Wear Steps

The friction model calculates overall friction coefficients corresponding to discrete amounts of wear of the liner material, split into a series of wear “steps”  $\Delta$ , where  $8 \Delta$  is the maximum wear depth considered for normal use. The reasons for choosing these particular wear amounts are to maintain the same mesh pattern at the contact interface while removing discrete amounts of material from the model.

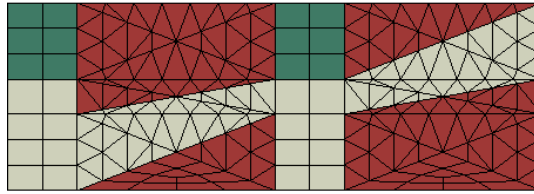
The numerical procedure for simulation of wear effectively removes layer after layer from the original surface of the composite liner thereby revealing different strata of the textile weave. As each “wear step” progresses through the weave it therefore exposes surfaces with different mixtures of the three components (reinforcement, PTFE, resin). This affects not only the area-fraction occupied by each component, but also the way in which pressure is distributed on the surface due to changes in the local stiffness behaviour of the liner when loaded in the FE model.

The wear simulation process, involving reductions in the volume of the model clearly has implications for the FE element structure. If we consider a section of one of the PTFE yarns in the warp/weft direction, for example, due to the pattern of the cell division it is possible to remove discrete amounts of material while maintaining the mesh pattern. Figure 4.6 shows a section of a weft thread with example mesh patterns at three different levels of wear. It can be seen that in all cases there are four element faces on the bottom edge of the unit cell.



**Figure 4.6** Single weft thread (top) with mesh pattern of the highlighted section shown at 3 different levels of material removal (bottom)

The figure shows that by using cuboid and wedge shaped elements, the same number of elements in contact can be maintained despite the changed geometry. In the above example the mesh is too coarse and would lead to mesh-dependent results, however these areas can be broken down into smaller meshes to obtain a mesh-independent result while maintaining the same number of elements in contact, as illustrated in Figure 4.7

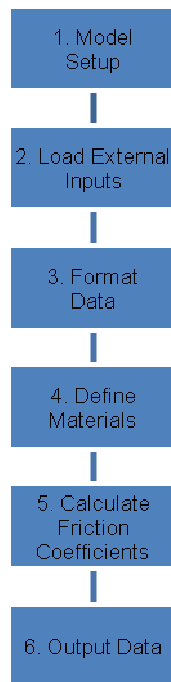


**Figure 4.7** Actual mesh of section seen in Figure 4.6

## 4.6 Model Structure

The friction model utilises the contact pressure data generated by the FE model, along with definitions of the materials in contact, and calculates an overall friction coefficient for the material at different levels of wear based on the proportions of each material in contact and the contact pressure variation. The model comprises of six parts, which are discussed in detail in the following sections of the chapter. Figure 4.8 shows a flowchart which illustrates the sequence in which these parts are handled..





**Figure 4.8** Friction model flowchart

#### 4.6.1 Model Setup

This section sets up the variables used in the friction model, be they integers, real (decimal), numbers or arrays, etc.

The friction model code begins by naming the executable file that will be created. It then defines all variables used, be they numbers or arrays. For example, “sx1” and “sy1” are the dimensions of the friction model node arrays in  $x$  and  $y$ , and are defined as integers, as these will later be read in from the Abaqus output files.

The friction model defines one- and two-dimensional arrays, their size not being set at this stage, as this is dependent on the data read in from the Abaqus output files. The one dimensional arrays (sx, sy, sxa, sya) are used to calculate the size of the associated area for each friction model node. The remaining arrays are used to define different information for each wear step, with  $n$  denoting the integer value of the wear depth:

- Area of each friction model node (“area”)
- Young’s modulus at each friction model node (“youngs”)
- Contact pressure at each FE node (“cpresn”)
- Contact pressure at each friction model node (“cpreseln”)
- Friction coefficient at each friction model node (“coefn”)
- Force due to contact pressure at each friction model node (“forceeln”)
- Force due to friction at each friction model node (“fricforcen”)
- Force due to friction at each friction model node, assuming a non-varying contact pressure distribution (“testfricmatn”)

#### 4.6.2 Load External Inputs

The contact pressure distribution generated by the FE analysis must be prepared to be read in from .csv files. These data must first be extracted from the FE results and processed into a format appropriate to the friction model, as described in a previous section.

The blank, undimensioned arrays are then given their dimensions, in terms of the data read in from the beginning of the Abaqus output files, in terms of “sxl” and “syl”. These are the

number of nodes in the  $x$ - and  $y$ -directions, and therefore “ $sxl-1$ ” and “ $syl-1$ ” are the number of friction model nodes in the  $x$ - and  $y$ -directions.

The data from the Abaqus output files are now read into the model. The contact pressures are read into a contact pressure array for the current wear step, and, in the case of the first wear step, the  $x$ - and  $y$ -coordinates of each FE node are also read, though this is necessary for subsequent steps.

#### 4.6.3 Format Data

By reading in the coordinates of all FE nodes, the size of the rectangle associated with the friction model nodes can be calculated by finding the difference between the  $x$ - and  $y$ -coordinate of each FE node and its neighbour. This is performed once for all wear steps, due to their identical mesh patterns. Once the two arrays of  $x$  and  $y$  vertex lengths have been calculated, they are multiplied together to give an array of the areas associated with each friction model node. These values depend on the resolution of the coordinates tabulated by the FE model, but the difference between the sum of all friction model node areas and the actual total contact area is always less than 0.12%, therefore this is not seen as a source of significant error.

As discussed earlier, in this model there will always be one more node in any axis direction in the FE model than there will be in the friction model. Thus the size of any array of FE nodes

has to be reduced by 1 in all dimensions to match it to the size of a friction model node array. The matrix reduction is performed by taking an average of the four FE nodes which surround the friction model node. This process reduces the resolution of the data, however a check is included to compare the total contact pressure before and after the downsizing process, and in all wear steps the difference between the total contact pressure before and after was less than 1%.

#### 4.6.4 Define Materials

An array is also created for each individual wear step of the same dimensions, but containing the coefficient of friction for each friction model node based on the material in contact at that node. As no suitable method of transferring this information between the FE model and the friction model code was identified, this array was built manually. The Abaqus graphical interface is used to view materials definitions at elements, and this is transferred to the Friction model code by specifying the material at each friction model node in the array.

#### 4.6.5 Calculate Friction Coefficients

Once all the necessary arrays have been generated and filled, they are multiplied together as according to Equation 4.3.

$$\tilde{\mu} = \frac{\sum F_{node}}{\sum area_{node}} \quad (4.3)$$

Two other “check” values are also calculated – the total tangential force at each wear step, and an average area-weighted coefficient of friction for the material based on the areas in contact and their coefficients of friction, but not the contact pressures, as seen in Equation 4.4.

$$TotalForce = \sum F_{node}$$

$$Avg\mu = \frac{\sum (\mu_{node} \times area_{node})}{\sum area_{node}} \quad (4.4)$$

A deviation in the total force would indicate that either not all contact pressures have been read in correctly in that step, or there is a problem in the array reduction between FE contact pressures and friction model contact pressures. The average coefficient of friction acts as a benchmark for the overall coefficient of friction, and significant deviation between these values could indicate a miscalculation within the friction model code and can be used to prompt a checking investigation.

The values for the coefficient of friction for each wear step, with and without inclusion of the contact pressure weighting, are then displayed to the user. These will vary based on the coefficients of friction specified for each material in the contact, so careful consideration of the values used is necessary

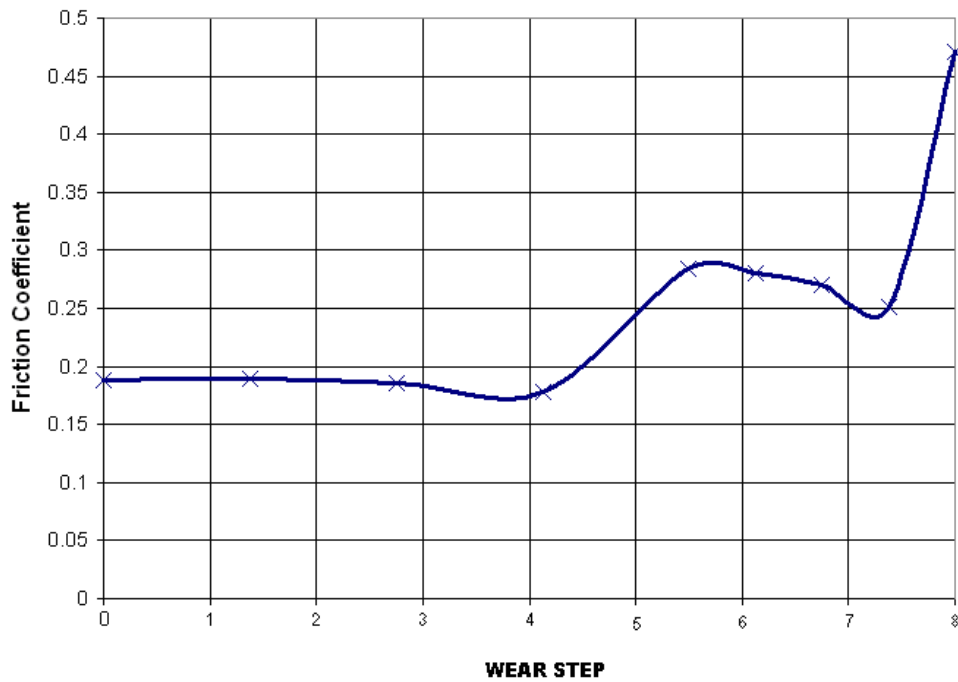
## 4.7 Results

In order to produce a friction coefficient for a given wear step, coefficients of friction must be defined for the three materials in contact. As the future application of the model was seen as being for analysis of pre-prototype liner materials, deriving these values from bespoke tests was not seen as appropriate. Instead values were taken from a commonly available source for the stiffness and coefficients of friction of these three materials. Table 4.3 shows the values assumed for the friction coefficient of each material.

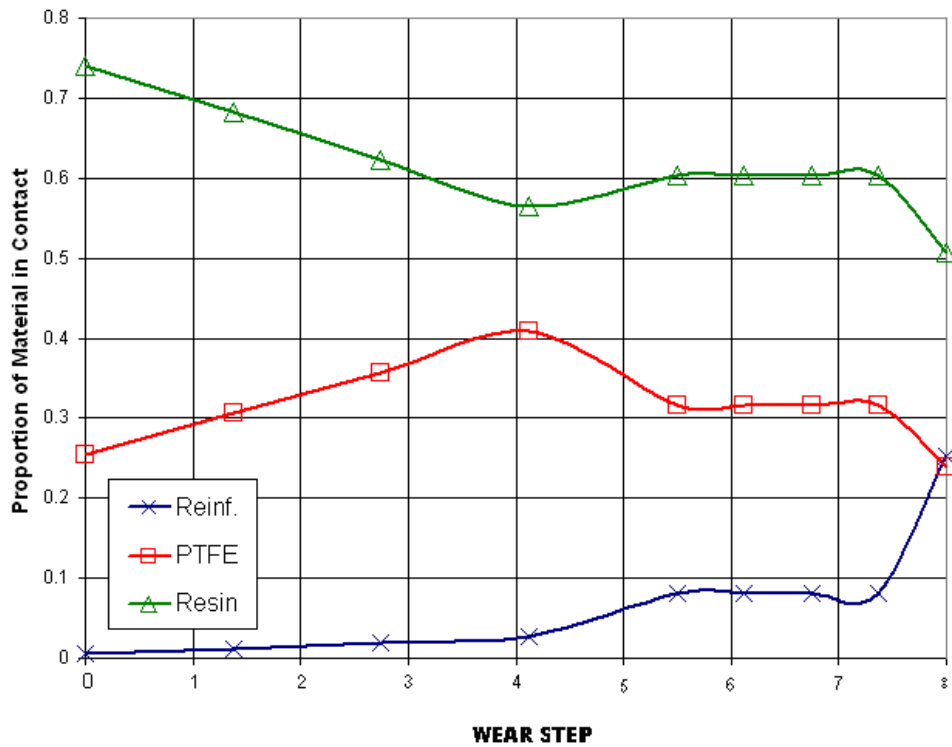
**Table 4.3** Friction coefficients of materials used in friction model (Engineering Toolbox, 2013)

	<b>Friction Coefficient</b>
<b>PTFE</b>	0.04
<b>Reinf.</b>	0.2
<b>Resin</b>	0.6

Figure 4.9 shows the variation in friction coefficient versus wear depth generated by the friction model. There is an almost constant coefficient of friction of 0.18 until a wear depth of  $4\Delta$ , at which stage the coefficient of friction increases significantly. This increase in the coefficient of friction is attributed to the increase in the proportion of reinforcement in the contact region. Figure 4.10 shows the variation in the proportion of each material in contact. It can be seen that after a wear depth of  $8\Delta$ , the proportion of reinforcement in the contact region increases sharply.



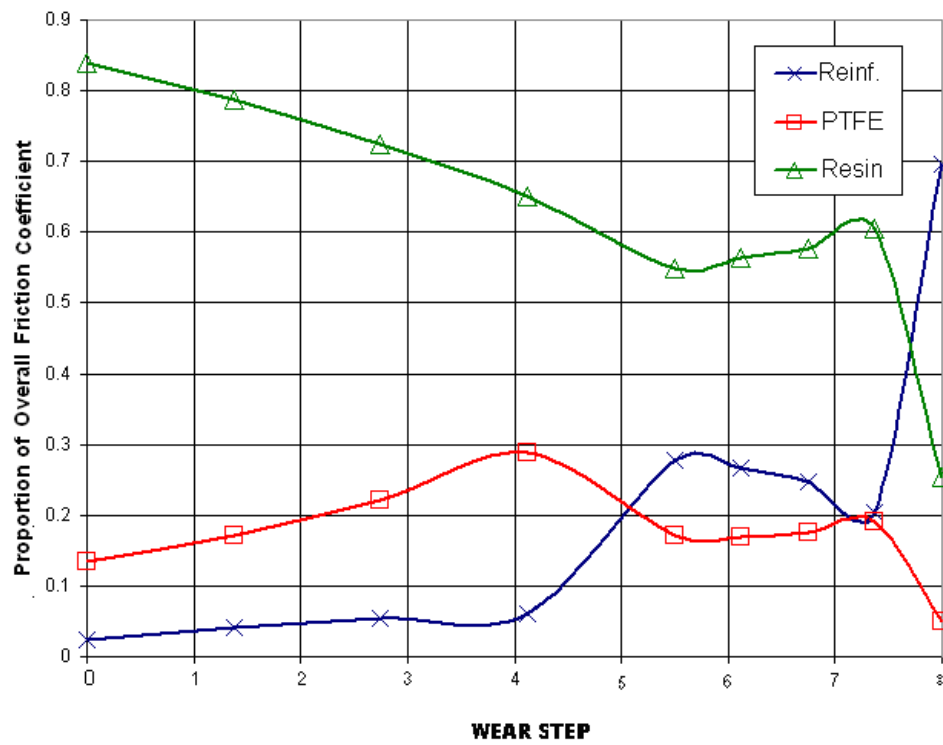
**Figure 4.9** Variation of friction coefficient with depth of wear predicted by the friction model



**Figure 4.10** Proportions of materials in contact at varying wear depths predicted by the friction model

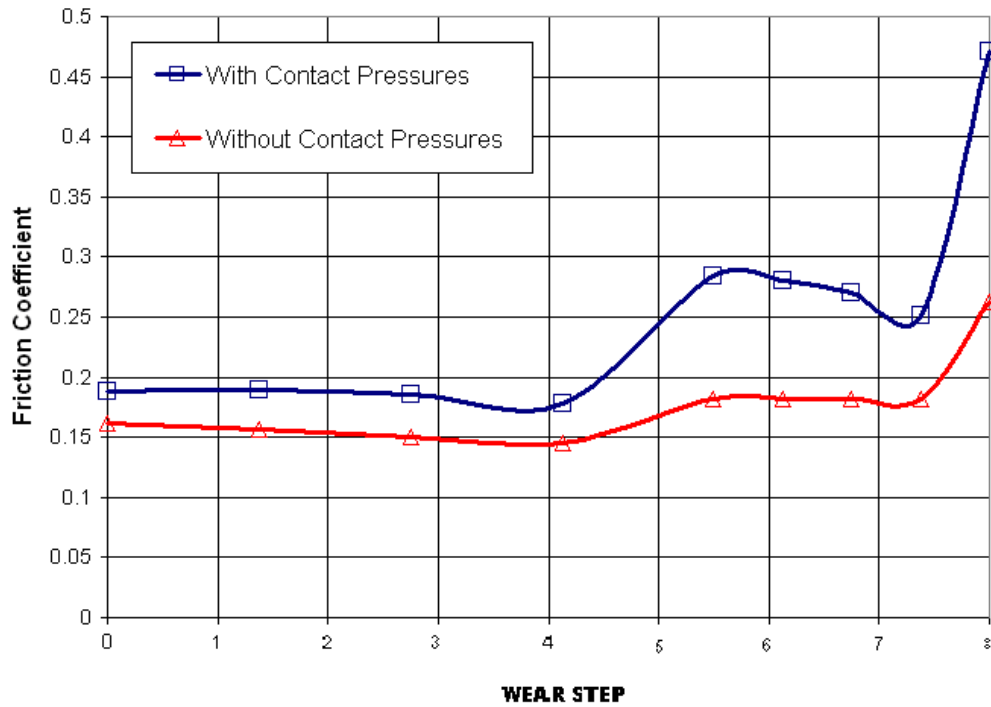
The sensitivity of the results to the assumed coefficients of friction for each material was also assessed by simulating each material successively with a friction coefficient of 1.0 and the other two materials with coefficients of zero. Figure 4.11 shows the results of this analysis, and demonstrates that the model is most highly sensitive to the coefficient of friction applied to the resin, except in the case of a wear depth of  $8\Delta$  when it is most sensitive to the coefficient of friction of the reinforcement.





**Figure 4.11** Results of sensitivity analysis of friction model

Figure 4.12 shows a comparison between the results obtained from the friction model with and without taking account of the contact pressure variation across the interface. The values without the contact pressure variation are easier to generate, as they only require knowledge of the proportions of materials in the contact area at different wear depths.



**Figure 4.12** Results of friction model with and without contact pressure bias

## 4.8 Limitations

The friction model was originally meant to use contact pressure data from the FEA model at element integration points (in this case the centre of the element), as this would match the number of points with the size of the friction model mesh. A difficulty was found, however, in obtaining the dimensions of the elements when the data were requested in this manner, which meant the area of each element could not be used in the friction model. As a result the information about contact pressures is read in at nodes, and the averaging process discussed earlier is used to obtain the effective pressure acting on each element.

The friction model was originally intended to be highly flexible with regard to the number of

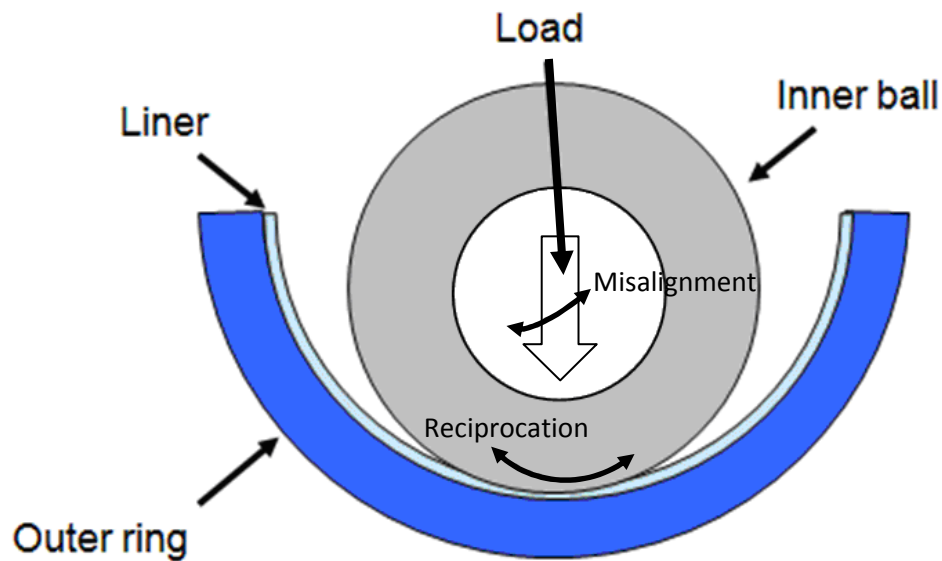
wear steps used and mesh density of the FE/friction model models at each of these steps. The final code is built on this principle, However, no reliable method for obtaining data about the material assignment at the Abaqus elements in contact could be found which was available in a useful format. The array defining the coefficient of friction of each friction model node (based on the material it is associated with) is a key part of the model, and due to this limitation it has to be created manually. This means that each extra wear step has to have this array manually defined, and it also has to be redefined following any changes in mesh density for existing wear steps.



## 6. Wear Model

### 6.1 Theory

The wear taking place in composite spherical plain bearings is in general a much simpler process than the complex wear mechanisms found in lubricated rolling-element bearings. In principle, the area of the bearing liner subjected to both load and sliding will wear away, gradually increasing the conformity of the liner and the inner ball, thus distributing the load over a wider contact patch. Figure 6.1 shows the constituent parts of a spherical plain bearing, with the non-conformity between the inner ball and the outer ring exaggerated for clarity. The three components considered are the inner ball, which will fit onto the reciprocating part of the application via a shaft, the outer race, which will fit into a housing in the non-moving part of the application, and a composite self-lubricating liner which resides between the two. This is a typical arrangement, and other configurations where both the inner ball and the outer ring are in motion can be reduced to this case by simply considering the relative motion of the components. The bearing is subjected to a load, and the inner ring reciprocates with an oscillation measured in degrees about the centre of the inner ball, and with a frequency in Hz. Rotation about the axis normal to the axis of load application and the axis of reciprocation is also possible. This is referred to as misalignment, and is a result of misalignment between components in the overall assembly.



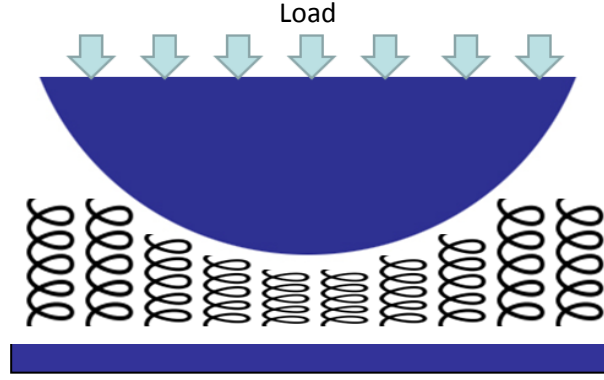
**Figure 6.1** Schematic arrangement of spherical plain bearing with exaggerated non-conformity between inner ball (grey) and outer ring (dark blue), also showing the composite liner (light blue) and the load and reciprocation that the bearing is subjected to

The lifespan of a bearing is measured by the number of operating cycles under load until the bearing is no longer suitable for the application. In the case of rolling element bearings, the end of a bearing's life is usually characterised by catastrophic failure, resulting in significantly increased friction and often a structural failure of the overall bearing. In most applications of spherical plain self-lubricating bearings, the bearing becomes unsuitable once the clearance or “backlash” has reached a pre-determined limit. Backlash in this example is the maximum radial internal clearance, defined as “The total free play between the ball and the outer ring when measured in the radial direction, i.e., normal to the centreline of the bearing bore.” (SAE, 2007)

A means of modelling the progression of backlash over the life of the bearing is sought both

for estimating the lifespan of a bearing in a given application, and predicting the effect of changes in bearing geometry or operating conditions. In practice it is found that the majority of wear takes place on the liner due to loss of material. Some wear is seen on the inner ball, but this is invariably much less than that which takes place on the liner, and usually amounts to a marginal change in surface roughness rather than a change in form. The inner ball and outer race are manufactured from steel and these components are an order of magnitude stiffer than the liner material in practice. In formulating a simple wear model therefore, the liner may be treated as the deformable, wearable component sandwiched between rigid, non-wearing parts.

In the wear model considered here, contact between the liner and inner ball is calculated based on the liner's elastic stiffness. Elastic deformation of the loaded liner is assumed to behave according to a simple bedspring model (Johnson 1987) as illustrated in Figure 6.2. The figure shows “springs” (initially all of the same length in this case) supporting the load applied between a rigid curved body and a rigid flat. The springs are deflected to conform to the shape of the rigid body, so that for a given translation of the rigid body, there will be a variation in the deflection of the springs.



**Figure 6.2** 2D bedspring model of a rigid circular object (blue) under load supported by a flat body represented by a series of springs, with the variation in deflection of the springs visible

In general all springs in a bedspring model have an associated length and stiffness, which means that a given strain of a spring ( $\varepsilon = \frac{\Delta L}{L}$ ) will give a stress due to contact, herein

referred to as a contact pressure ( $\sigma_{contact} = \frac{E\Delta L}{L}$ ). This contact pressure will be dependent on the length ( $L$ ) and stiffness ( $E$ ) of the spring considered. By considering the equations for stiffness and strain,  $E = \frac{\sigma}{\varepsilon}$  and  $\varepsilon = \frac{\Delta L}{L}$ ,

$$\sigma_{contact} = \frac{E\Delta L}{L} \quad (6.1)$$

The product of the contact pressure of a spring and its associated area ( $A$ ) gives the load carried by that spring. For a flat bedspring model, the sum of the load carried by all springs gives the total load carried.

$$W_{total} = \sum_{all\ springs} \frac{EA\Delta L}{L} \quad (6.2)$$

The area and length of a spring is dependent on the geometry of the model, and its stiffness is

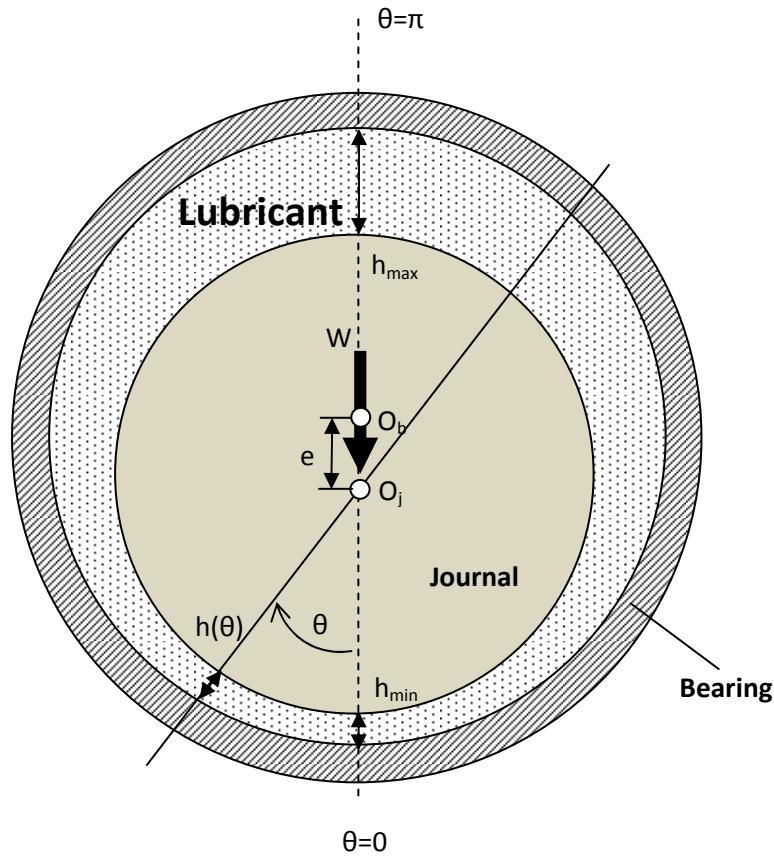


dependent on the properties of the material to be simulated. This means that if the deflection of all springs in a model is known, the load applied to the rigid part in the model can be calculated.

In order to create a model of a spherical bearing, a method of calculating the displacement of the ball into the liner is necessary, which gives the variation in displacement of the liner across the contact region. To calculate the displacement of the inner ball into the liner, the concept of eccentricity was used as in journal bearing theory. In a journal bearing the lubricant is oil; in a composite bearing the lubricant is solid, but the geometry of the space between the rigid parts is the same.

Figure 6.3 shows a journal bearing, with the journal (grey) surrounded by a lubricant, with the clearance between the journal and the bearing exaggerated. The clearance of the journal bearing,  $c$ , is the difference between the radius of the bearing ( $R_b$ ) and the radius of the journal ( $R_j$ ). The eccentricity of the journal,  $e$ , is the distance between the centre of the journal ( $O_j$ ) and the centre of the bearing ( $O_b$ ). The gap between the journal and the bearing,  $h(\theta)$ , varies dependent on its radial position,  $\theta$ , which is the angle measured from the centre of the journal. The minimum gap ( $h_{min}$ ) and maximum gap ( $h_{max}$ ) are found along the axis of load application in the case where there is no reciprocation. The axis of translation is the radial direction at the point where the gap is  $h_{min}$ , i.e.  $\theta = 0$ . In the composite bearing application this is also the direction of load application, as shown in Figure 6.3. (In a journal bearing the axis joining the maximum/minimum clearances does not in general align with the load axis due to the nature of the hydrodynamic lubrication mechanism which is governed by

the Reynolds equation).



**Figure 6.3** Diagram of journal bearing with lubricant, showing key components and dimensions

The eccentricity ratio,  $\varepsilon$ , is the eccentricity of the journal ( $e$ ) divided by the radial clearance of the bearing ( $c$ ). The eccentricity of the bearing is typically a few orders of magnitude smaller than the radius of the journal, so, as in hydrodynamic journal bearing theory, the gap between the journal and the bearing at any angular position may be closely approximated by

$$h(\theta) = c(1 + \varepsilon \cos \theta) \quad (6.3)$$

## 6.2 Spherical Plain Bearing Liner Contact Model

### 6.2.1 Relationship between Contact Load and Eccentricity

This model is first applied to the case of a two-dimensional journal bearing with a self-lubricating liner. In this case the gap,  $h(\theta)$ , is the distance between the journal and the outer race at a given radial position. For a very small load, just enough to give contact, the distance  $h_{min}$  would be the thickness of the liner,  $t$ . If a significant load is applied,  $W$ , this will cause the liner to deflect in the contact region, and the minimum gap will be less than the thickness of the liner. The deflection of points with gaps less than the thickness of the liner can be used in Equation 6.1, along with the calculation of liner deflection at a point,  $\Delta l = t - h(\theta)$ , to give

$$\sigma(\theta)_{contact} = \frac{E(t - h(\theta))}{L} \quad (6.4)$$

By dividing the area in contact into a series of points or nodes, with the deflection known at each of these points, a contact pressure contour can then be calculated.

For a flat bedspring model, the total load is found from the sum of all contact pressures multiplied by the associated area covered by each spring. In the journal bearing case, however, the spring axes are not parallel, therefore the load carried by each spring has to be resolved into the direction of the axis of load application. Figure 6.4 shows a spring with a gap of  $h(\theta)$ , highlighted in red, which is inclined at angle  $\theta$  from the axis of load application. If  $dA$  is the liner area corresponding to the spring, the amount of load carried along the axis of load application, will be

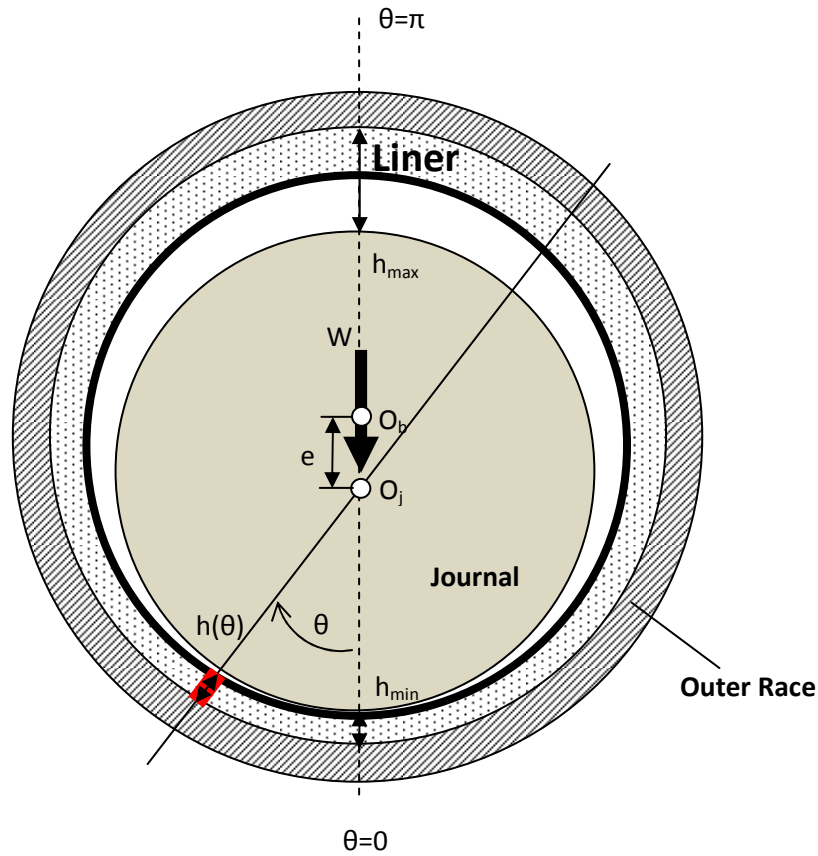
$$W_{\theta} = \cos \theta \frac{E(t - h(\theta))dA}{L} \quad \text{for } h(\theta) < t$$

$$W_{\theta} = 0 \quad \text{for } h(\theta) \geq t \quad (6.5)$$

The total load carried by the liner will be, for all points with  $h(\theta)$  less than the thickness of the liner,

$$W_{total} = \sum_{-\pi}^{\pi} W_{\theta} = \sum_{-\pi}^{\pi} \cos \theta \frac{E(t - h(\theta))dA}{L} \quad (6.6)$$

Equation 6.6 can be extended to the spherical case provided that  $\theta$  is then treated as the solid angle between the radial direction corresponding to area  $dA$  and the load direction.

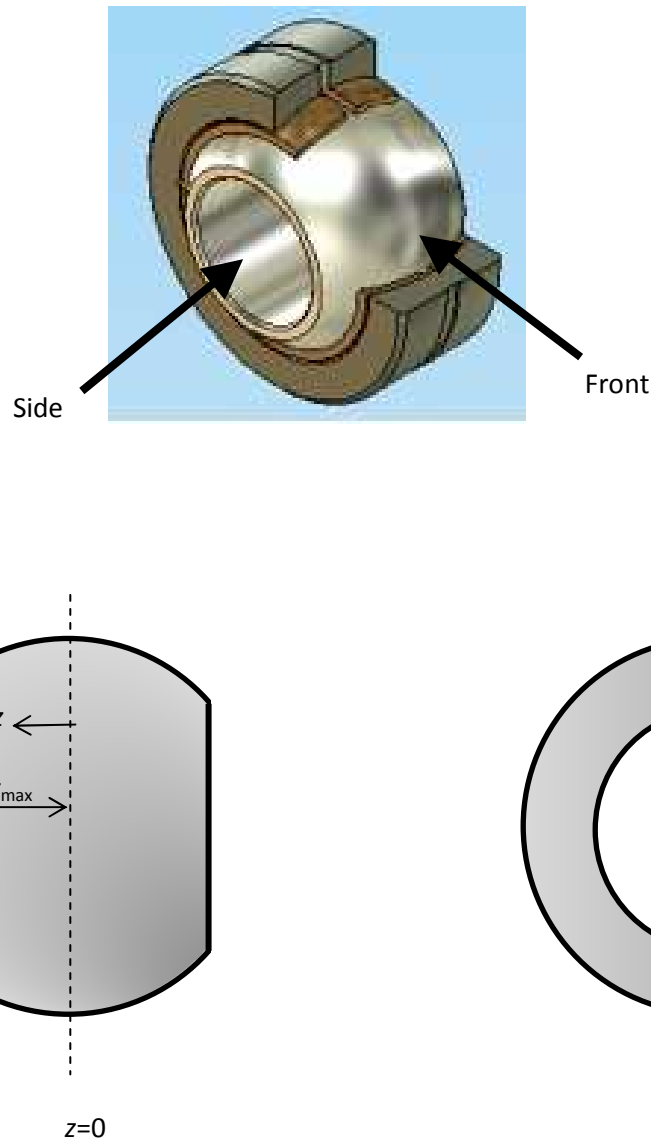


**Figure 6.4** Diagram of journal bearing adapted for self-lubricating liner, with a spring highlighted in red, and its associated radial position ( $\theta$ ) and gap ( $h(\theta)$ ) shown

### 6.2.2 Liner Contact Model Discretisation and Solution Method

By finding a solution to Equation 6.6 in three dimensions, we can calculate the load applied to the inner ball for a given eccentricity ratio. The solution is simplified by defining some of the variables according to the bearing quantities. The stiffness,  $E$ , is the stiffness of the liner, and is based on either empirical evidence or data from a finite element analysis of the material. The length of the springs,  $L$ , is the thickness of the liner, and the initial clearance,  $c$ , is known from the geometry of the bearing specified. This leaves only the area associated with the springs,  $A$ , the cosine of the solid angle between the spring and the load-line,  $\cos\theta$ , and the eccentricity ratio,  $\varepsilon$ , to be found.

In order to solve the problem analytically, the liner is divided by a mesh – a series of points (nodes) each with an associated area, material properties and representative geometry. In the 3D model, a mesh pattern is generated over the surface of the inner ball, and this mesh is then projected onto the liner. As the clearance between the inner ball and outer race is very small compared to the radius of the bearing, this is seen as an acceptable simplification. The mesh contains a series of nodes at which  $h(\theta)$  can be calculated. Nodes are defined by coordinates in  $(z, \alpha)$ . The  $z$ -coordinate is the axial distance measured from the inner ring mid-plane, and the  $\alpha$ -coordinate is the rotation about the ring axis as defined in Figure 6.5. The  $z$ -coordinate is the distance from the centreline ( $z = 0$ ) to the point of interest, and is positive to the left of the centreline, and negative to the right. The  $\alpha$ -coordinate is the angle measured from the line of load application ( $\alpha = 0$ ) and is negative in the clockwise direction, and positive in the anti-clockwise direction.



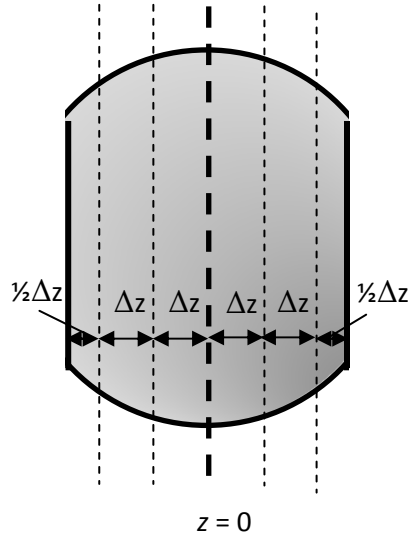
**Figure 6.5** Front- (left) and side-profile (right) of inner ring of spherical plain bearing, showing coordinate system and example point (AST Bearings, 2013)

The domain of  $z$  is  $-z_{max} < z < z_{max}$ , and the domain of  $\alpha$  is  $-\pi < \alpha < \pi$ . The mesh of nodes divides the spherical surface of the inner ring in equal increments of  $z$  and  $\alpha$  and this is referred to as a regular mesh spacing, although the distance between mesh points and the spherical surface is not uniform. In the  $z$ -dimension, the mesh is split into a series of nodes with a spacing of  $\Delta z$  in the  $z$ -direction. This quantity is calculated in the following manner,

where  $n_z$  is the number of divisions in the  $z$  dimension.

$$\Delta z = \frac{2z_{\max}}{n_z} \quad (6.7)$$

Nodes are required on the centreline,  $z = 0$ , so it is therefore necessary that  $n_z$  is an odd number. This is illustrated in Figure 6.6.



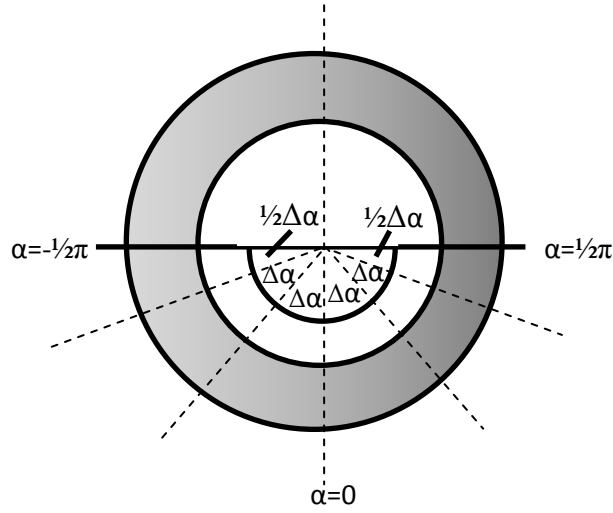
**Figure 6.6** Front-profile of inner ring of spherical plain bearing, showing  $z$ -dimension mesh when  $n_z=5$ , with nodes lying along dashed lines

In the  $\alpha$ -dimension, a similar equation is used, with  $\Delta\alpha$  being the spacing between points in radians, and  $n_\alpha$  the number of divisions in the  $\alpha$  dimension. For a constant load direction relative to a fixed outer race, contact can only occur on one half of the liner, irrespective of movement of the inner ball, and for this case the domain of  $\alpha$  was adjusted to  $-\frac{1}{2}\pi < \alpha < \frac{1}{2}\pi$ , to significantly reduce the number of calculations. To allow the future potential for

introduction of a moving load line however,  $\alpha_{\max}$  is left as an adjustable parameter.

$$\Delta\alpha = \frac{2\pi}{n_\alpha} \quad (6.8)$$

Nodes are required on the centreline,  $\alpha = 0$ , and do not extend to the far edge of the inner ring. It is therefore also necessary that  $n_\alpha$  is an odd number. This mesh is illustrated in Figure 6.7.



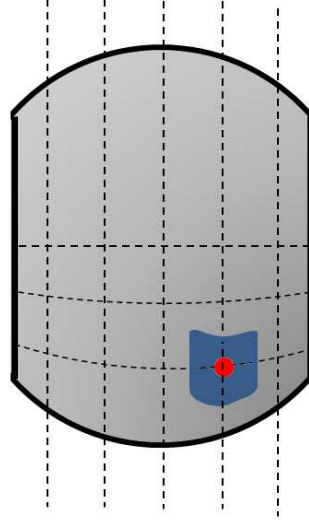
**Figure 6.7** Side-profile of inner ring of spherical plain bearing, showing  $\alpha$ -dimensional mesh when  $n_\alpha=5$ , with nodes lying along dashed lines

Figure 6.8 shows the two meshes combined, with an example point highlighted in red and its associated area highlighted in blue. The area associated with a node is half the distance to its neighbouring nodes on all sides in both the  $z$ -axis direction and  $\alpha$ -axis direction. In the case of a flat plane with  $x$ - and  $y$ -axes, the area would be

$$A = (1/2dx + 1/2dx) \times (1/2dy + 1/2dy) = dx dy \quad (6.9)$$



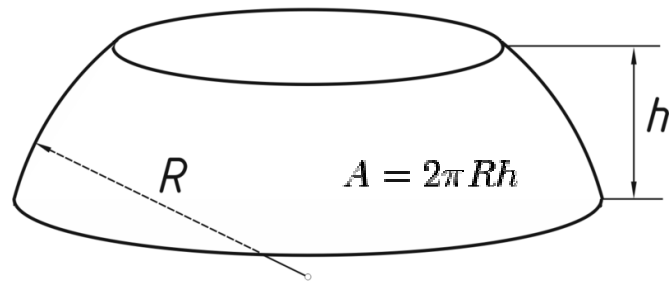
This model is however spherical, and this spherical geometry must be taken into account when determining the area associated with a node.



**Figure 6.8** Node (red) with associated area highlighted (blue)

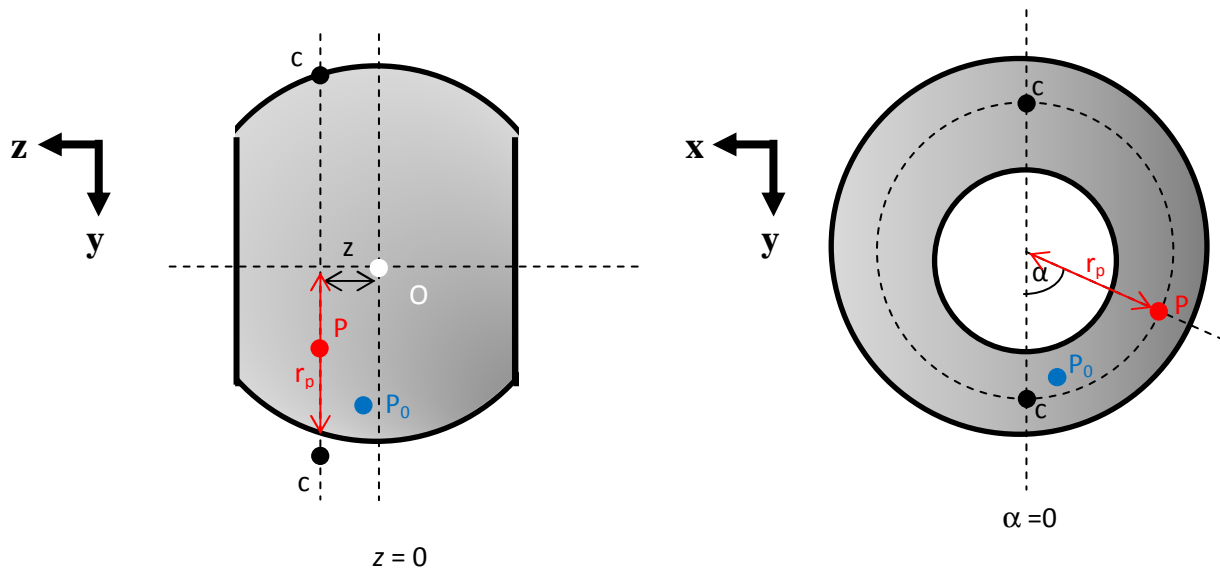
Due to the equal spacing of the mesh, each point will have the same associated area. The sphere is divided into spherical segments in the  $z$ -dimension, which have a surface area of  $2\pi Rh$ , where  $R$  is the radius of the sphere and  $h$  is the height of the segment. This is illustrated in Figure 6.9. In this model, the height of the segment is  $dz$ , and the radius of the sphere is the radius of the outer race,  $R_{out}$ , minus the thickness of the liner,  $t$ . The area associated with a node is therefore (Stojek & Osteryoung, 1989)

$$A = \Delta\alpha(R_{out} - t)\Delta z \quad (6.10)$$



**Figure 6.9** Key dimensions of spherical segment (Stojek & Osteryoung, 1989)

To derive a formula for calculating  $\cos\theta$  for all points, we consider two points on the surface of the inner ball –  $P_0$ , the point through which the load acts, and  $P$ , a general point of interest – and the origin at the centre of the sphere,  $O$ .  $P_0$  has the coordinates  $(z_0, \alpha_0)$  and  $P$  has the coordinates  $(z, \alpha)$ . This is illustrated in Figure 6.10



**Figure 6.10** Front- and side-profile of an inner ball showing points  $P$  (red) and  $P_0$  (blue) along with the associated dimensions of  $P_0$

From vector trigonometry, the cosine of the angle between the vectors  $\overline{OP}$  and  $\overline{OP_0}$  is

$$\cos \theta = \frac{\overline{OP} \bullet \overline{OP_0}}{|\overline{OP}| \cdot |\overline{OP_0}|} \quad (6.11)$$

If  $r_p$  is the radius of the circle on which point  $P$  is located, and  $r_{p0}$  is the radius of the circle on which point  $P_0$  is located, then  $\overline{OP}$  and  $\overline{OP_0}$  are given by

$$\overline{OP} = -r_p \sin \alpha \cdot i + r_p \cos \alpha \cdot j + z \cdot k$$

$$\text{and } \overline{OP_0} = -r_{p0} \sin \alpha \cdot i + r_{p0} \cos \alpha \cdot j + z_0 \cdot k \quad (6.12)$$

Combining the two gives

$$\overline{OP} \bullet \overline{OP_0} = (-r_p \sin \alpha \cdot i + r_p \cos \alpha \cdot j + z \cdot k) \cdot (-r_{p0} \sin \alpha_0 \cdot i + r_{p0} \cos \alpha_0 \cdot j + z_0 \cdot k)$$

$$\overline{OP} \bullet \overline{OP_0} = r_p r_{p0} (\sin \alpha \sin \alpha_0 + \cos \alpha \cos \alpha_0) + z z_0 = r_p r_{p0} \cos(\alpha - \alpha_0) + z z_0 \quad (6.13)$$

As both points  $P$  and  $P_0$  lie on the sphere with radius  $R$

$$|\overline{OP}| = R \quad \text{and} \quad |\overline{OP_0}| = R \quad (6.14)$$

Therefore

$$\cos \theta = \frac{\overline{OP} \bullet \overline{OP_0}}{|\overline{OP}| \cdot |\overline{OP_0}|} = \frac{r_p r_{p0} \cos(\alpha - \alpha_0) + z z_0}{R^2} \quad (6.15)$$

From Pythagoras' theorem we have

$$r_p^2 + z^2 = R^2 \therefore r_p^2 = R^2 - z^2 \quad \text{and} \quad r_{p0}^2 + z_0^2 = R^2 \therefore r_{p0}^2 = R^2 - z_0^2 \quad (6.16)$$

Therefore

$$\cos \theta = \frac{\overline{OP} \bullet \overline{OP_0}}{|\overline{OP}| |\overline{OP_0}|} = \frac{(\sqrt{R^2 - z^2} \bullet \sqrt{R^2 - z_0^2} \cos(\alpha - \alpha_0) + zz_0)}{R^2} \quad (6.17)$$

All necessary variables are now available to solve Equation 6.6, except for  $\varepsilon$ .

$$W_{total} = \sum_{-\pi}^{\pi} W_{\theta} = \sum_{-\pi}^{\pi} \cos \theta \frac{E(t - h(\theta))dA}{L} \quad (6.6)$$

Equation 6.6 shows a direct relationship between  $W_{total}$  and  $\varepsilon$ . To find the eccentricity of the inner ball for a given load  $\varepsilon$  is varied until the total load for all points is the same as the given load, +/- an error percentage. This is carried out numerically by repeated division.

Two values for  $\varepsilon$  are initially created,  $\varepsilon_{high}$  and  $\varepsilon_{low}$ , and are given the following initial values

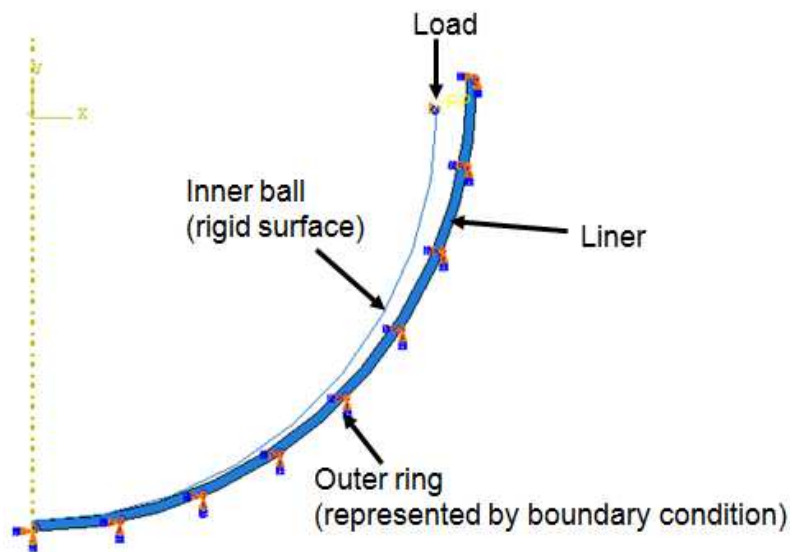
$$\varepsilon_{low} = 1 - \frac{t}{c} \quad \text{and} \quad \varepsilon_{high} = 1 \quad (6.18)$$

An  $\varepsilon$  value of 1 means that  $e/c$  is equal to 1, therefore the eccentricity is the same as the clearance, meaning the inner ball has completely compressed the liner and has reached the depth of the outer race at a point.  $\varepsilon_{high}$  is initially set to this value as, in this model, it is not possible to have a higher eccentricity than the clearance of the bearing, as the outer race is rigid and cannot deflect. For the case where the inner ball is just touching the liner (under almost no load), the eccentricity of the inner ball is  $c-t$ , and as  $\varepsilon = e/c$ , this gives  $\varepsilon_{low} = 1 - \frac{t}{c}$ .

The total load is initially calculated at a value of  $\varepsilon$  exactly half way between  $\varepsilon_{\text{high}}$  and  $\varepsilon_{\text{low}}$ . If the load is found to be too high,  $\varepsilon_{\text{high}}$  is changed to the current  $\varepsilon$  value, and a new  $\varepsilon$  is found between the new  $\varepsilon_{\text{high}}$  and  $\varepsilon_{\text{low}}$ . If the load is too low,  $\varepsilon_{\text{low}}$  is changed to the current  $\varepsilon$  value, and a new  $\varepsilon$  is found between the new  $\varepsilon_{\text{high}}$  and  $\varepsilon_{\text{low}}$ . This process is repeated until the  $\varepsilon$  value gives the specified load, within a user-defined error margin.

### 6.2.3 Comparison of Liner Contact Model and equivalent Finite Element model

The simple bedspring model differs from a finite element model primarily due to the fact that adjacent springs have no connection, unlike a finite element model where adjacent elements are connected. This means that in a bedspring model only springs which are within the contact area are deflected, whereas in a finite element model there is some deflection outside of the contact area. For a given geometry and load the overall contact pressure contour was compared between the bedspring model and a finite element model using DSS Abaqus software. The model represents a steel spherical plain bearing having an inner ball radius of 20 mm and a steel outer race of radius 22 mm, with a 0.5 mm thick liner around the interior of the outer race, with an assumed stiffness of 10 GPa. Figure 6.11 shows this geometry as assumed in the finite element model. The finite element model is axi-symmetric and two-dimensional, comprising of a rigid arc of 20 mm radius to represent the inner ball, and a 0.5 mm thick liner of outer radius 22 mm, with an encastre boundary condition along its outer edge to represent the outer ring. The inner ball and outer ring are not represented as elastic parts as their stiffness is an order of magnitude ( $>20\times$ ) larger than that of the liner. Both models had a mesh applied such that there were at least 100 nodes in the contact region.



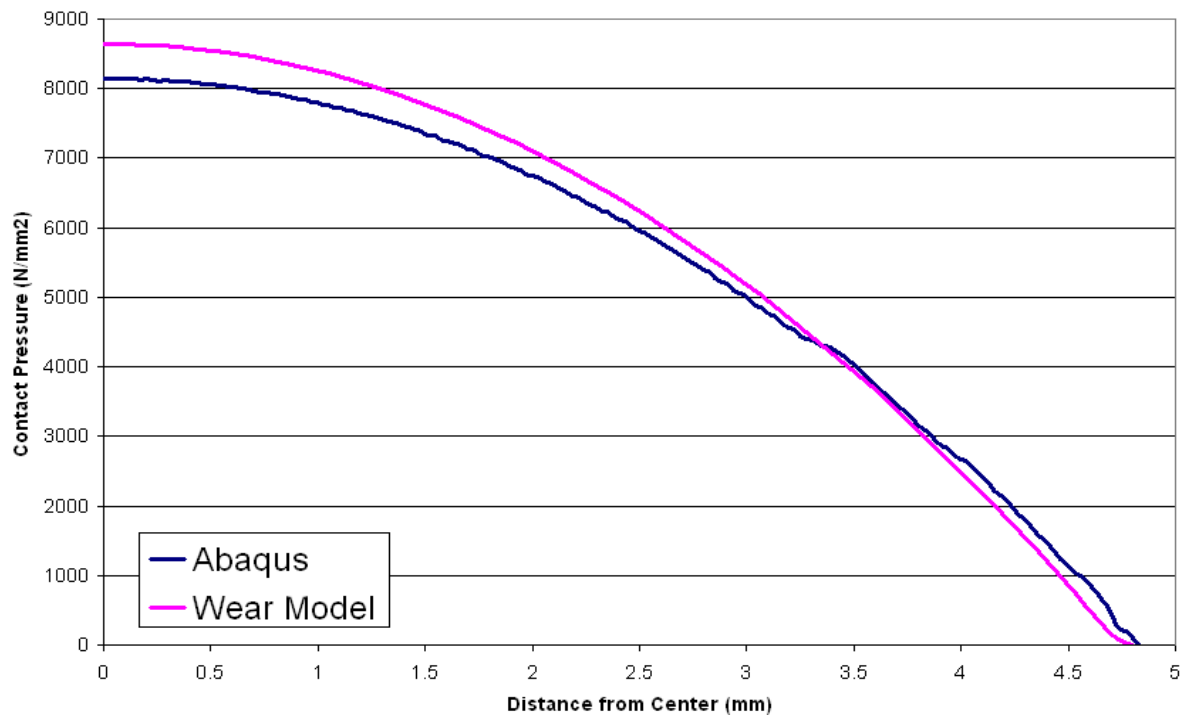
**Figure 6.11** Finite element model of journal bearing with self-lubricating liner

Figure 6.12 shows the results obtained from the the bedspring-based model and the finite element model. The key differences are:

- The bedspring model contact pressures are distributed over a slightly smaller area. This is to be expected as a limitation of the bedspring model is that it does not allow for deflection (and therefore stress) outside of the contact region, whereas finite element analysis does account for this effect. The difference in the contact dimension is minor (<2%) and is therefore not seen to be significant.
- The bedspring model exhibits a higher contact pressure in the centre of the contact, with a slightly lower contact pressure at the outer edge of the contact. This is due to the difference in deflected shape between the liner in the liner contact model and

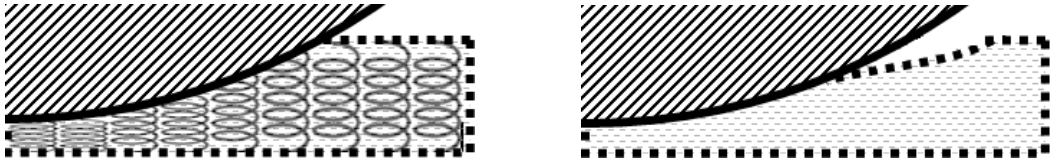
finite element model, as shown in Figure 6.13.

The differences between the two models were small, and the bedspring model was seen to be an acceptable approximation of the contact behaviour in the spherical plain bearing.



**Figure 6.12** Comparison of results of finite element (FE) model with bedspring model for the assumed journal bearing geometry. The distance from centre is a radial distance, not a vector distance in the  $x$ -axis/ $z$ -axis direction.

*Note: The overall load integrated across the contact region appears to be higher for the bedspring model than the finite element model, however as this is a circular contact the load should be integrated across  $\pi r^2$ , which gives the two loads as equal to within 1%.*



**Figure 6.13** Comparison of exaggerated deflected shape of liner between bedspring model (left) and finite element model (right)

### 6.3 Adding Wear to the Liner Contact Model

#### 6.3.1 Overview

In Chapter 4 the effects of wear of the composite liner on contact pressure and net friction were modelled by prescribing the wear process as one in which uniform layers of the surface are removed to reveal different strata of the textile/resin mixture. The aim of the work described in the following sections was to predict the instantaneous rate of wear of the liner based upon an empirical wear model which assumes basic wear parameters for the individual components of the composite. The wear model adopted is the simple Archard wear law as follows

$$Q = K \frac{WL}{H} \quad (6.20)$$

This equation gives  $Q$ , the total volume of wear debris ( $\text{m}^3$ ), dependent on  $W$ , the total normal load,  $H$ , the hardness of the softer of the two contacting materials,  $K$ , a dimensionless constant, and  $L$ , the sliding distance.

For an area of  $\Delta A$ , the rate of change of liner thickness ( $dt/d\zeta$ , where  $t$  is liner thickness and  $\zeta$



is time) will therefore be

$$\frac{dt}{d\zeta} = \frac{Q}{dt\Delta A} = K \frac{Wu}{H\Delta A} \quad (6.21)$$

Where  $u$  is the sliding speed ( $u=L/d\zeta$ ) for area  $\Delta A$ .  $W/\Delta A$  is the local pressure,  $p$ . From equation 6.21 we then have

$$\frac{dt}{d\zeta} \Delta A = \frac{K}{H} up \quad (6.22)$$

Let  $\Delta t$  be the depth of material removed per cycle. For a constant load, constant load direction and a stationary outer ring we may write

$$\Delta t = \frac{Kp}{H} \int_0^{\zeta_0} u d\zeta \quad (6.23)$$

Where  $\zeta_0$  is the period of one cycle of oscillation.  $S$ , the sliding distance of the inner ball relative to the liner position considered over one cycle of oscillation is

$$S = \int_0^{\zeta_0} u d\zeta \quad (6.24)$$

Adding wear to the liner contact model involves varying the liner thickness at a given point to simulate wear based on load and sliding distance, together with a modification of the pressure distribution across the liner surface based on the change in thickness. Equation 6.25 shows the contact pressure for a local liner thickness  $t$ . If we allow for changes in  $t$ , for a given

displacement ( $h(\theta)$ ) contact pressure will increase as spring length decreases.

$$\sigma(\theta)_{contact} = \frac{E(t - h(\theta))}{t} \quad (6.25)$$

By varying  $t$  in a controlled manner, and periodically recalculating the load distribution for the modified spring lengths, it is possible to simulate wear in the bearing liner.

### 6.3.2 Sliding Distance

In order to determine the sliding distance of a point on the liner against the inner ring over a cycle, we find the integral of the sliding speed (with respect to time) over the period of one cycle. The sliding speed of the inner ring on the liner depends on the operating conditions, i.e. the oscillation angle and frequency of oscillation in the reciprocation and misalignment directions. In this model, only oscillation in the reciprocation direction is considered, as most existing test data have been obtained using this motion.

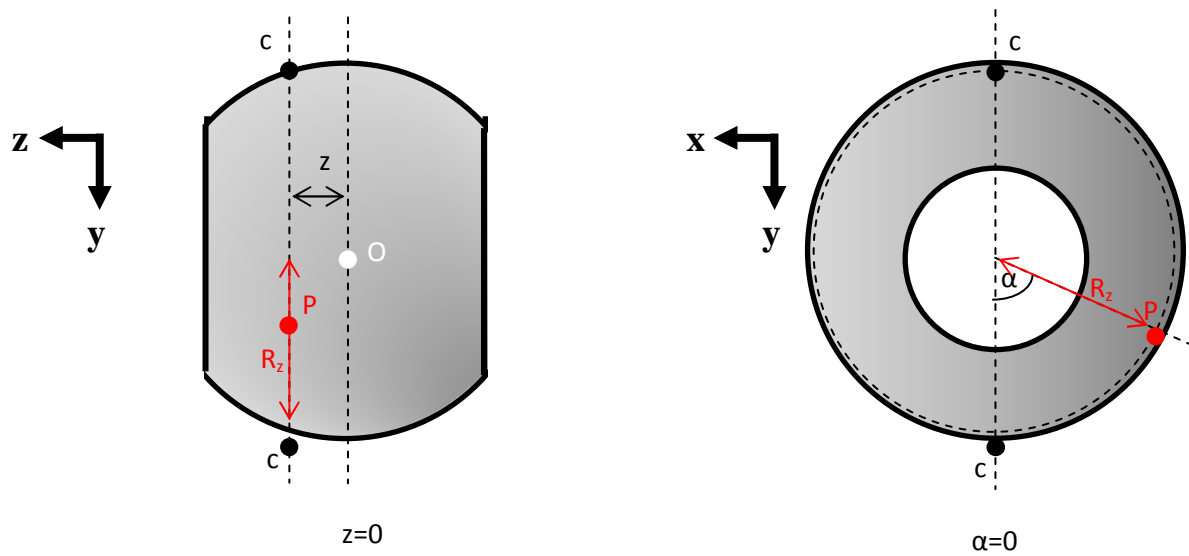
The distance travelled by a point ( $u$ ) moving around a circle of radius  $R$  by  $\beta$  radians is

$$R \cdot \beta \quad (6.26)$$

Dependent on the position of a point which lies on a rotating sphere, the radius of the circle on which it travels is equal to or less than the radius of the sphere, as highlighted in Figure 6.14. The radius of the circle,  $R_z$ , on which a point,  $P$ , lies in the  $z$ -axis direction is determined by

$$R_z^2 + z^2 = R^2 \quad \text{therefore} \quad R_z^2 = R^2 - z^2 \quad (6.27)$$

Where  $R$  is the radius of the inner ball, and  $z$  is the distance from the centreline of the point in the  $z$ -axis, illustrated in Figure 6.14.



**Figure 6.14** Front- and side-profile of an inner ball showing point  $P$  (red) and the radius of the circle on which it lies in the  $z$ -axis,  $R_z$ .

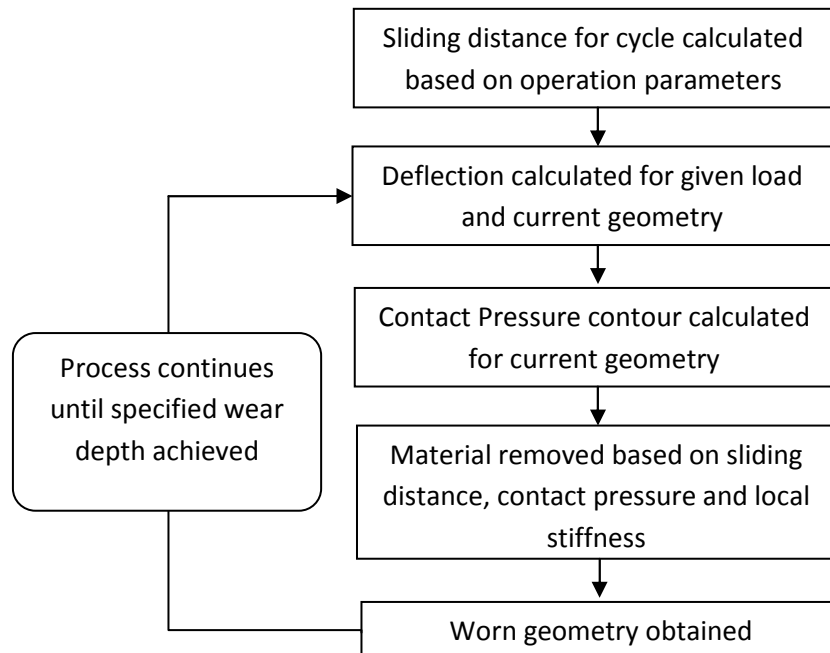
Oscillation in bearings is usually described as  $\pm X^\circ$ . This means that for a point lying directly on the line of load, it will move  $X^\circ$  in one direction, then  $X^\circ$  back to its starting position, then  $X^\circ$  in the opposite direction, then  $X^\circ$  to return to its starting position. This is the movement undertaken in one cycle. For an oscillation angle  $\pm X^\circ$ , the total angular distance travelled by the point will be  $4 \times X^\circ$ .

The total sliding distance over one cycle ( $S$ , in Equation 6.24) for a point with  $z$ -direction dimension  $z$ , and oscillation of  $\pm X^o$ , on a sphere of radius  $R$  will therefore be

$$S = \sqrt{R^2 - z^2} \cdot 4 \cdot X^o \cdot \frac{2\pi}{360} \quad (6.28)$$

### 6.3.3 Wear Model Operation

Figure 6.15 shows how the wear of the bearing is determined computationally. The routine runs in a closed loop, which continues to “wear” the liner until a pre-determined level of wear has been reached.



**Figure 6.15** Schematic of wear model routine

The Wear Model produces three key outputs: the wear profiles; contact pressure contours at discrete intervals; and the progression of backlash through the bearing's life. The “discrete intervals” correspond to whole numbers of cycles which can be varied to increase or reduce the number of data produced by the model.

The contact pressure profile is obtained for information only at this stage, but in future applications of the model, where new materials may be under development, it may be helpful as an indicator of pressure and temperature “hotspots”. The wear profile is output at discrete numbers of cycles so that comparisons can be made to the wear profiles measured in actual bearing tests.

#### **6.4 Results and Comparison with Test Data**

The results of the wear model may be compared with measured backlash values across the life of a bearing. By using the same parameters as an actual bearing test for the motion, load and geometry of a real bearing, results can be compared with bearing tests.

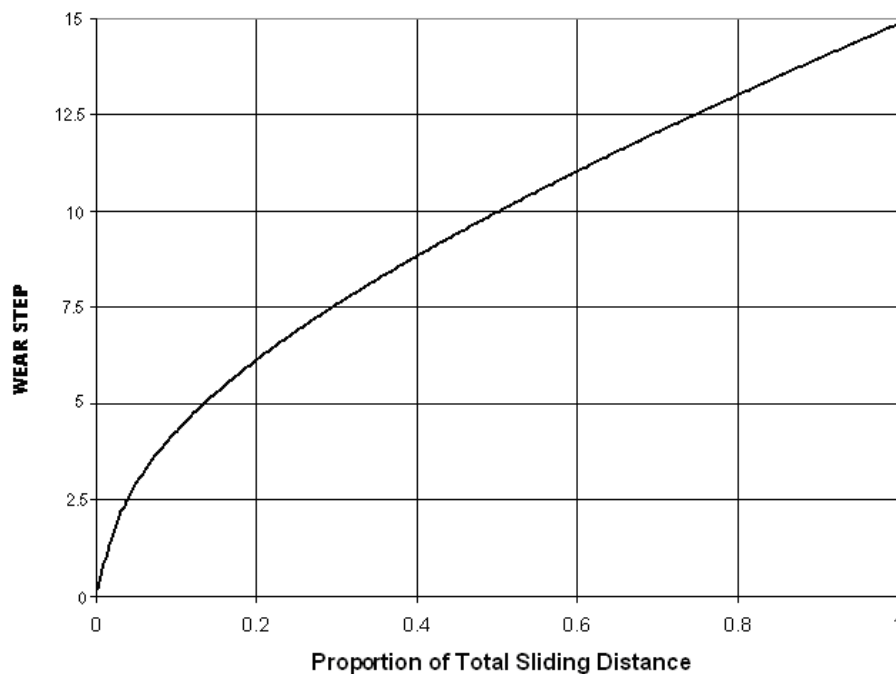
Bearing backlash values are usually monitored off-line during qualifying tests, i.e. a test has to be stopped, and in some cases parts removed, in order to measure the backlash value. This means that over the life of a bearing, there may only be one backlash value taken. A test rig was used to monitor backlash values on-line whilst the test rig continued to operate. These values do not compensate for the deformation of the liner due to load, as they are measured

from the deflection of the inner ring. In these tests the bearings were run until the bearing temperature reached a cut-off limit. It is not known at what locations these temperatures were taken in the bearing. Both ambient and bearing temperatures were recorded over the course of the tests, and three bearings were tested. Measured dynamic backlash values were obtained periodically during the test and are presented in terms of the mean sliding distances at the measurement intervals. The results of these tests are commercially confidential, consequently some details of the test and wear model parameters are removed.

The wear model was given a set of conditions to closely match those of the bearings tested physically. The bearing was assumed to be in perfect conformity with manufacturing specifications – i.e. it met all tolerances. The simulation was allowed to run until the liner was almost entirely worn (the maximum depth was 99% of its thickness), and the simulation covered the range of wear allowed to take place in the actual tests. The stiffness was set to an appropriate value, and the load matched to that of the physical tests, as were the frequency and angle of oscillation in the radial direction. No oscillation in the misalignment direction was included.

As no appropriate  $K$  value (the wear constant assumed in the Archard wear law) had yet been found, this was set to  $1 \times 10^{-6}$ , to ensure a high number of cycles to resolve the maximum wear depth. The mesh density in the  $\alpha$  and  $z$  directions was increased until increasing them further showed no significant change in the results obtained. The load error margin (the difference between the load calculated iteratively and the real load applied) was set at 0.01%.

As the real bearing tests do not account for deflection of the liner, Figure 6.19 shows the modelled deflection of the inner ring due to the combination of liner wear and liner deflection. Wear depth is presented as a function of  $\Delta$ , the “wear step” discussed in previous chapters. As no appropriate  $K$  value was determined within the timeframe of the project, the predicted deflection is shown plotted against sliding distance normalised with respect to total sliding distance.

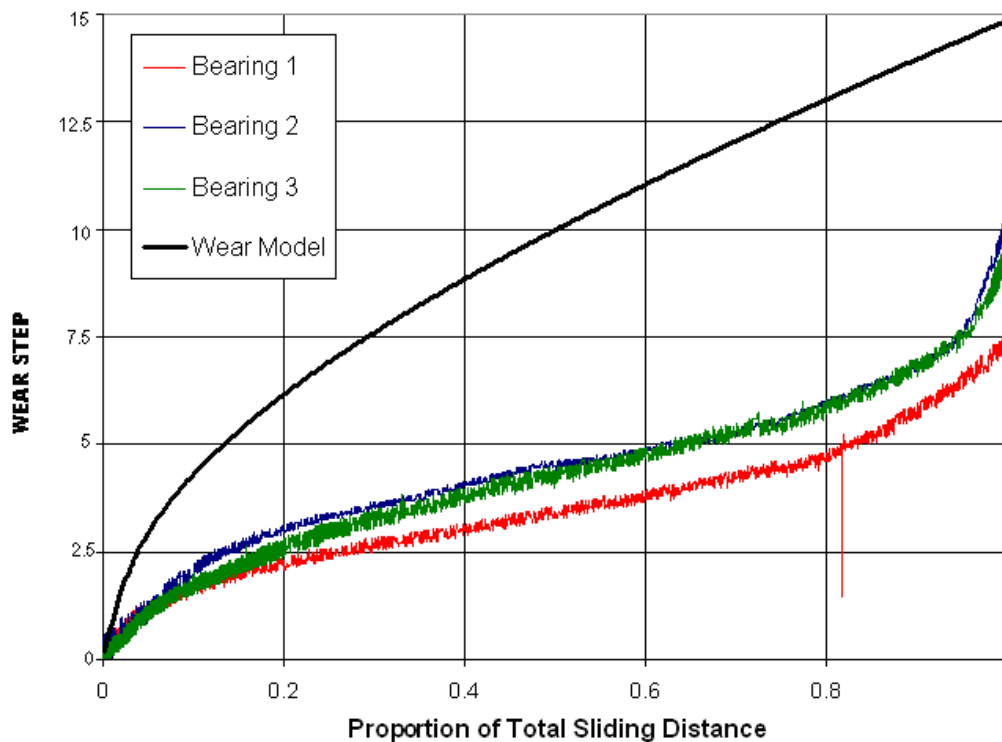


**Figure 6.19** Inner ring deflection as a proportion of total sliding distance from the wear model

Figure 6.19 clearly shows the familiar two key features reported in both the literature and observed in the real bearing tests discussed earlier. First, the “phase 2” linear wear rate behaviour after 20% of its total sliding distance, and, second, the rapid increase in wear in

“phase 1” before 20% of its total sliding distance. The simulation does not, however, exhibit the “phase 3” wear out behaviour of a rapid increase in wear in the final 20% of the wear life.

Figure 6.20 shows the predictions of the wear model compared to the real bearing tests.

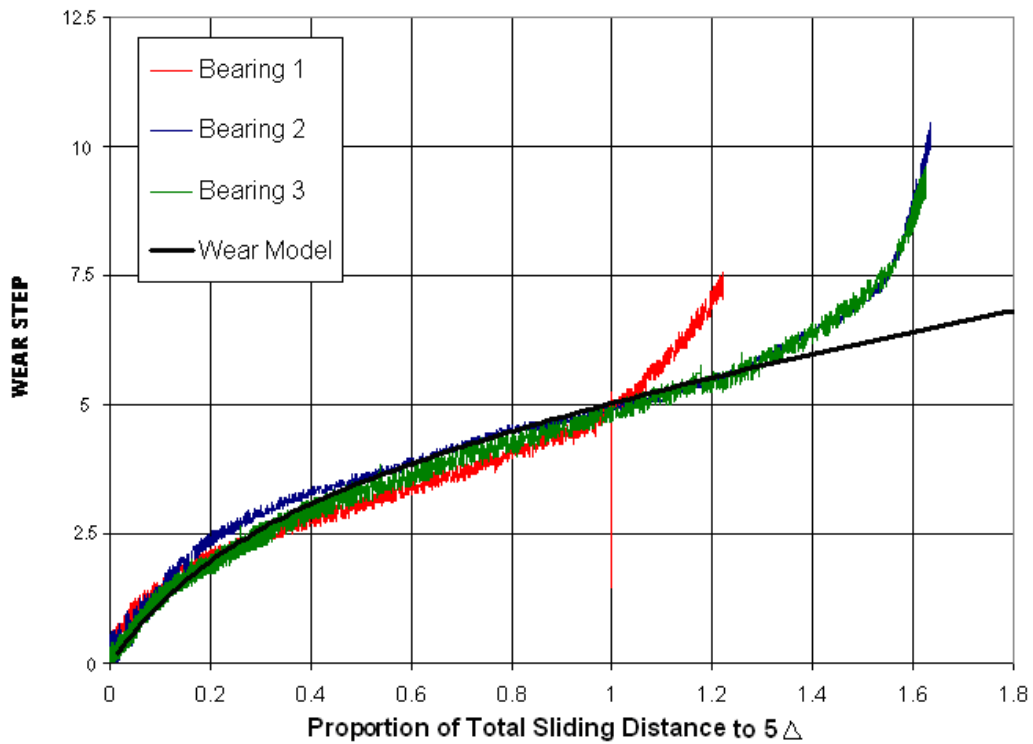


**Figure 6.20** Real bearing test and wear model results showing inner ring deflection as a proportion of total sliding distance

Figure 6.20 shows that while the form of the results of the wear model is similar to the real bearing tests in the first 80% of its total sliding distance (i.e. a slowing rate of increase of wear with sliding distance), there is a difference in the magnitude of wear between the results by a factor of about 2.5. This may be explained as follows. The wear model is allowed to



wear to a much greater depth than is possible in real bearing tests, and the proportion of the total sliding distance is a proportion of the sliding distance up to a wear of  $30 \Delta$ . From the real bearing test data, Bearings 1 and 3 show that a wear depth of  $5\Delta$  is achieved at 60% of the total sliding distance. All bearing test data and the wear model predictions were therefore re-normalised, this time with sliding distance as a proportion of sliding distance to achieve  $5\Delta$  deflection, as shown in Figure 6.21.



**Figure 6.21** Real bearing test and wear model results with inner ring deflection presented as a proportion of sliding distance to  $5 \Delta$  inner ring deflection

The main difference between the wear model and real bearing test results are now seen to be in the region of 70% to 100% final backlash. The real bearing tests show an increasing wear

rate over this period which is not reflected in the wear model predictions. In real bearings, this is believed to be the result of increased presence of reinforcement material in the contact region, which increases the wear rate (as discussed in Chapter 1). The wear model however does not have a variable wear rate, and the only attribute linked to the increase in reinforcement material in the contact is the increase in localised stiffness.

The wear model exhibits the behaviour seen in the first two zones of the familiar three-zone curve, discussed by King (1979) and others, which is encouraging. This correlation between the wear model and the “knee” between zones one and two is of particular note as this feature is commonly attributed to the development of a PTFE “transfer layer”, yet no information regarding such effect is included in the model. While micrography of surfaces sliding with PTFE do show the presence of such a transfer layer (Yang et al., 2009), some researchers believe it to be developed extremely early in the wear process (Briscoe et al., 1988), long before reaching ~20% of the total lifetime cycles. It is therefore hypothesised that this “knee” is not the result of development of a PTFE transfer layer, but a geometrical effect of spherical plain bearings. Initially there is very small load application region on the unworn bearing liner, leading to high localised contact pressures and therefore wear rates. As the liner wears, the load application region of the inner ball increases, reducing both localised contact pressure and wear rate. The “wear out” transition between zones 2 and 3 on the real bearing tests however could be a result of the failure of the transfer layer, leading to increased wear rates. As the transfer layer (and its eventual failure) is not included in the wear model, this could explain why the “wear out” feature is not seen in the wear model.

## **7. Conclusions and Future Work**

### **7.1 Overview**

The work described in this thesis was concerned with experimental measurement and theoretical modelling of both friction and wear of a particular self-lubricating, composite bearing liner material. A finite element-based friction model was developed which took account of the detailed physical structure and elastic response of the PTFE/reinforcement textile weave/resin filler composite liner loaded in contact with a steel counterface. The effect of increasing wear on the contact and friction behaviour was modelled by progressively removing layer after layer of the contacting face of the FE model to reveal different proportions of the constituent materials of the composite in contact. In this way a net friction versus wear depth graph was obtained. The friction coefficients of the individual components of the composite assumed in the model were taken from both the literature and from values actually measured in the test rig. The predicted net friction values using friction coefficients from these two sources were then compared to the overall friction measured in a bespoke friction and wear test rig. In general the predicted net friction values based on the individual friction coefficients obtained from the literature were significantly higher than the corresponding measured values. It was found that the calculation was particularly sensitive to the friction coefficient of the resin filler, and closer agreement between predicted and measured net friction was obtained assuming a (lower) friction coefficient actually measured in the test rig using an isolated resin sample.

A numerical wear model for the composite liner was developed based on a simplified “bedspring” formulation for the elastic behaviour of the liner in contact with the steel counterface. The Archard wear law was adopted in an iterative scheme to predict the progression of wear with sliding distance (under constant load), taking account of the increased conformity and redistribution of contact pressure due to wear itself. The results from the wear model were compared with the results of full-scale bearing tests carried out earlier by SKF, and good agreement was obtained for the first 80% of the wear life of the liner. The remaining sections of this chapter present a discussion of proposed future work on the friction model, flat-on-flat coupon tests, and the bearing wear model, along with a summary of the main conclusions of the thesis.

## **7.2 Aims and Objectives Met and Contributions**

- A representative model of the liner material was created, which is both efficient and useful.
- A friction model for the bearing liner was created. It was found that incorporating the results of the finite element analysis did not increase the accuracy of the model, but the model provides a useful prediction of the variation in coefficient of friction over the operating life of the bearing liner provided appropriate coefficients of friction are used for the constituent materials.
- Experimental data from the flat-on-flat wear testing rig was obtained, however due to problems with the reliability of the rig, the data obtained were limited.

- A wear model was produced by adapting lubricated journal bearing theory, which proved to be accurate for the first 80% of the wear life of a practical bearing liner.
- Results from the wear model show good agreement with the initial wear behaviour of full-scale bearing tests without accounting for presence of PTFE. This suggests that the formation of a PTFE transfer layer is not responsible for the transition between initial and steady state wear behaviour as discussed in relevant literature, and that the transition is in fact a geometric effect.

### **7.3 Future Work – Friction Model**

The friction model showed encouraging results when appropriate coefficients of friction were assumed for the constituent materials and when the reciprocating sliding distance amplitude was greater than 25 mm. The model matches the steady-state (i.e. constant wear rate) period of the trend of friction coefficient over the wear life of the bearing liner, and also the spike in friction coefficient seen in some test results. It is notable that the method of predicting the friction coefficient without the inclusion of the detailed elastic contact pressure distribution provides good agreement with the experimental results, as this method is significantly simpler to implement than that which calculates the pressure contours across the contact surface. There was a lack of agreement in the results when the reciprocating sliding amplitude is less than 25 mm. As discussed in Chapter 5, the particularly low coefficient of friction seen with a sliding distance of 12.5 mm could be due to either the formation and maintenance of a PTFE “transfer layer”, or possibly a thermal effect in the contact region. Suggestions for the investigation of this effect are discussed in Section 7.3. To account for

the impact of these effects on the coefficient of friction, some form of sliding amplitude based parameter should be included in the model. In the experimental testing it was also noted that lower mean contact pressure resulted in a higher steady-state coefficient of friction, therefore it may be necessary to include some degree of pressure-dependence in the values of the individual friction coefficients of the constituent materials in future work.

The current model should be validated using other dry-sliding materials. This would require further testing on the existing flat-on-flat coupon test rig. It would be desirable for this material to either have the same structure as the current material, but with one material changed (for example the resin), or for it to contain exactly the same materials, but in a different weave structure, perhaps. This would help identify the variables which most affect the model predictions and hence the real bearing behaviour.

Other factors which were not investigated experimentally in this project include the effect of counterface surface roughness and humidity. These are factors which have been identified in the literature review as having a significant effect on the coefficient of friction of liner materials. These factors are both discussed further in Section 7.3, but including them in the friction model would require further parameters to be considered.

The friction model should be developed to model friction in full-scale bearings over a range of operating conditions. This would require development of a full FE model of the bearing liner and the two spherical components in order to yield the extent of the zone of contact and

the detailed pressure distribution under load.

It was noted in Chapter 1 that “bearing torque” (or overall bearing friction) is generally higher under “no-load” conditions, where a pre-load is introduced by manufacturing an “overclosure” which ensures that new bearings have an initial contact pressure which is relaxed as backlash develops due to wear. In this case inclusion of a contact pressure dependency on the friction coefficient would allow comparison between loaded and unloaded bearing friction. If the concept of a critical sliding distance is also included, this would allow identification of bearing geometries which may be inappropriate or inefficient in a given application. For a given load and angle of oscillation, for example, reducing the diameter of the bearing (subject to available load capacity, of course) also reduces the circumferential sliding distance, therefore by reducing the diameter of the bearing, it is possible in some applications that the coefficient of friction of the bearing will also be reduced. The current friction model developed in this project is therefore a useful starting point for the development of a more comprehensive model for industrial design purposes.

## **7.4 Future Work – Experimental Data**

As discussed in Chapter 5, the number of data obtained from the flat-on-flat coupon test rig within the timeframe of this project was limited. It is suggested that test regime D in particular requires further investigation, as this showed a significantly reduced steady-state coefficient of friction. Further investigation into the relationship between coefficient of friction and pressure should also be carried out, as this relationship can be combined with

calculated contact pressure contours across the liner in real bearing geometries to give an estimation of bearing friction under a range of loading conditions.

If, in the light of further testing, the results of test D1 are shown not to be anomalous, then further tests using sliding distances between that of test C and test D should be carried out to investigate the sliding-distance related transition between the two steady-state coefficients of friction. It has been proposed that there may be a critical reciprocating sliding amplitude, below which the friction coefficient attains a significantly reduced plateau value. An alternative hypothesis is that below the critical sliding distance, the coefficient of friction is lowered as sliding distance reduces further. This second hypothesis is thought to be less likely, as the coefficient of friction of  $\sim 0.035$  seen in test D1 is similar to that observed in full-scale bearing tests (Henninger, 2011) and, importantly, in coupon fretting tests of the material, which have very low sliding distances (Dayot, 2011). The proposed concept of a critical sliding amplitude associated with a significantly reduced steady-state coefficient of friction should also be investigated with regard to whether it is contact-pressure dependent or not.

If a critical sliding distance exists, the next step is to investigate whether it is due to thermal effects or the formation of a third body transfer layer. Options could include introducing a heating element to the counterface artificially to generate a high temperature close to the contact region. Of course the thermal/third body effects are not mutually exclusive – high contact temperatures could aid the formation of the third body film, although in this case this would still present the thermal effect as the governing variable, as a useful third body film



could not be formed without a sufficiently high temperature. Another method of evaluating the two effects exclusively would be to run a test until the steady-state coefficient of friction has been reached, then stop the test for a sufficient time to allow cooling back down to ambient temperature, then start the test again. In this case it could be assumed that the third body film had been formed, and was still present when the test was restarted. If the coefficient of friction on restarting was found to be higher, that would suggest that the temperature was not high enough to make the third body effective as a solid lubricant. If the coefficient of friction was unchanged, it would imply that the formation of the third body film was the governing factor in reducing the coefficient of friction.

As stated earlier, the impact of counterface roughness was not investigated with regard to modification of the wear rate or steady-state coefficient of friction of the samples. It was noted in Chapter 1 that some published work implies a critical roughness for minimum wear rate, and that if the initial roughness is above or below this critical value, the roughness will tend to this critical roughness over the course of the wear life of the material. This effect is seen in Chapter 5, where three different counterface roughnesses were tested. Papers in the literature suggest that this critical roughness is in the region of  $0.05\text{ }\mu\text{m Ra}$ , whereas the testing carried out in this project indicates a value of around  $0.22\text{ }\mu\text{m Ra}$ . Ra is not however an all-encompassing means of quantifying the functional significance of surface roughness however, as it does not account for form or the presence (or otherwise) of isolated, high asperity peaks, therefore detailed analysis of the surface using profilometry is needed to understand the important surface parameters affecting performance.

Humidity was highlighted in Chapter 1 as a key factor in the friction of composite bearing liners, however the test rig used in these experiments does not have the capacity to either record or control the local humidity. As the tests in this project were carried out over the course of three years, there will have been fluctuations in the local humidity, both daily and seasonal. It is proposed that, in future work, a method of recording local humidity be included on the test rig, as recording this fluctuation could, perhaps, be used to explain the spread of results in the same test for both friction and wear performance.

## **7.5 Future Work – Wear Model**

In order to make the wear model useful as a means of predicting the wear of a given bearing geometry, an appropriate  $K$  value (dimensionless constant of wear) must be found. This value should be obtained from experimental testing, and would hopefully be found to be uniform across a wide range of bearing geometries. This would mean that the wear model in its current form could be adopted as an aid for predicting wear of a given bearing geometry for at least the first 80% of its wear life.

The model should be further developed in order to predict the trend of wear over the last 20% of the bearing liner life. If the rapid increase in wear rate in this tertiary period is due to an increase in the proportion of reinforcement in the contact region, a  $K$  value could be used which varies dependent on the proportion of reinforcement calculated to be in the contact region from models of the material. Inclusion of this feature is possible through use of the tools already developed in this project.

In the current wear model, the stiffness of the liner is taken to be a fixed value. It should be possible to modify the model so that the stiffness changes with wear. In the case of the test liner, the softest materials are predominantly in the contact region of the unworn liner, meaning the liner becomes stiffer as it is worn.

By knowing the load and wear depth of points across the spherical plain bearing contact interface, it would be possible to make a prediction of the overall friction coefficient of the bearing and show the progression of this friction coefficient over the bearing's wear life. This would require information on the load/friction coefficient behaviour for different wear depths, which was not available given the time span of the project. Once this information is available and has been validated, integrating this into the wear model would be a useful additional feature.

A fully developed and experimentally verified bearing friction and wear model is an ambitious objective. In the case of customer applications it could be used as an advanced method of selecting the correct bearing geometry for the given application. As an aid in the development of new materials, it could be applied as a preliminary screening method for candidate materials, thus reducing the time spent in carrying out expensive testing.

## 7.6 Summary of Conclusions

- The friction and wear of self-lubricating bearing liners are affected by a range of factors governed by both the operating and environmental conditions.
- Composite 3D textile weaves can be modelled in an efficient manner when reasonable engineering approximations are made with regard to their structure.
- The friction model which has been developed is particularly sensitive to the coefficient of friction used for the resin material and care must therefore be exercised in determining this quantity.
- When an appropriate set of coefficients of friction are used for the constituent materials in the friction model, a good approximation is made of the friction behaviour over the bearing liner's life when compared to experimental results from coupon tests.
- Coupon tests of the coefficient of friction of the bearing liner suggest a dependence on contact pressure and oscillatory sliding distance.
- When the liner is subjected to a uniform contact pressure, its wear rate is found to be linear throughout its wear life.
- The wear model using the continuum mechanics approach gives a good approximation of the wear behaviour of full-scale bearing tests over the first 80% of their wear life and has potential for further development and improvement as a useful design aid.

## References

AST Bearings, 2013, “Steel-on-Bronze Series SPB” [online], [Accessed 12-01-2013], Available from: <http://www.astbearings.com/steel-on-bronze-spb.html>

Bell, A., 2009, “ARD511: Wear Hypothesis for SKF Airframe Self-lubricating bearing technology”, SKF Ltd.

Bell, A., 2012a, *Private Communication*.

Bell, A., 2012b, *Private Communication*.

Bell, A., 2013, *Private Communication*.

Bennett, A., 2008, “ARD498: Liner Compressive Stiffness Analysis”, SKF Ltd.

Bernard, P., 2011, “Discrete Modelling of Woven Structures”, SKF Ltd.

Bortoleto, E.M., Rovani, A.C., Seriacopi, V., Profito, F.J., Zachariadis, D.C., Machado, I.F., Sinatora, A., Souza, R.M., 2013, “Experimental and numerical analysis of dry contact in the pin on disc test”, *Wear*, v.301, pp. 19-26.

Bowman, D., Balch, J., Artaxo, P., 2009, “Fire in the Earth system”, *Science*. v. 324, pp. 481–4.

Bramham, R.W., King, R.B., Lancaster, J.K., 1980, “Fluid Contamination Effects on the Wear of PTFE-Containing Dry Bearings”, *ASLE Prep 80LC6B3*.

---

Briscoe, B.J., Evans, P.D., Lancaster, J.K., 1988, “The influence of debris inclusion on abrasive wear relationships of PTFE”, *Wear*, v. 124, pp. 177-194.

Brossard, I., 1997, “Technologie des Textiles” (in French), *Dunod*, Paris.

Callister, W.D., 2007, “Materials Science and Engineering – An Introduction” *John Wiley & Sons*.

Cao, L., Shen, X., Li, R., 2010, “Three-dimensional Thermal Analysis of Spherical Plain Bearings with Self-lubricating Fabric Liner”, *Advanced Materials Research*, v. 97, pp. 3366-3370.

Carnes, K., 2005, “The Ten Greatest Events in Tribology History”, *STLE*.

Cook, J.G., 1968, “Handbook of Textile Fibres 2 – Man-made fibres” *Merrow Publishing*, Watford.

Dayot, C., 2011, “Wear Scenario of a Bearing Liner”, *SKF Ltd*.

Department of Education and Science, 1966, “Lubrication (Tribology) Education and Research. A Report on the Present Position and Industries’ Needs”, *HMSO*, London.

Dowson, D., 1979, “History of Tribology”, *Longman Ltd*.

DSS Abaqus, 2012, “Analysis User’s Manual”.

Engineering Toolbox, 2013, “The Engineering Toolbox”, [online], [Accessed 12-01-2013], Available from: [http:// http://www.engineeringtoolbox.com/](http://www.engineeringtoolbox.com/)

---

Eto, E., 2008, "Barnsdall Weaving Class" [online], [Accessed 12-01-2013], Available from: [http://www.supercozy.com/blog/2008\\_08\\_01\\_supercozy\\_archive.html](http://www.supercozy.com/blog/2008_08_01_supercozy_archive.html)

Evans, D.C., 1978, "The friction and wear properties of PTFE composites at elevated temperatures", RAE Tech. Report 77070, *Royal Aircraft Establishment*, Farnborough.

Evans, D.C., 1978, "Polymer-fluid interactions in relation to wear", *Proc. 3rd Leeds-Lon Symp. on Wear of Non-metallic Materials*.

Fillot, N, Iordanoff, I, Berthier, Y, 2005, "Simulation of Wear through Mass Balance in a Dry Contact", *ASME Journal of Tribology*, v. 127, pp. 230-237.

Floquet, A., Play, D., Godet, M., 1977, "Surface Temperatures in Distributed Contacts, Application to Bearing Design", *ASME Journal of Lubrication Technology*, v. 99, pp. 277-283.

Floquet, A, Play, D, 1981, "Contact Temperature in Dry Bearings. Three Dimensional Theory and Verification", *ASME Journal of Lubrication Technology*, v. 103, pp. 243-251.

Godet, M., Play, D., 1975, "Third-body formation and elimination on carbon-fibre/epoxy composite", *Space tribology proceedings of the first European Space Tribology, Fracasti, Italy*, p.165-173.

Godet, M., Play, D., Berthe, D., 1980, "An attempt to provide a unified treatment of tribology through load carrying capacity, transport, and continuum mechanics", *Journal of Lubrication Technology*, v. 102, pp. 153-164.

Holmberg, K., Matthews, A., Ronkaninen, H., 1997, "The Tribological Mechanisms of Coated Surfaces", *ASME Journal of Tribology*, v.2, pp. 615-622.

---

Johnson, K.L., 1987, “Contact Mechanics”, *Cambridge University Press*.

Kennedy, F.E., Smidhammar, L., Play, D., 1975, “Wear of polyethylene in small-amplitude oscillatory motion”, *Proc. 4th Eur. Trib. Congress*, v. 2, pp. 1-9.

King, R. B., 1979, “Wear Properties of Dry Bearing Liners at Ambient and Elevated Temperatures”, *Wear*, v. 56, pp. 37-53.

Lancaster, J. K., 1972, “Lubrication of carbon fibre-reinforced polymers. Part 1 Water and aqueous solutions”, *Wear*, v. 2, pp. 315-333.

Lancaster, J. K., 1979, “Accelerated Wear Testing of PTFE Composite Bearing Materials”, *Tribology International*, v. 12, pp.65-75.

Lancaster J.K., 1981, “On the initial stages of wear of dry-bearing composites”, *Ministry of Defence*.

Lancaster, J.K., 1982, “Accelerated wear testing as an aid to failure diagnosis and materials selection”, *Tribology International*, v. 15, pp. 323-329.

Lancaster, J.K., Bramham, R. W., Play, D., Waghorne, R., 1982, “Effect of Amplitude of Oscillation on the Wear of Dry Bearings containing PTFE”, *ASME Journal of Lubrication Technology*, v. 104, pp. 559-568.

Li, J., Ran, Y., 2010 “Evaluation of the friction and wear properties of PTFE composites filled with glass and carbon fiber”, *Materialwissenschaft und Werkstofftechnik*, v. 41, pp. 115-118.



---

Li, K., Shen, X. J., Chen, Y., Li, R., 2008, “Numerical Analysis of Woven Fabric Composites Lubricated Spherical Plain Bearings”, *Proc. 11th Intl Congress, Soc. For Experimental Mechanics Inc.*

Liu, Z., Shen, X., 2010, “Study on the Elastic Properties of the Woven Fabric Liner of Spherical Plain Bearing with Self-lubricating”, *Advanced Materials Research*, v. 139, pp. 190-193.

Moreno, R., 2012, “What does shape function mean in finite element modelling?” [online], [Accessed 12-01-2013], Available from:  
<http://stochasticandlagrangian.blogspot.co.uk/2011/07/what-does-shape-function-mean-in-finite.html>

Moreton, R., 1983, “The wear behaviour of PTFE-based composite materials at different relative humidities”, *RAE Technical Memo*.

Morgan, J.E., Plumbridge, W.J., 1987, “The effect of humidity on dry bearing torque”, *Wear*, v. 119, pp. 215-223.

Parsons, E., Weerasooriya, T., Sarva, S., Socrate, S., 2010, “Impact of Woven Fabric: Experiments and Mesostructure-Based Continuum-Level Simulations”, *Journal of Mechanics and Physics of Solids*, v. 58, pp. 1995-2021.

Pihtili, H., Tosun, N., 2002, “Effect of load and speed on the wear behaviour of woven glass fabrics and aramid fibre-reinforced composites”, *Wear*, v. 252, pp. 979-984.

Pihtili, H., 2009, “An experimental investigation of wear of glass fibre-epoxy resin and glass fibre-polyester resin composite materials”, *European Polymer Journal*, v. 45, pp. 149-154

Play, D., Godet, M., 1977, “Self-Protection of High Wear Materials”, *ASLE Transactions*, v. 22, pp. 56-64.

---

Play, D., Pruvost, B., 1984, “Comparative dry Wear of PTFE Liner Bearing in Cylindrical and Spherical Geometry”, *ASME Journal of Tribology*, v. 106, pp. 185-193.

Play, D., 1985, “Mutual Overlap Coefficient and Wear debris motion in dry oscillating friction and wear tests”, *ASLE Transactions*, v. 28, pp. 527-535.

Puso, M., 2006, “A stabilized nodally integrated tetrahedral”, *International Journal of Numerical Methods in Engineering*, v. 67, pp. 841-867.

Python, 2013, “Python Programming Language – Official Website”, [online], [Accessed 12-01-2013], Available from: <http://www.python.org/>

Richard, D, Iordanoff, I, Berthier, Y, Renouf, M, Fillot, N, 2007, “Friction Coefficient as a Macroscopic View of Local Dissipation”, *ASME Journal of Tribology*, v. 129, pp. 829-835.

Richard, D, Iordanoff, I, Renouf, M, Berthier, Y, 2008, “Thermal Study of the Dry Sliding Contact with Third Body Presence”, *ASME Journal of Tribology*, v. 130, pp. 031404.1-031404.10.

Rossi, C., Russo, Fe., Russo, Fl., 2009, "Ancient Engineers' Inventions: Precursors of the Present", *Springer*, pp. 171.

SAE, 1998, “AS81820 - Bearings, Plain, Self-Aligning, Self-Lubricating, Low Speed Oscillation”, *SAE International*.

SAE, 2007, ”Aerospace Recommended Practice”, *SAE International*.

Santner, E., Czichos, H., 1989, "Tribology of Polymers", *Tribology International*, v. 22, pp. 103-109.

---

Siede, G, 2012, “Research at ITA: Polymers”, [online],  
[Accessed 12-01-2013], Available from:  
[http://www.ita.rwth-aachen.de/andere\\_sprachen/englisch/3-06-polymers.html](http://www.ita.rwth-aachen.de/andere_sprachen/englisch/3-06-polymers.html)

SKF Group, 2010, “SKF Spherical Plain Bearings and Rod Ends”.

Sliney, H. E., Williams F. J., 1982, “Performance of PTFE-Lined Composite Journal Bearings”, *Ann. Meeting of the Am. Soc. of Lubrication Engr.,; 10-13 May 1982; Cincinnati, OH; United States*.

Stojek, Z., Osteryoung, J., 1989, “Experimental Determination of the Coefficient in the Steady State Current Equation for Spherical Segment Microelectrodes”, *Office of Naval Research*.

Texgen, 2013, “Main Page”, [online], [Accessed 12-01-2013], Available from:  
[http://texgen.sourceforge.net/index.php/Main\\_Page](http://texgen.sourceforge.net/index.php/Main_Page)

U.S. Customs and Border Protection (U.S.C.P.B.), 2012, “What Every Member of the Trade Community Should Know About: The Classification of Ball Bearings, Roller Bearings and Parts Thereof”, *Informed Compliance*.

US Navy, 1998, “MIL-B-81820F - Bearings, Plain, Self-Aligning, Self-Lubricating, Low Speed Oscillation”.

US Navy, 2000, “MIL-B-81819B - Bearings, Plain, Self-Lubricating, Self-Aligning, High Speed Oscillation”.

Verma, A.P., Vishwanath, B., Kameswara Rao, C.V.S., 1996, “Effect of resin modification on friction and wear of phenolic composites”, *Wear*, v. 193, pp. 193-198.

---

Wagner, J., 2010, “New Formaldehyde Regulations Are Headed Your Way” [online], [Accessed 12-01-2013], Available from:  
<http://www.propelmg.com/blog/2010/08/new-formaldehyde-regulations-are-headed-your-way/>

Yang, Y., Ma, C., Huang, S., Jing, L., Pang, H., 2010, “Effects of Mechanical Properties of Kevlar/PTFE Fabric-Reinforced Self-lubricating Liners on Performance of Self-lubricating Spherical Plain Bearings”, *Applied Mechanics and Materials*, v. 29, pp. 197-202.

Yang, Y., Zu, D., Zhang, R., QI, X., 2009, “Effects of Friction Heat on the Tribological Properties of the Woven Self-lubricating Liner”, *Chinese Journal of Mechanical Engineering*, v. 22, pp. 918-927.